DFVLR Deutsche Forschungs- und Versuchsanstalt für Luft- und Raumfahrt

Forschungsbericht

Excited Waves in Shear Layers

Dietrich W. Bechert

DFVLR
Institut für Experimentelle Strömungsmechanik
Göttingen
Abteilung Turbulenzforschung, Berlin

DFVLR-FB 82-23

DFVLR Deutsche Forschungs- und
Versuchsanstalt
für Luft- und Raumfahrt

Forschungsbericht

Excited Waves in Shear Layers

Dietrich W. Bechert

DFVLR
Institut für Experimentelle Strömungsmechanik
Göttingen
Abteilung Turbulenzforschung, Berlin

150 Seiten
26 Bilder
3 Tabellen
42 Literaturstellen

DFVLR-FB 82-23

DM 31,40

Manuskript eingereicht am 27. August 1982

Excited Waves in Shear Layers *)

Deutsche Forschungs- und Versuchsanstalt für Luft- und Raumfahrt
Forschungsbereich Strömungsmechanik
Institut für Experimentelle Strömungsmechanik
Abteilung Turbulenzforschung
Müller-Breslau-Str. 8, D-1000 Berlin (West) 12, West-Germany

Berlin, im April 1982

Komm. Forschungsbereichsleiter:

Prof. Dr.rer.nat. H. L. Jordan

Institutsleiter:

H. Hornung, Ph. D.

Verfasser:

Dr.-Ing. D. W. Bechert

Abteilungsleiter:

Dr.-Ing. E. Pfizenmaier

---

*) Supported by NASA Lewis Research Center Grant NAG 3-198 (1981)
and by the Deutsche Forschungsgemeinschaft Grant Be 889/1-1 (1982)

Stability Theory, Aeroacoustics, Shear Layers

Excited Waves in Shear Layers

Summary

The generation of instability waves in free shear layers is investigated. The model assumes an infinitesimally thin shear layer shed from a semi-infinite plate which is exposed to sound excitation. For this model, it is shown that only forced instability waves and a Kutta condition at the trailing edge are possible. The shear layer excitation by a source further away from the plate edge in the downstream direction is very weak while upstream from the plate edge the excitation is relatively efficient. A special solution is given for the source at the plate edge. Any type of source further away from the plate edge creates a parabolic pressure field near the edge. For this latter, fairly general case, a reference quantity is found for the magnitude of the excited instability waves. The theory is then extended to two streams on both sides of the shear layer having different velocities and densities. Furthermore, the excitation of a shear layer in a channel is calculated. The limitations to the theory and some aspects related to experiments are discussed. In particular, for a comparison with measurements, numerical computations of the velocity field outside the shear layer have been carried out.

Stabilitätstheorie, Aeroakustik, Scherschichten

Angeregte Wellen in Scherschichten

Übersicht

Die Erzeugung von Instabilitätswellen in freien Scherschichten wird untersucht. Dabei wird eine unendlich dünne Scherschicht betrachtet, die am Ende einer halbunendlichen Platte entsteht. Diese Scherschicht wird akustisch angeregt. Für dieses Modell wird gezeigt, daß nur erzwungene Instabilitätswellen möglich sind und daß an der Plattenendkante die Kuttasche Abflußbedingung gilt. Die Anregung der Scherschicht durch eine Quelle stromab der Plattenkante ist schwach, während die Anregung von stromauf relativ wirksam ist. Für die Anregung direkt an der Plattenkante wird eine spezielle Lösung angegeben. Jede Art von Quellen in größerer Entfernung von der Plattenkante erzeugt ein parabolisches Druckfeld in Kantennähe. Zu diesem letzteren, recht allgemeinen Fall wird eine Referenzgröße für die Amplitude der Instabilitätswellen angegeben. Die Theorie wird ausgeweitet auf zwei Strömungen auf beiden Seiten der Scherschicht mit verschiedenen Geschwindigkeiten und Dichten. Außerdem wird die Anregung einer Scherschicht in einem Kanal berechnet. Die Grenzen der Theorie sowie einige experimentelle Aspekte werden diskutiert. Zum Vergleich mit Messungen wird das Geschwindigkeitsfeld außerhalb der Scherschicht numerisch berechnet.

Contents page

1. Introduction..... 7
2. One stream model..... 11
2.1. Differential equation for v..... 15
2.2. Differential equation for u..... 30
3. Field calculations..... 37
4. The relative importance of the edge region..... 46
5. Two streams with different densities..... 55
6. Theoretical considerations related to experiments..... 61
6.1. "Overshoot" of the mean velocity profile..... 62
6.2. Entrainment and finite shear layer thickness effects..... 65
6.3. Channel effects..... 67
6.3.1. Effects on the excitation field..... 69
6.3.2. Effects on the resulting shear layer motion..... 76
6.3.3. The induced u-velocities..... 80
7. Speculations..... 81
8. Conclusions and survey of essential results..... 83
9. References..... 92
10. Appendices..... 99
10.1. Appendix A: Glossary of symbols..... 99
10.2. Appendix B: Discussion of the pressure sources..... 110
10.3. Appendix C: The absence of "free" instability waves..... 116
10.4. Appendix D: v-computations at $y = \pm o$, tables..... 121
10.5. Appendix E: u-computations at $y < o$, tables..... 138

1. Introduction

Let us first consider a picture of the interaction process which we are going to investigate. In Fig. 1 a photograph of the evolution of a plane free shear layer can be seen. The shear layer is forced by acoustic excitation into wave motion and vortex roll-up. The lower half of the picture shows a flow from left to right whereas the upper half shows a very slow entrainment flow in the same direction. A smoke filament is injected into the shear layer from the low-speed side. A splitter plate separating the two streams ends at the left hand side of the picture. Around the end of this splitter plate a fluctuating pressure field is created by vibrating plates outside the flow.

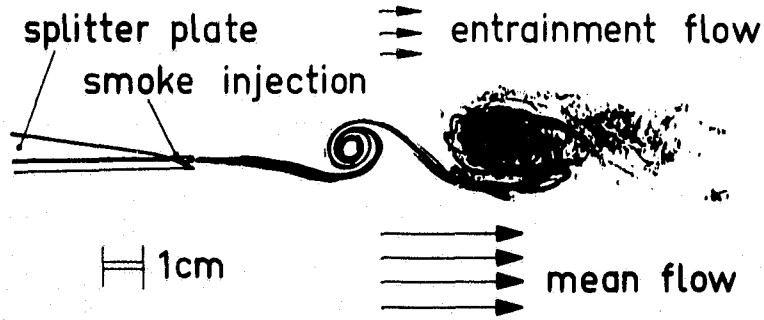

Fig. 1 Free shear layer evolution with acoustic forcing. For more convenient reproduction, the colours have been inverted so that the white sulfuric acid smoke filament is shown in black. Mean flow velocity 6.4 m/s, entrainment velocity ≈ 0.6 m/s, frequency 63 Hz, forcing reference velocity $\Delta p_{12}/\rho\sqrt{\omega\theta_1} = 0.354$ m/s RMS (definition see section 2.1.), Strouhal number $S_\theta = 0.0040$.

Although impressive, pictures like Fig. 1 have been observed many times in the past. In particular, the observation of the sensitivity of flames to sound has been made by Leconte [1] as early as 1858. Tyndall [2] has shown in 1867, that also jets without

combustion are sensitive to sound. Experimental observations like these were already known to Lord Kelvin, von Helmholtz and Lord Rayleigh when they laid the foundations to the stability theory of flows. Lord Rayleigh,e.g., refers to sound-sensitive smoke jets in his 1880 paper "On the stability, or instability, of certain fluid motions" [3]. Since that time, stability theory has used a model assuming a parallel flow extended from $x = -\infty$ to $x = +\infty$ which is disturbed by a wave motion with constant magnitude in streamwise direction and growing with time. This approach is perfectly valid to answer the question whether or not a flow is unstable. However, it is not appropriate to use this model if an instability wave is driven by an oscillatory excitation which does not vary with time. In 1962, it has been suggested by Gaster [4] and Watson [5], that in this latter case a stability analysis with spatially growing waves is the only reasonable approach. For free shear layers, the spatial stability model has been verified by Michalke [6] and Freymuth [7]. In addition, it has become evident from Freymuth's experiments, that the magnitude of the spatial instability waves is linearly dependent on the exterior forcing by, e.g., an acoustic field.

In spite of the numerous experiments with artificially forced shear layers and jets which have been carried out in the meantime, the mechanism describing how the perturbations were introduced into the flow was not yet understood.*) About a decade ago, however, a few theoretical papers appeared which included a semi-infinite plate into the stability analysis of a thin free shear layer. The introduction of such a solid surface into the

*) Also some theoretical papers on this issue have inherent problems, e.g., Tam's paper [8] discusses the excitation of a shear layer by an acoustic beam. His model assumes a beam width of typically 20 ÷ 60 times the momentum thickness of the shear layer. On the other hand, the range of unstable waves in the shear layer requires a relatively low excitation frequency. This would cause the beam width to be about 1/100 of the acoustic wavelength. Unfortunately, it is not possible to form an acoustic beam narrower than several acoustical wavelengths.

analysis turned out to be of crucial importance in the understanding of the coupling between sound waves and instability waves. The first of these papers [9], albeit mathematically correct, led to some confusion of the physics. Later, a few other theoretical papers were published [10, 11] which utilized (as [9]) a Fourier transform procedure (i.e., the Wiener-Hopf technique), whereas a simpler approach using symmetry/asymmetry arguments [12, 13] turned out to be more elegant but also less versatile in its applicability. In the present investigation we will extend and exploit this latter approach [12] so that theoretical data are available which can be compared to experiments. Any testing of the new theories [10 ÷ 13] had not been carried out previously because the previous theories were presented in a way which could not be verified easily by experimentalists. Indeed, we think that it is desirable in this field to track down by individual experiments all basic assumptions and findings of the first simple theories before going on to more complex problems. The rewarding aspect of this "old fashioned" type of research is, that simple analytic solutions are obtained which can be checked with (moderately) simple experiments.

There are different motivations for the present investigation:

(i) From the viewpoint of scientific curiosity it is interesting how perturbations are introduced into a shear flow. These perturbations cause instability waves which, in turn, lead to turbulence. This development can be seen in Fig. 1. The interaction region is found close to the lip of the splitter plate. The emerging instability waves are amplified rapidly in the downstream direction. As usual in flow vizualisation pictures, the linear growth regime cannot be seen clearly, because the displacements of the shear layer are still too small to be visible. Since the amplification rate of the instability waves is rather high (about 500 times within the first 10 cm of Fig. 1), the onset of nonlinearities characterized by the vortex roll-up occurs rather suddenly (see also [6, 7]).

(ii) A behaviour very similar to instability wave evolution (orderly structures) has been found also in turbulent jets [14, 15] exposed to acoustic excitation. On the other hand, similar orderly structures have been found also in "unexcited jets" [16]. Recently, however, it has been shown, that at least in turbulent shear layers, orderly structures become highly organized and dominant if an involuntarily generated, mostly unnoticed and sometimes inaudible acoustic excitation does exist [17, 18].

(iii) The investigations on acoustically excited turbulent jets have led to findings of practical importance. It has been found, that broad band jet noise can be amplified by a pure tone acoustic excitation from inside the nozzle [19 + 21]. Because of its relevance to aircraft noise generation this observation has triggered a number of further investigations [22 + 24]. It has been recognized, that the acoustic excitation of stability waves plays a crucial rôle in this mechanism [19, 21, 24].

(iv) The change in acoustic radiation of turbulent jets due to acoustical excitation is accompanied by quite substantial changes in the flow pattern. An amplification of the jet noise corresponds to an enhanced mixing and an increased pertubation level in the near field of the jet [21, 25]. On the other hand, it has been shown, that the spreading rate of a jet can also be reduced by acoustic control of the shear layer [25, 26].

(v) Whereas the above-mentioned broad band jet noise amplification is basically a <u>nonlinear</u> effect, another related interaction has been found. It has been shown, that the generation of instability waves at an edge can extract energy from a sound field [27 + 30]. This absorption effect is (at least for small perturbations of a mean flow) a <u>linear</u> effect. It can lead to quite dramatic sound absorptions, in particular at low frequencies. To give an example: Consider the sound transmission through a nozzle and a jet at, say, a jet Mach number of $M = 0.3$ and a

dimensionles frequency $\frac{\omega R}{a_o} = 0.1$. For these parameters*) only 1 % of the sound power transmitted through the nozzle exit will be transmitted into the far field!

This paper, however, will not provide any detailed prediction on any of the three latter effects. Nevertheless, the basic underlying interaction mechanism between sound waves and free shear layers will be dealt with and we will be able to predict, e.g., the perturbation magnitude introduced into the shear layer shown in Fig. 1. In addition, a well-defined reference quantity representing the acoustic excitation will be given so that future experimental investigators will be able to replace arbitrarily taken reference pressures, velocities, or even loudspeaker input voltages by a more general and appropriate reference quantity.

This paper will only deal with theoretical aspects of the shear layer excitation. There is evidence from our recent experiments that the present theory is valid in the expected range.

2. One stream model

Fig. 2 shows the simplified configuration which will be modelled mathematically. The geometry is basically the same as in Fig. 1. We will, however, assume that there is no flow above the shear layer (this condition will be released in section 5). The acoustic field is assumed to be created by a pulsating source outside the shear layer in the fluid at rest.

The following simplifying assumptions are introduced:

1. plane flow
2. parallel mean flow
3. linearized problem
4. all fluctuating quantities harmonic in time, i.e., $\propto e^{-i\omega t}$
5. inviscid flow
6. incompressible flow
7. infinitesimally thin shear layer

*) R is the radius of the nozzle, ω is 2π times the frequency and a_o is the sound speed.

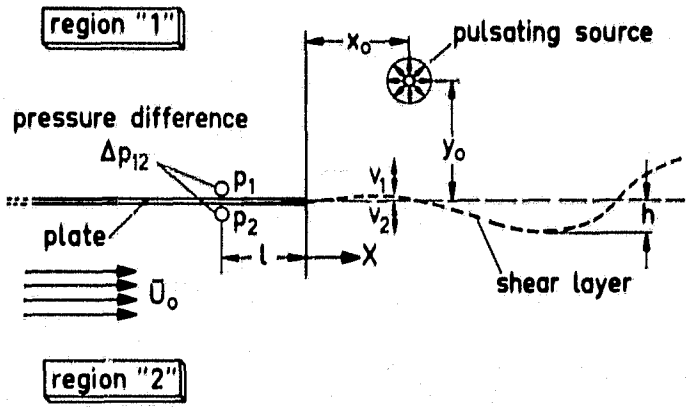

Fig. 2 Configuration of the analytic model.

The first five simplifications are common in the stability theory of free jets. The assumption of an inviscid flow works quite well at sufficiently high Reynolds number [6, 7]. The sixth assumption is equivalent to the restriction to small Mach numbers and small Helmholtz numbers, where the Helmholtz number is defined as the ratio of the typical length of the problem to the wavelength of the sound waves. For our problem, the latter condition means, that the interaction region close to the lip should be small compared to the acoustic wavelength. It will turn out, that this region has a dimension of the order $\bar{U}_o/f$ (where $\bar{U}_o$ is the mean flow velocity and f the sound frequency). Consequently, we should have $\bar{U}_o/f \ll a_o/f$, where a_o/f is the acoustic wavelength. This is

equivalent to $M = \bar{U}_o/a_o \ll 1$, i.e., again the condition of small Mach number. The seventh assumption, the restriction to an infinitesimally thin shear layer will limit the validity range of the theory to the case where the shear layer thickness is small compared to the wavelength of the instability waves. In other words, the Strouhal number $f\theta/\bar{U}_o$ should be small. θ is the momentum thickness of the shear layer.

After all these simplifications we end up with the linearized Euler equation and the continuity equation in the following form:

$$(1) \qquad -i\omega u + \bar{U}\frac{\partial u}{\partial x} + v\frac{\partial \bar{U}}{\partial y} + \frac{1}{\rho}\frac{\partial p}{\partial x} = o$$

$$(2) \qquad -i\omega v + \bar{U}\frac{\partial v}{\partial x} + \frac{1}{\rho}\frac{\partial p}{\partial y} = o$$

$$(3) \qquad \frac{\partial u}{\partial x} + \frac{\partial v}{\partial y} = o$$

where $\bar{U}$ is the mean flow velocity and u, v, p are fluctuating quantities, all proportional to $e^{-i\omega t}$.

The classical approach would be to fulfill the boundary conditions at both sides of the shear layer, which means that both the pressure p and the displacement h should be equal there. We focus first on the pressure condition. Instead of taking p we may as well choose $\partial p/\partial x$. Above the shear layer (index "1") we have $\bar{U} = o$. Equation (1) then reads

$$(4) \qquad -i\omega u_1 + \frac{1}{\rho}\frac{\partial p_1}{\partial x} = o,$$

Below the shear layer (index "2") we have $\bar{U} = \bar{U}_o$ and

$$(5) \qquad -i\omega u_2 + \bar{U}_o\frac{\partial u_2}{\partial x} + \frac{1}{\rho}\frac{\partial p_2}{\partial x} = o,$$

If we subtract eq. (5) from eq. (4) we obtain

$$(6) \qquad u_2 + i\,\frac{\bar{U}_o}{\omega}\,\frac{\partial u_2}{\partial x} - u_1 = \frac{i}{\rho\omega}\,\frac{\partial (p_1-p_2)}{\partial x}\,.$$

For $x > o$ we should have $p_1-p_2 = \Delta p_{12} = o$.

This is a first equation connecting the u-velocities at both sides of the shear layer.

Now we consider the condition of equal displacements. The displacement h and the velocity v are connected in the following way

$$(7) \qquad v = \frac{\partial h}{\partial t} + \bar{U}\,\frac{\partial h}{\partial x}\,.$$

In the region above the shear layer we have with $\bar{U} = o$

$$(8) \qquad v_1 = -i\omega h;$$

and below the shear layer we obtain

$$(9) \qquad v_2 = -i\omega h + \bar{U}_o\,\frac{\partial h}{\partial x}\,.$$

We can insert h from eq. (8) and find

$$(10) \qquad v_2 = v_1 + i\,\frac{\bar{U}_o}{\omega}\,\frac{\partial v_1}{\partial x}\,,$$

which is the second connecting equation between the velocities at both sides of the shear layer at $y = \pm o$. However, equations (6) and (10) are valid for two different velocity components. If we want to find solutions for v <u>and</u> u we have to generate (i) two equations for the two unknowns v_1 and v_2 as well as (ii) again two equations for the two unknowns u_1 and u_2.

(i) A second equation for v_1 and v_2 can be produced in two different ways. In [12] it is shown how eq. (6) can be converted into an equation for v using a source distribution approach. We will follow, however, another procedure (which

is also given in [12]) which will provide more insight into the physics; this latter approach we will call the pressure gradient approach.

(ii) To create a second equation for u_1 and u_2 we have to convert eq. (10) from an equation for v into an equation for u. This will be done using a vorticity distribution approach.

2.1. Differential equation for v

The aim of this section is to create a second equation for v_1 and v_2 out of a consideration of the pressure field and its gradients at the shear layer. Then we will derive a differential equation for v_1 only and solve it.

We start out by taking the x-derivative of the first Euler equation (1). Subsequently, we take the y-derivative of the second Euler equation (2). Both derivatives are added and some terms are eliminated using the continuity equation (3). We end up with

$$(11) \qquad \nabla^2 p = -2\rho \frac{\partial v}{\partial x} \cdot \frac{\partial \bar{U}}{\partial y} .$$

In our model, the mean velocity profile jumps from $\bar{U} = o$ for positive y to $\bar{U} = \bar{U}_o$ for negative y. This can be represented in terms of a Heaviside step function H

$$(12) \qquad \bar{U} = \bar{U}_o \cdot H_{(-y)} .$$

The derivative of a step function is a delta function and we obtain from eq. (11) and (12)

$$(13) \qquad \nabla^2 p = 2\rho \bar{U}_o \cdot \frac{\partial v}{\partial x} \cdot \delta_{(y)} .$$

Eq. (13) is a nonhomogeneous Laplacean equation with a line source of varying strength in the shear layer. It should be stressed here, that the sources in the shear layer are pressure sources and not sources of fluid; the latter would violate the continuity equation (3). Since there might be some confusion

about the structure of these pressure sources we will give, as an example, the detailed pressure source structure of an amplified instability wave in appendix B. It will be shown there that eq. (13) can be integrated to produce the whole pressure field. For the further progress of our calculation, however, a detailed knowledge of the pressure sources is <u>not</u> necessary.

At the surface of the semi-infinite plate we have v and $\partial v/\partial x$ equal to zero. Consequently, the pressure source strength is zero on the plate surface (see eq. (13)). The only other location where $\nabla^2 p$ is nonzero is at the location of the exterior pulsating source (see Fig. 2). The basic idea of this approach is, that the pressure distribution in the whole field can be split into two contributions:

(i) a pressure field which is <u>symmetric</u> with respect to the shear layer and which is created by the pressure source distribution in the shear layer itself.

(ii) a pressure field which is created by the exterior forcing, e.g., a pulsating source. The pressure fluctuations of this contribution are transmitted through the shear layer. The pressure gradient of this contribution is continuous through the shear layer and therefore it is <u>antisymmetric</u> close to the shear layer.

As a result of this splitting process we have

$$(14)\begin{cases} p_1 = p_{1s} + p_{1f};\ p_2 = p_{2s} + p_{2f} \\ v_1 = v_{1s} + v_{1f};\ v_2 = v_{2s} + v_{2f} \\ u_1 = u_{1s} + u_{1f};\ u_2 = u_{2s} + u_{2f} \end{cases}$$

The index s stands for <u>s</u>hear layer and the index f labels the exterior <u>f</u>orcing. The boundary conditions at both sides of the shear layer have to be fulfilled by the summations of the individual constituents, e.g., by v_1 and v_2; as before. On the other hand, we have some new informations: Since the induced

field of the pressure sources in the shear layer is symmetrical (it is created by sources of symmetrical directivity in a field with symmetrical boundary conditions) we obtain:

$$(15) \qquad \frac{\partial p_{1s}}{\partial y} = - \frac{\partial p_{2s}}{\partial y} \quad \text{at} \quad y = \pm o$$

and for the continuous pressure of the exteriour forcing

$$(16) \qquad \frac{\partial p_{1f}}{\partial y} = \frac{\partial p_{2f}}{\partial y} \quad \text{at } y = \pm o \ .$$

These conditions for the pressure gradients in y-direction can be inserted into the 2nd Euler equation (2), which gives

$$(17) \qquad v_{2s} + i \frac{\bar{U}_o}{\omega} \frac{\partial v_{2s}}{\partial x} = -v_{1s}$$

$$(18) \qquad v_{2f} + i \frac{\bar{U}_o}{\omega} \frac{\partial v_{2f}}{\partial x} = v_{1f} \ .$$

Equations (17) and (18) can be added, using eq. (14)

$$(19) \qquad v_2 + i \frac{\bar{U}_o}{\omega} \frac{\partial v_2}{\partial x} + v_1 = 2v_{1f} \ .$$

This is the desired second equation for v_1 and v_2. The velocity v_{1f} is not an unknown quantity, it is the velocity which is created by the exterior forcing <u>without</u> the mean flow being present, but in the presence of the semi-infinite plate. Equation (10) can be inserted into eq. (19) to obtain a non-homogenous differential equation

$$(20) \qquad 2v_1 + 2i \frac{\bar{U}_o}{\omega} \frac{dv_1}{dx} - \left(\frac{\bar{U}_o}{\omega}\right)^2 \frac{d^2 v_1}{dx^2} = 2v_{1f} \ .$$

The homogeneous solutions of this equation are found easily

$$(21) \qquad \varphi_1 = c_1 e^{\lambda_1 x}, \ \varphi_2 = c_2 e^{\lambda_2 x}$$

with

$$(22) \qquad \lambda_1 = \frac{\omega}{\bar{U}_o}(i+1);\ \lambda_2 = \frac{\omega}{\bar{U}_o}(i-1),$$

C_1 and C_2 are arbitrary constants with the dimension of a velocity. φ_1 and φ_2 are the well-known spatial stability waves for an infinitesimally thin shear layer, extended from $-\infty$ to $+\infty$, which we will call the Helmholtz solutions. The complete solution can be obtained in a straightforward way

$$(23) \qquad \boxed{v_1 = -\frac{\omega}{\bar{U}_o} e^{\lambda_1 x} \int_{G_1}^{x} e^{-\lambda_1 x} v_{1f}\,dx + \frac{\omega}{\bar{U}_o} e^{\lambda_2 x} \int_{G_2}^{x} e^{-\lambda_2 x} v_{1f}\,dx}$$

This is the general solution for v_1. Once v_1 has been found, v_2 can be determined with eq. (10). The lower boundaries G_1 and G_2 will produce terms of the Helmholtz solution type. The actual value of G_1 and G_2 depends on the boundary conditions; this will be discussed in detail for our configuration (shown in Fig. 2). However, before we are going to do this, we have to consider the structure of v_{1f}, the fluctuating vertical velocity at $x > o$ and $y = o$ which is created by the exterior excitation.

The general solution (23) for v, was obtained by splitting the pressure field into two constituents p_f, the forcing field and p_s the field induced by the shear layer wave motion. The field p_f is continuous through the shear layer. It can be seen, e.g., from equation (2), that the velocities cannot be continuous through the shear layer, in other words: $v_{1f} \neq v_{2f}$. Therefore, the appropriate approach is to calculate the pressure field first, which follows from $\nabla^2 p = o$ outside the source location and the shear layer. After splitting it into the two constituents we have (i) the excitation pressure field p_f with a singularity at the location of the exciting source (x_o, y_o) (see Fig. 2) and (ii) the shear layer pressure field p_s with a pressure source distribution in the shear layer ($x > o$, $y = o$). As we know from potential theory, analytic functions of $z = x \pm iy$ are solutions

of the Laplacean equation for the pressure. Therefore, we can use all known tools of conformal mapping to calculate, e.g., the pressure field p_f. In the fluid at rest ($\bar{U} = 0$ in region "1" of Fig. 2) there is a simple relation between the velocities and the pressure. This can be obtained from the two Euler equations (1) and (2).

$$(24) \qquad u_1 = -\frac{1}{\rho\omega}\frac{\partial p}{\partial x} \; ; \quad v_1 = -\frac{1}{\rho\omega}\frac{\partial p}{\partial y} \, .$$

We recognize, that, in a fluid at rest, the pressure is proportional to the potential function ϕ which is defined as

$$(25) \qquad u = \frac{\partial \phi}{\partial x} \; ; \quad v = \frac{\partial \phi}{\partial y} \, .$$

This allows us to use conventional potential theory to calculate, say, v_{1f} for a source or a dipole in conjunction with a semi-infinite plate. This has been done in [12] and we will give only the results here. For a pulsating two-dimensional source, as shown in Fig. 2 we have

$$(26) \qquad v_{\substack{1f \\ (y=0)}} = -\frac{1}{i\omega} \cdot \frac{Q}{4\pi} \cdot \frac{(x + r_o)\sqrt{2(r_o - x_o)}}{(x - x_o)^2 + y_o^2}$$

with

$$(27) \qquad r_o = \sqrt{x_o^2 + y_o^2} \, .$$

x_o and y_o are the horizontal and vertical distances, respectively, of the source from the plate edge and Q is the source strength, say, in m^2/s. Clearly, Q is fluctuating as

$$(28) \qquad Q = Q_o e^{-i\omega t} \, .$$

For large distances $r_o \gg x$ we have simply

$$(29) \qquad v_{1f} = -\frac{1}{i\omega} \cdot \frac{Q}{4\pi} \cdot \sqrt{\frac{2}{r_o}(1 - x_o/r_o)} \, .$$

In [12] the induced field of a dipole is also given. We will not give here the full equations of the general case of an arbitrary location of the dipole. There is, however, a simple case which is worth mentioning. Assume that the dipole is far away from the edge, i.e., $r_o >> x$, and located above the end of the plate so that $y_o >> x_o$ (see Fig. 3).

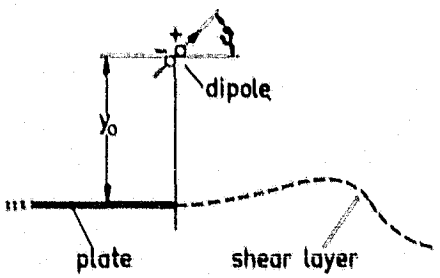

Fig. 3 Dipole as excitation of the shear layer.

The direction of the dipole is ϑ. In this case, we have, according to [12]:

$$(30) \qquad v_{1f} = \frac{1}{rx} \cdot \frac{D}{4\pi y_o^{3/2}} \cdot \cos(\vartheta - \pi/4),$$

where D is the dipole strength. As we see, v_{1f} becomes a maximum at $\vartheta = 45^o$. The direction of maximum efficiency ϑ_{max} of the dipole clearly changes with its position relative to the semi-infinite plate (see also [12]). For a position close to the shear layer, we will have, as expected, $\vartheta_{max} = 90^o$. If we use a vibrating cylinder to create a dipole, we have for the dipole strength $D = u_c \cdot 2\pi R^2$ where R is the cylinder radius and u_c is the velocity $u_c = u_o \cdot e^{-i\omega t}$ of the cylinder. Similar expressions can be given

for a vibrating ribbon in the fluid at rest [12]. *) The general finding is that in almost all conceivable cases we create a field close to the plate edge where $v_{1f} \propto 1/\sqrt{x}$. There are only a few singular cases where we create a stagnation point at the plate edge, like the "zero" position of the dipole in eq. (30). In section 4 it will be shown, that this region close to the edge where $v_{1f} \propto 1/\sqrt{x}$ is in fact the relevant one for the whole interaction process.

As we will show now, $v_{1f} \propto 1/\sqrt{x}$ corresponds to a parabolic pressure field around the edge. This fact is of particular significance for the choice of a suitable reference quantity for the excitation in real experimental situations. Since it is often impossible to track down the whole pressure field in a practical situation, we are looking for measurable quantities relevant to the interaction process.

To model a parabolic pressure field around the semi-infinite plate, we have to keep in mind, that analytic functions of $z=x\pm iy$ are solutions of $\nabla^2 p_f = 0$ and that we can use conformal mapping to fulfill the boundary conditions at the semi-infinite plate. We start with the consideration of a plane pressure field (see Fig.4)

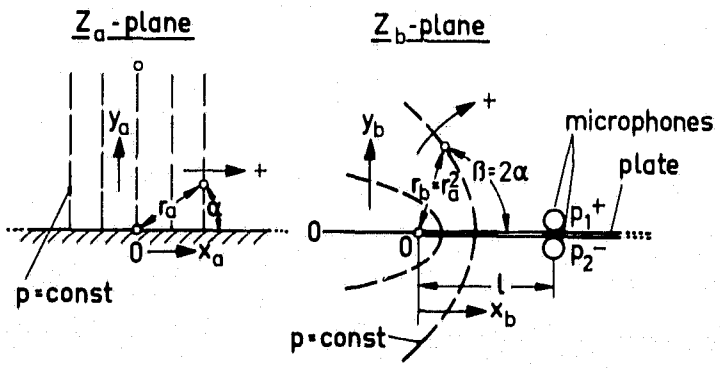

Fig. 4 Plane pressure field, parabolic pressure field.

*) If the vibrating ribbon operates within the flow regime at $y < 0$, the generated pressure field is, however, completely different, due to the interaction with the flow.

This pressure field in the z_a-plane ($z_a = x_a + iy_a$) has vertical lines as lines of constant pressure (we suppress the time dependence $e^{-i\omega t}$ for convenience). This would be the pressure field of a horizontal velocity fluctuation u constant throughout the plane. In the z_a-plane we have $p = A \cdot x_a$. If we apply the conformal mapping function $z_b = z_a^2$ we have for a point $z_a = x_a + iy_a = r_a e^{i\alpha}$ a conversion to the point $z_b = x_b + iy_b = r_b e^{i\beta} = z_a^2 = r_a^2 e^{2i\alpha}$ (see Fig. 4).

For the pressure we obtain:

$$(31) \qquad p = A \cdot x_a = A \cdot \mathrm{Re}\{z_a\} = A \cdot \mathrm{Re}\{\sqrt{z_b}\} = A \cdot \sqrt{r_b} \cdot \cos\frac{\beta}{2} .$$

For $\beta = o$ (above the semi-infinite plate) we have $p_1 = A\sqrt{x_b}$ and for $\beta = 2\pi$ we have $p_2 = -A\sqrt{x_b}$ (below the semi-infinite plate). At the location 1 of the reference microphones we have

$$(32) \qquad p_1 - p_2 = \Delta p_{12} = 2A\sqrt{l} .$$

With this equation we can eliminate A and find

$$(33) \qquad p = \frac{\Delta p_{12}}{2\sqrt{l}} \cdot \sqrt{r_b} \cos\frac{\beta}{2} .$$

To obtain v_{1f} we take the derivative $\frac{\partial p}{\partial y}$ at $y = o$ and $x < o$, which is equivalent to $-\frac{1}{v}\frac{\partial p}{\partial \beta}$ at $\beta = \pi$.

$$(34) \qquad -\frac{1}{r}\frac{\partial p}{\partial \beta}\ (\beta = \pi) = +\frac{\Delta p_{12}}{4\sqrt{l r_b}} .$$

Since our plate (see Fig. 2) should be extended from $x = -\infty$ to $x = o$, and since we want to have our result in Cartesian coordinates, we write

$$(35) \qquad \frac{\partial p}{\partial y}\ (x > o,\ y = o) = +\frac{\Delta p_{12}}{4\sqrt{lx}} .$$

Using eq. (24) we can relate this expression to v_{1f}

$$(36) \qquad \boxed{v_{1f} = -\frac{1}{\sqrt{x}} \cdot \frac{i\Delta p_{12}}{4\rho\omega\sqrt{l}}}$$

This is the desired relation between a quantity easily measurable such as the pressure difference Δp_{12} at the plate taken at a distance l from the lip. This quantity, Δp_{12}, contains no contributions from the shear layer. We feel, therefore, that Δp_{12} is the most suitable reference quantity for the excitation of the shear layer.

Since we have with eq. (36) a distribution of the excitation field v_{1f} which is valid in almost all conceivable cases, we can proceed to solve eq. (23), the differential equation for the shear layer motion. After inserting v_{1f} (eq. (36)) into eq. (23) we have

$$(37)\quad v_1 = \frac{i\Delta p_{12}}{4\rho\bar{v}_0\omega T}\left[e^{\lambda_1 x}\int_{G_1}^{x}\frac{e^{-\lambda_1 x}}{\omega x}\,dx - e^{\lambda_2 x}\int_{G_2}^{x}\frac{e^{-\lambda_2 x}}{\omega x}\,dx\right].$$

The lower boundaries G_1 and G_2 will produce contributions to the solution of the Helmholtz-type. Since v_1 must be zero for $x < 0$ these are truncated Helmholtz-solutions starting at $x = 0$. In appendix C we prove that such solutions cannot fulfill the condition of equal pressure at both sides of the shear layer and that there is no combination of G_1 and G_2 fulfilling this condition. This calculation in the appendix is based on calculating v_2 from v_1 using the condition of equal deformation of the shear layers (eq. (10)). Subsequently the corresponding u_1 and u_2 distributions are calculated using a source distribution approach. Finally, using the first Euler equation (eq. (1)), $\partial p_1/\partial x$ and $\partial p_2/\partial x$ are compared. Since $\partial p_1/\partial x$ and $\partial p_2/\partial x$ are incompatible under all conceivable situations, we can conclude, that <u>there are no unforced (free) vibrations of the shear layer</u>. This is, by the way, one of the essential results of the present investigation.

Since we have $G_1 = G_2 = 0$, we are left with a forced solution only, for which we have to prove that it fulfills the conditions of equal deformation and equal pressure at both sides of the shear layer. This is done in several steps:

(i) v_1 is calculated in an unambiguous way from eq. (37) with $G_1 = G_2 = o$. Subsequently, v_2 can be determined in an unambiguous way using eq. (10).

(ii) by a separate procedure (section 2.2.) analytic solutions for u_1 and u_2 are generated. We end up with a differential equation for u_1 very similar to eq. (37). The free constants there are determined by the compatibility with the v_1 and v_2 solutions in the far field.

(iii) Since we found no direct approach to relate the analytically obtained u_1 to v_1 and u_2 to v_2 in the near field, this was done using a numerical procedure. It is a by-product of the calculation of u_2 in the whole field (not only for $y = o$) which had to be carried out for a comparison between theory and experiment.

(iv) it is shown, that the analytic solution for u_1 and u_2 leads to zero pressure difference at both sides of the shear layer ($x > o$) and also to the expected pressure difference of the excitation field at the semi-infinite plate ($x < o$).

As we see, all ambiguities and, hopefully, all doubts are removed by this chain of procedures. The first step (i) is then to evaluate eq. (37) with $G_1 = G_2 = o$. After some suitable substitutions (see [12] for details) and introducing the error function defined as

$$(38)\quad \operatorname{erf} z = \frac{2}{\sqrt{\pi}} \int_0^z e^{-s^2} ds$$

we have

$$(39)\quad v_1 = \frac{\Delta p_{12}}{\rho \bar{U}_o \sqrt{I}} \cdot \frac{i\sqrt{\pi}}{4} \left[\frac{e^{\lambda_1 x}}{\sqrt{\lambda_1}} \operatorname{erf}\sqrt{\lambda_1 x} - \frac{e^{\lambda_2 x}}{\sqrt{\lambda_2}} \operatorname{erf}\sqrt{\lambda_2 x} \right]$$

and with eq. (10)

$$(40)\quad v_2 = -\frac{\Delta p_{12}}{\rho \bar{U}_o \sqrt{I}} \cdot \frac{\sqrt{\pi}}{4} \left[\frac{e^{\lambda_1 x}}{\sqrt{\lambda_1}} \operatorname{erf}\sqrt{\lambda_1 x} + \frac{e^{\lambda_2 x}}{\sqrt{\lambda_2}} \operatorname{erf}\sqrt{\lambda_2 x} \right]$$

using the abbreviations

$$(22) \qquad \lambda_1 = \frac{\omega}{\bar{U}_o}(i+1); \quad \lambda_2 = \frac{\omega}{\bar{U}_o}(i-1),$$

It is useful to define dimensionless quantities as follows:
A dimensionless wave number

$$(41) \qquad \tilde{\lambda}_1 = i + 1; \quad \tilde{\lambda}_2 = i - 1,$$

a dimensionless distance

$$(42) \qquad \tilde{x} = \frac{\omega x}{\bar{U}}$$

which will be used in the same way for y; and a dimensionless velocity*)

$$(43) \qquad \tilde{v} = \frac{v \cdot \rho \cdot \sqrt{\omega \bar{U}_o l}}{\Delta p_{12}}$$

which depends on quantities which can be measured easily. The same form will be also applied to u. After introduction of these dimensionless quantities we have:

$$(44) \qquad \tilde{v}_1 = \frac{i\sqrt{\pi}}{4}\left[\frac{e^{\tilde{\lambda}_1\tilde{x}}}{\sqrt{\tilde{\lambda}_1}}\,\mathrm{erf}\sqrt{\tilde{\lambda}_1\tilde{x}} - \frac{e^{\tilde{\lambda}_2\tilde{x}}}{\sqrt{\tilde{\lambda}_2}}\,\mathrm{erf}\sqrt{\tilde{\lambda}_2\tilde{x}}\right]$$

$$(45) \qquad \tilde{v}_2 = -\frac{\sqrt{\pi}}{4}\left[\frac{e^{\tilde{\lambda}_1\tilde{x}}}{\sqrt{\tilde{\lambda}_1}}\,\mathrm{erf}\sqrt{\tilde{\lambda}_1\tilde{x}} + \frac{e^{\tilde{\lambda}_2\tilde{x}}}{\sqrt{\tilde{\lambda}_2}}\,\mathrm{erf}\sqrt{\tilde{\lambda}_2\tilde{x}}\right]$$

Fig. 5 shows a plot of eqs. (44) and (45) where $\tilde{v}_1$ and $\tilde{v}_2$ have been split into their real and imaginary parts, respectively.

*) Based on dimensional considerations, similar dimensionless quantities had been defined in [12]; the relation to these is: $\tilde{v} = -i\frac{v^*_{FK}}{2}$ and $\tilde{x} = x^*$.

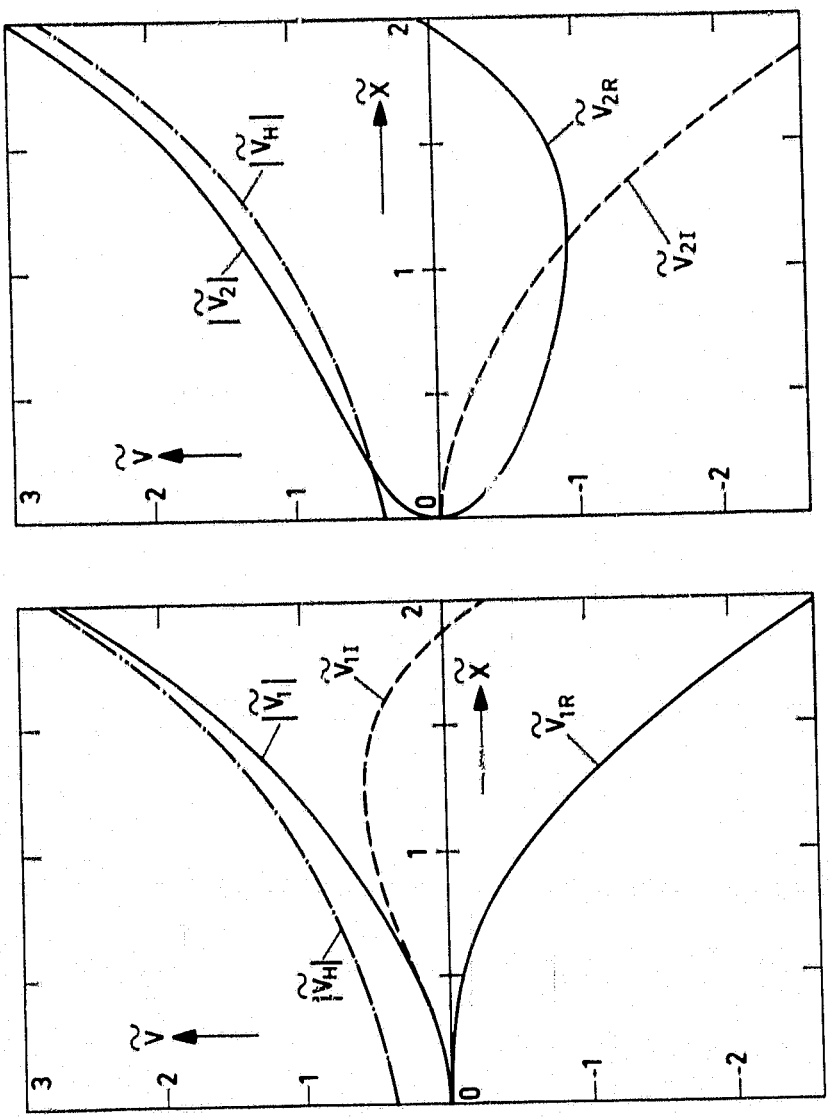

Fig. 5 v-velocity components on both sides of the shear layer.

Tables of numerical values of v_1 and v_2 will be shown in appendix D. Subsequently, we will investigate the behaviour for small and large $\tilde{x}$, because this provides some additional insight into the interaction process.

For small $\tilde{x}$ we take advantage of the expansion given in [31]

$$(46) \qquad \operatorname{erf} z = \frac{2}{\sqrt{\pi}} \cdot e^{-z^2} \cdot \sum_{n=0}^{\infty} \frac{2^n}{1 \cdot 3 \ldots (2n+1)} z^{2n+1} ;$$

we obtain for small x

$$(47) \qquad \tilde{v}_1 \sim \tilde{x}^{1.5} \; ; \; \tilde{v}_2 \sim \sqrt{\tilde{x}}$$

which shows, that there is no singularity of v_1 or v_2 anymore near the trailing edge. In addition, it is shown by eq. (47), that the flow leaves the trailing edge without a jump in the slope. This is equivalent to the presence of a Kutta condition.

A question of particular interest is the far field behaviour of equations (44) and (45). By virtue of the far field expansion of the function erf z, given in [31]

$$(48) \qquad \underset{z \to \infty}{\sqrt{\pi}\, z e^{z^2} \operatorname{erfc} z} \; : \; 1 + \sum_{m=1}^{\infty} (-1)^m \frac{1 \cdot 3 \ldots (2m-1)}{(2z^2)^m} ,$$

with erfc z= 1 - erf z we obtain for large z, where the summation term can be neglected:

$$(49) \qquad \tilde{v}_{1\,(\tilde{x} \to \infty)} = \frac{i\sqrt{\pi}}{4} \cdot \frac{e^{\tilde{\lambda}_1 \tilde{x}}}{\sqrt{\tilde{\lambda}_1}} - \frac{i}{4\sqrt{\tilde{x}}}$$

$$(50) \qquad \tilde{v}_{2\,(\tilde{x} \to \infty)} = -\frac{\sqrt{\pi}}{4} \cdot \frac{e^{\tilde{\lambda}_1 \tilde{x}}}{\sqrt{\tilde{\lambda}_1}} - \frac{i}{4\sqrt{\tilde{x}}}$$

with $\tilde{\lambda}_1 = i + 1$. It is evident, that the field has separated into an amplified Helmholtz-type wave (1st term of eqs. (49) and (50),

respectively) and the contribution of the exterior excitation v_{1f}, which is the second term in both equations. This latter contribution is transmitted through the shear layer without any change. If we call the first term in the equations v_H (where H stands for Helmholtz solution), we may write equations (49) and (50)

$$(51) \qquad \tilde{v}_{1_{(\tilde{x}\to\infty)}} = \tilde{v}_{1H} + \tilde{v}_{1f} \; ; \; \tilde{v}_{2_{(\tilde{x}\to\infty)}} = \tilde{v}_{2H} + \tilde{v}_{1f} .$$

It is interesting to see where this far field solution emerges i.e., beyond which distance $\tilde{x}$ amplified instability wave and excitation can be split. In order to investigate this, we subtract the asymptotic instability wave from the complete solution

$$(52) \qquad \tilde{v}_{1D} = \tilde{v}_1 - \tilde{v}_{1H} \overset{?}{=} v_{1f} \; ; \; \tilde{v}_{2D} = \tilde{v}_2 - \tilde{v}_{2H} \overset{?}{=} v_{2f} .$$

The differences $\tilde{v}_{1D}$ and $\tilde{v}_{2D}$ are plotted in Fig. 6.

It is evident from Fig. 6 that the far field solution is valid beyond $\tilde{x} \approx 4 \div 6$, that is beyond about 2/3÷1 wavelength of the instability waves. This means, that the basic interaction takes place within $\frac{1}{2}$ wavelength of the instability waves. This latter finding, that the wave field can be separated into a predictable instability wave and the exterior excitation field (sound field) is one of the essential findings of this paper and it supports similar attempts made previously on a more heuristic basis [32]. This splitting is therefore admissible at distances greater than about 1/2÷1 wavelengths of the instability waves. Finally, we provide also a simple formula for the magnitude (modulus) of the excited instability wave:

$$(53) \qquad |\tilde{v}_{1_H}| = |\tilde{v}_{2_H}| = \frac{\sqrt{\pi}}{4 \cdot \sqrt[4]{2}} \cdot e^{\tilde{x}} \qquad \text{for } \tilde{x} \geq 4 \div 6$$

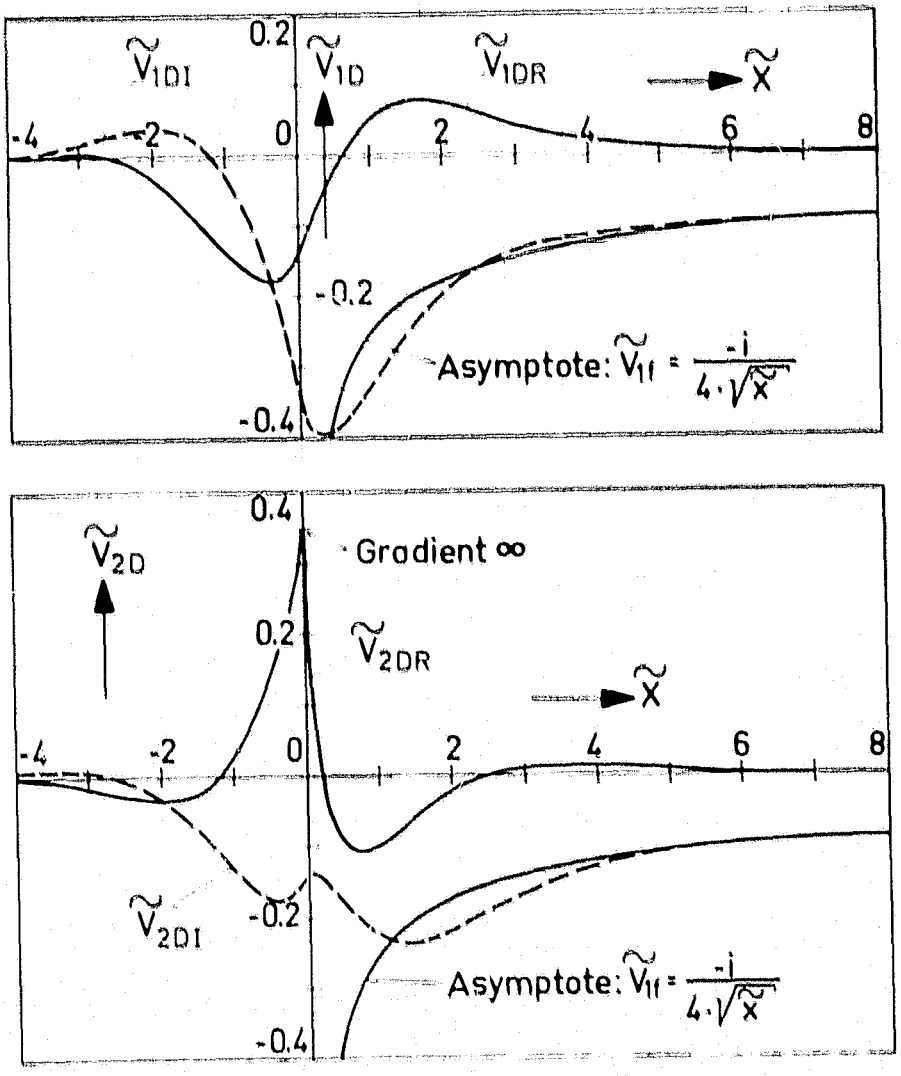

Fig. 6 Difference between complete far field velocity and asymptotic instability wave.

or, in dimensional quantities

$$(54) \qquad \boxed{|v_{1_{II}}| = |v_{2_{II}}| = \frac{\Delta p_{12}}{\rho\sqrt{\bar{U}_o \omega 1}} \cdot \frac{\sqrt{\pi}}{4\cdot\sqrt{2}} \, e^{\frac{\omega x}{\bar{U}_o}}}$$

Numerical values of v_1 and v_2 are given in appendix D.

Since v-velocity components are difficult to measure, we will, in the subsequent sections, both calculate u_1 and u_2 at $y = \pm o$ (analytic solutions) and will provide also numerically computed values of u_2 outside the shear layer in the potential field.

2.2. Differential equation for u

The procedure to obtain a differential equation for u is slightly less elegant than the one for v. We restrict ourselves, in addition, to the "parabolic" excitation, for which we obtained the special solutions, eqs. (44) and (45) in the preceding section. As we have shown before (see also section 4) the "parabolic" excitation case is valid in almost all conceivable situations. In addition, when dealing with u-velocities, we do not worry about causality; and if we encounter ambiguities, we can remove these by linking the u-solutions to the unambiguously known v-solutions. If we create, e.g., a parabolic pressure distribution around the semi-infinite plate it is irrelevant, therefore, whether this has been created by a singularity distribution at $y = \pm o$ or by a source at a large distance. As a consequence thereof, we do not split the field here into two contributions from the exterior source and the shear layer itself, respectively.

The first task in this section is to construct an equation for u out of the equation for equal displacement

$$(10) \qquad v_2 = v_1 + i\frac{\bar{U}_o}{\omega}\frac{\partial v}{\partial x} .$$

In [12] and in appendix C it is shown how a v-velocity condition can be created out of a u-velocity condition using a source

distribution approach. Here we will do the opposite, i.e., we will generate a u-velocity condition out of a v-velocity condition using a vorticity distribution approach.

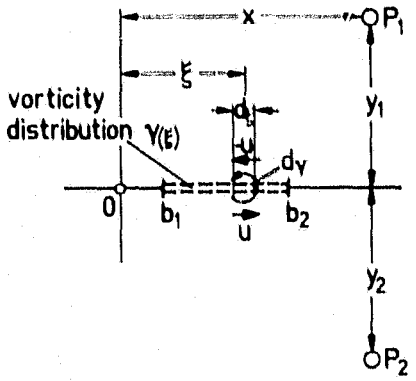

Fig. 7 Induction of a vorticity distribution on a straight line

We consider the velocities which are induced by a vorticity distribution on a straight line between b_1 and b_2 (see Fig. 7). The induced velocities u and v at a point P_1 above a vorticity distribution $\gamma(\xi)$ on the x-axis are:

$$(55)\quad \left\{ \begin{aligned} u &= -\frac{1}{2\pi} \int_{b_1}^{b_2} \frac{\gamma(\xi) \cdot y_1}{(x-\xi)^2+y_1^2}\, d\xi, \\ v &= \frac{1}{2\pi} \int_{b_1}^{b_2} \frac{\gamma(\xi) \cdot (x-\xi)}{(x-\xi)^2+y_1^2}\, d\xi. \end{aligned} \right\}$$

If the point P_1 approaches the x-axis ($+y_1 \to 0$), the u-component becomes $u = -\gamma(\xi)/2$. This fact can be verified if one analyzes the distribution $\gamma(\xi)$ into a series of small steps of locally constant $\gamma(\xi)$ and evaluates eq. (55). One finds that in the case of a vorticity distribution on a straight line no induced

u-component contributions can come from vorticity elements outside ξ (at $+y_1 \to o$). By inspection of Fig. 7 this is also obvious. For a point P_2 approaching the x-axis from below ($-y_2 \to o$) we have $u = +\gamma(\xi)/2$. With these considerations we obtain:

$$(56)\quad \left\{ \begin{array}{l} v_{(y=+o)} = -\frac{1}{\pi} \int_{b_1}^{b_2} \frac{u(\xi)}{x-\xi}\, d\xi \\ \\ v_{(y=-o)} = +\frac{1}{\pi} \int_{b_1}^{b_2} \frac{u(\xi)}{x-\xi}\, d\xi \end{array} \right\}$$

Inserting eq. (56) into eq. (10) and adjusting the limits b_1 and b_2 yields

$$(57)\quad \int_{-\infty}^{+\infty} \frac{u_2(\xi)}{x-\xi}\, d\xi = -\int_{-\infty}^{+\infty} \frac{u_1(\xi)}{x-\xi}\, d\xi - i\,\frac{\bar{U}_o}{\omega}\,\frac{\partial}{\partial x} \int_{-\infty}^{+\infty} \frac{u_1(\xi)}{x-\xi}\, d\xi\,.$$

Since we expect exponentially growing instability waves in the downstream direction we will run into difficulties with the upper limit of the integrals in eq. (57). To avoid this we will use a simple trick: we will subtract from the forced instability solutions the amplified Helmholtz solution u_H which has asymptotically the same magnitude as the forced instability wave. Consequently, we write

$$(58)\quad \int_{-\infty}^{+\infty} \frac{(u_2-u_{2H})}{x-\xi}\, d\xi + \int_{-\infty}^{+\infty} \frac{(u_1-u_{1H})}{x-\xi}\, d\xi + i\,\frac{\bar{U}_o}{\omega}\,\frac{\partial}{\partial x} \int_{-\infty}^{+\infty} \frac{(u_1-u_{1H})}{x-\xi}\, d\xi = o,$$

The evaluation of the third term in this equation uses integration by parts

$$(59)\quad \frac{\partial}{\partial x} \int_{-\infty}^{+\infty} \frac{(u_{1(\xi)}-u_{1H(\xi)})}{x-\xi}\, d\xi = -\int_{-\infty}^{+\infty} \frac{(u_{1(\xi)}-u_{1H(\xi)})}{(x-\xi)^2}\, d\xi =$$

$$= - \frac{(u_1(\xi)-u_{1II}(\xi))}{(x-\xi)} \Big|_{-\infty}^{+\infty} + \int_{-\infty}^{+\infty} \frac{\partial}{\partial \xi}\frac{(u_1(\xi)-u_{1II}(\xi))}{x-\xi}\, d\xi$$

The first (integrated) term on the right hand side becomes zero if (i) x remains finite, (ii) the difference (u_1-u_{1II}) does not grow faster than ξ for large negative and positve values of ξ. That the latter condition is fulfilled will be evident from the solution we are going to obtain; so we have

$$(60) \qquad \int_{-\infty}^{+\infty} \frac{(u_2-u_{2II})}{x-\xi}\, d\xi + \int_{-\infty}^{+\infty} \frac{(u_1-u_{1II})}{x-\xi}\, d\xi + i\,\frac{\bar{U}_o}{\omega} \int_{-\infty}^{+\infty} \frac{\partial}{\partial \xi}\frac{(u_1-u_{1II})}{x-\xi}\, d\xi ,$$

The integrals in eq. (60) each posses the same denominator and the same boundaries. We have a condition at least as restrictive if we write

$$(61) \qquad u_2 - u_{2II} + u_1 - u_{1II} + i\,\frac{\bar{U}_o}{\omega}\,\frac{\partial}{\partial x}\,(u_1-u_{1II}) = 0$$

where we have replaced ξ by x. Since we know that eq. (61) is fulfilled by the Helmholtz solution alone we can write

$$(62) \qquad \boxed{u_2 + u_1 + i\,\frac{\bar{U}_o}{\omega}\,\frac{\partial u_1}{\partial x} = 0}$$

It is valid for all x since eq. (10) was valid for all x. This is the desired second condition for u_1 and u_2. If we insert this equation into eq. (6) we obtain a differential equation for u_1 alone:

$$(63) \qquad \boxed{2u_1 + 2i\,\frac{\bar{U}_o}{\omega}\,\frac{du_1}{dx} - \left(\frac{\bar{U}_o}{\omega}\right)^2 \frac{d^2u_1}{dx^2} = -\frac{1}{\rho\omega}\,\frac{d(p_1-p_2)}{dx}}$$

We can obtain the pressure at both sides of a semi-infinite plate (located at $x < 0$) from eq. (33), after adjustment of

coordinates:

$$(64)\quad \left\{ \begin{array}{l} p_{1\ (y=+o)} = \dfrac{\Delta p_{12}}{2\sqrt{i}} \cdot \sqrt{-x} \\ p_{2\ (y=-o)} = -\dfrac{\Delta p_{12}}{2\sqrt{i}} \cdot \sqrt{-x} \end{array} \right\}$$

This can be used to find the right hand side of eq. (63)

$$(65)\quad 2u_1 + 2i\,\frac{\bar{U}_o}{\omega}\,\frac{du_1}{dx} - \left(\frac{\bar{U}_o}{\omega}\right)^2 \frac{d^2u_1}{dx^2} = \frac{1}{\sqrt{-x}} \cdot \frac{i\Delta p_{12}}{2\rho\omega\sqrt{i}}$$

for $x > o$ the right hand side of eq. (65) becomes zero, because, by definition, the pressure difference at both sides of the shear layer should be zero. In complete analogy to the procedure to solve the differential equation for v in the preceding section we obtain:

$$(66)\quad u_1 = \frac{i\Delta p_{12}}{4\rho\bar{U}_o\sqrt{i}} \left[e^{\lambda_1 x} \int_{G_3}^{x} \frac{e^{-\lambda_1 x}}{\sqrt{-x}}\,dx - e^{\lambda_2 x} \int_{G_4}^{x} \frac{e^{-\lambda_2 x}}{\sqrt{-x}}\,dx \right].$$

We should keep in mind, as mentioned before, that there exists a contribution to the integrals only for $x < o$. Consequently, <u>we have for $x > o$ only contributions of the Helmholtz instability wave type</u>, created by the lower boundaries of the integrals G_3 and G_4 in eq. (66).

An unambiguous way to find the magnitude of these Helmholtz-type contributions is to relate them to the asymptotic magnitude of the v instability waves. These v instability waves also behave like Helmholtz-type solutions for distances $\frac{\omega x}{U_o} \geq 4 \div 6$. We should find out, therefore, what the coupling between the u and the v-components in the Helmholtz instability waves is. The easiest way to do this is to start out with the potential of the induced velocity field of these waves:

$$(67)\quad \left\{ \begin{array}{l} \phi_1 \ (y > o) = Ae^{\lambda_{1,2}(x+iy)} \\ \phi_2 \ (y < o) = Be^{\lambda_{1,2}(x-iy)} \end{array} \right\}$$

we take the derivatives

$$(68)\quad \left\{ \begin{array}{l} \frac{\partial \phi_1}{\partial y} = v_1 = i\lambda_{1,2} Ae^{\lambda_{1,2}(x+iy)} \\ \\ \frac{\partial \phi_1}{\partial x} = u_1 = \lambda_{1,2} Ae^{\lambda_{1,2}(x+iy)} \\ \\ \frac{\partial \phi_2}{\partial y} = v_2 = -i\lambda_{1,2} Be^{\lambda_{1,2}(x-iy)} \\ \\ \frac{\partial \phi_2}{\partial x} = u_2 = \lambda_{1,2} Be^{\lambda_{1,2}(x-iy)} \end{array} \right\}$$

Therefore we have $u_1 = -iv_1$ and $u_2 = iv_2$ at $y = o$. With the solutions for v_1 (eq. (44)) and v_2 (eq. (45)), we obtain (with u nondimensionalized as in eq. (43)):

$$(69)\quad \left\{ \begin{array}{l} \tilde{u}_1 = \frac{\sqrt{\pi}}{4} \left[\frac{e^{\tilde{\lambda}_1 \tilde{x}}}{\sqrt{\tilde{\lambda}_1}} - \frac{e^{\tilde{\lambda}_2 \tilde{x}}}{\sqrt{\tilde{\lambda}_2}} \right] \\ \\ \tilde{u}_2 = \frac{i\sqrt{\pi}}{4} \left[\frac{e^{\tilde{\lambda}_1 \tilde{x}}}{\sqrt{\tilde{\lambda}_1}} + \frac{e^{\tilde{\lambda}_2 \tilde{x}}}{\sqrt{\tilde{\lambda}_2}} \right] \end{array} \right\} \quad \text{for } x > o$$

with $\tilde{u} = \dfrac{u \cdot \rho\sqrt{\omega U_o l}}{\Delta p_{12}}$; $\tilde{x} = \dfrac{\omega x}{U_o}$; $\tilde{\lambda}_1 = i + 1$; $\tilde{\lambda}_2 = i - 1$.

Analytic solutions of this type had not been published before, but they were obtained already with different mathematical

methods by W. Möhring [33] and M.S. Howe [34]. To find solutions for $x < o$ we have to proceed analogously to section 2.1. The only difference is, that we now have additional Helmholtz-type solutions in contrast to the situation for the component v. After some algebra we end up with

(70)
$$\left.\begin{aligned} \tilde{u}_1 &= \frac{\sqrt{\pi}}{4}\left[\frac{e^{\tilde{\lambda}_1\tilde{x}}}{\sqrt{\tilde{\lambda}_1}}\,\mathrm{erfc}\sqrt{\tilde{\lambda}_1\tilde{x}} - \frac{e^{\lambda_2 x}}{\sqrt{\tilde{\lambda}_2}}\,\mathrm{erfc}\,\sqrt{\tilde{\lambda}_2\tilde{x}}\right] \\ \tilde{u}_2 &= -i\frac{\sqrt{\pi}}{4}\left[\frac{e^{\tilde{\lambda}_1\tilde{x}}}{\sqrt{\tilde{\lambda}_1}}\,\mathrm{erfc}\,\sqrt{\tilde{\lambda}_1\tilde{x}} + \frac{e^{\tilde{\lambda}_2\tilde{x}}}{\sqrt{\tilde{\lambda}_2}}\,\mathrm{erfc}\,\sqrt{\tilde{\lambda}_2\tilde{x}}\right] \end{aligned}\right\} \quad \text{for } x<o$$

x has to be inserted into these equations with its negative sign. The abbreviations are identical to those used in eqs (69), (44) and (45). Since erfc is defined as erfc z = 1-erf z, it is obvious that equations (69) and (70) merge into each other at x = o. If one expands eq. (70) for large negative x, one can show that the wave structure of the instability waves vanishes and the prevailing terms are proportional to $u \propto 1/\sqrt{-x}$. In addition, it can be shown using the first Euler equation (1), that eq. (70) produces the correct pressure difference at both sides of the semi-infinite plate.

For large positive values we have from eq. (69)

(71)
$$|u_1| = |u_2| = \frac{\Delta p_{12}}{\rho\sqrt{\bar{U}_o\omega l}} \cdot \frac{\sqrt{\pi}}{4\cdot\sqrt{2}}\, e^{\frac{\omega x}{\bar{U}_o}}$$
for $x \gtrsim \bar{U}_o/f$

which is the same result as eq. (54) for v at large x. The only difference is, however, that the excitation velocity has no component in the u-direction for $x > o$.

There is yet another less obvious feature of the exact solution, eq. (71), near x = y = o. If one wants to verify eq. (71) experimentally, one might take, e.g., data of the velocity u_2

in the region outside the shear layer and would extrapolate these data into the shear layer. However, this would lead to erroneous results near $x = y = o$ (plate edge). The reason is, that the gradient of a curve $u_2(y)$ for constant x would be infinite at $x = y = o$, which hardly allows any sensible extrapolation towards $y \to o$ from data at $y \neq o$. The reason for this is the following. In the potential flow region outside the shear layer the vorticity should be zero, i.e., $\partial u_2/\partial y - \partial v_2/\partial x = o$. Since $v_2 \propto \sqrt{x}$ for small x, $\partial u_2/\partial y$ must become infinite (but, certainly, not u_2 itself). Thus, the exact solution for u_2 (eq. (69)) is only of limited value if it comes to comparing it with experimental data. This is the reason why the u_2 velocity field for finite y has to be calculated numerically. After this will have been done in the next section,and the induced u_2-field is available, the discussion in this paragraph will also become more convincing.

3. Field calculations

For a comparison with experiments it is necessary to calculate velocities also outside the shear layer. The quantity which can be measured most easily and accurately is the velocity u_2 in the flow region $y < o$. A source distribution approach is used to compute u_2 from v_2, which is given for all x. Actual data of v_2, i.e., its real and imaginary part can be found in Appendix D and curves can be seen in Figs. 5 and 6 in section 2.1. The source distribution approach we use here is identical to that used in [12] or in Appendix C; there is also a formal similarity to the vorticity approach used in section 2.2.

We consider first a source distribution $q(\xi)$ on the x-axis (see Fig. 8)

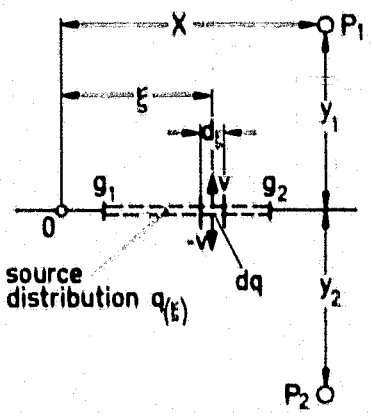

Fig. 8 Induction of a source distribution.

The induced u-velocity component at a point p_1 <u>above</u> a line source distribution $q(\xi)$ is

$$u = \frac{1}{2\pi} \int_{g_1}^{g_2} \frac{q(\xi) \cdot (x - \xi)}{(x_1 - \xi)^2 + y_1^2} \, d\xi \,. \tag{72}$$

For a point p_2 <u>below</u> the line source distribution we end up with the same result. If the point P_1 approaches the x-axis ($+y_1 \to o$) the v-component becomes $+q(\xi)/2$. For the case of a source distribution on a straight line no induced v-component contributions can come from sources outside ξ at $y_1 \to o$. So $q(\xi)$ can be replaced by $2v$ for $y > o$. For negative y we obtain negative induced v-components from positive source strengths $q(\xi)$. Thus we have for negative y

$$u_2 = -\frac{1}{\pi} \int_{g_1}^{g_2} \frac{v_2(\xi) \cdot (x_2 - \xi)}{(x_2 - \xi)^2 + y_2^2} \, d\xi \,. \tag{73}$$

This is the type of equation which provides the relation between

v_2 and u_2. It will be evaluated numerically. Formally, we would have to integrate from $g_1 = -\infty$ to $g_2 = +\infty$. However, we again encounter difficulties with the upper limit, because v_2 grows exponentially. This difficulty will be circumvented in the same way as we did it before. We subtract the exponentially growing asymptote v_{2H} to obtain an integrable function. The difference $v_{2D} = v_2 - v_{2H}$ is only proportional to $1/\sqrt{x}$ for large positive x and becomes zero exponentially at large negative x. After having carried out the integration we add the induced field of the asymptote v_{2H} (see eq. (68)) to obtain the complete u_2-distribution. This whole procedure has to be carried out separately for the real and imaginary part of v_2 to obtain the real and imaginary part of u_2.

The integration of u_2 is then split into three regimes:

(i) For large values of $\tilde{x}$ the real part v_{2DR} of v_{2D} becomes zero and the imaginary part v_{2DI} of v_{2D} is proportional to $1/\sqrt{\tilde{x}}$ (see Fig. 6). Thus, for values between, say, $\tilde{x} = 6$ and $\tilde{x} = \infty$ we will use the asymptotic form of v_{2DI}, insert it into eq. (73) and will carry out the integration in closed form. This will take care of the contribution to the integral (73) for large values of $\tilde{x}$ (or ξ).

(ii) For small positive $\tilde{x}$ the real part v_{2R} of v_2 has a parabolic behaviour with $v_{2R} \propto \sqrt{\tilde{x}}$. Caused by this, the slope of v_{2DR} is infinite for $x = +o$. Since this can lead to numerical problems we will also integrate the region between $\tilde{x} = o$ and $\tilde{x} = 0.1$ in closed form.

(iii) The remainder of the integral from, say, $\tilde{x} = -6$ (where $v_2 = o$) to $\tilde{x} = o$ and from $\tilde{x} = 0.1$ to $x = +6$, where the asymptotic solution takes over, is calculated using a step integration procedure with intervals of $\Delta\tilde{x} = 0.1$. The step integration elements are trapezoidal pieces where the upper and the lower limits have the same values as the function v_{2DR} (or v_{2DI}). This provides a much better accuracy than ordinary rectangular steps would do.

For each of these integration elements (i) + (iii) we have to produce analytical solutions. We start with the far field influence (i). For large values of $\tilde{x}$ we have for v_{2DI} from eq. (50):

$$\tilde{v}_{2DI} \overset{(\text{far field})}{=} -\frac{1}{4\sqrt{\tilde{x}}} \,. \tag{74}$$

For u_2, x and ξ we use the nondimensionalized form to obtain

$$\tilde{u}_{2DI} \overset{(\text{far field})}{=} +\frac{1}{4\pi} \int_{\tilde{\xi}_1}^{\infty} \frac{1}{\sqrt{\tilde{\xi}}} \cdot \frac{(\tilde{x}-\tilde{\xi})}{(\tilde{x}-\tilde{\xi})^2-\tilde{y}^2} \, d\tilde{\xi} \,. \tag{75}$$

We will not find this type of integral in the usual integral tables. However, it can be simplified by complex fraction decomposition using the following relation

$$\frac{\tilde{x}-\tilde{\xi}}{(\tilde{x}-\tilde{\xi})^2+\tilde{y}^2} = \frac{1}{2}\left[\frac{1}{z-\tilde{\xi}} + \frac{1}{\bar{z}-\tilde{\xi}}\right] \tag{76}$$

with

$$z = \tilde{x} + i\tilde{y} \,, \quad \bar{z} = \tilde{x} - i\tilde{y} \,. \tag{77}$$

Thus we have for (75)

$$\tilde{u}_{2DI} \overset{(\text{far field})}{=} \frac{1}{8\pi} \int_{\tilde{\xi}_1}^{\infty} \frac{d\tilde{\xi}}{\sqrt{\tilde{\xi}}\,(z-\tilde{\xi})} + \frac{1}{8\pi} \int_{\tilde{\xi}_1}^{\infty} \frac{d\tilde{\xi}}{\sqrt{\tilde{\xi}}\,(\bar{z}-\tilde{\xi})} \,. \tag{78}$$

Integrals of this kind can be found, e.g., in [38]. The total integral turns out, as it should, to be completely real. We obtain after some algebra:

$$(79)\qquad \tilde{u}_{2DI} = \frac{1}{4\pi\sqrt{\tilde{r}}}\left[\frac{1}{2}\cdot\cos\frac{\vartheta}{2}\cdot\ln\left(\frac{\tilde{r}+\tilde{\xi}_1-2\sqrt{\tilde{\xi}_1\tilde{r}}\,\cos\vartheta/2}{\tilde{r}+\tilde{\xi}_1+2\sqrt{\tilde{\xi}_1\tilde{r}}\,\cos\vartheta/2}\right)+\right.$$

$$\left.+\sin\frac{\vartheta}{2}\cdot\arctan\left(\frac{2\sqrt{\tilde{\xi}_1\tilde{r}}\,\sin\vartheta/2}{\tilde{r}-\tilde{\xi}_1}\right)-\pi\sin\frac{\vartheta}{2}\right]$$

with $\tilde{r} = \sqrt{\tilde{x}^2+\tilde{y}^2}$ and $\vartheta = \arctan(\tilde{y}/\tilde{x})$, and for

$\tilde{\xi}_1$ in the order of 6.

The second (ii) particular element of the integration is tackled in a similar way. The expansion for v_{2R} (the real part of v_2) yields for small $\tilde{x}$

$$(80)\qquad \tilde{v}_{2R} = -\sqrt{\tilde{x}}\,,$$

Therefore, we have to integrate

$$(81)\qquad \underset{(\text{small }\tilde{x})}{\tilde{u}_{2R}} = +\frac{1}{\pi}\int_0^{\tilde{\xi}_2}\frac{\sqrt{\tilde{\xi}}\,(\tilde{x}-\tilde{\xi})}{(\tilde{x}-\tilde{\xi})^2+\tilde{y}^2}\,d\tilde{\xi}$$

for ξ_2 in the order of o.1. we proceed in a way very similar to that shown above and end up after some intermediate calculations:

$$(82)\qquad \underset{(\text{small }x)}{\tilde{u}_{2R}} = \frac{\sqrt{\tilde{r}}}{\pi}\left[-\frac{1}{2}\cdot\cos\frac{\vartheta}{2}\cdot\ln\left(\frac{\tilde{r}+\tilde{\xi}_2-2\sqrt{\tilde{\xi}_2\tilde{r}}\,\cos\vartheta/2}{\tilde{r}+\tilde{\xi}_2+2\sqrt{\tilde{\xi}_2\tilde{r}}\,\cos\vartheta/2}\right)+\right.$$

$$\left.+\sin\frac{\vartheta}{2}\cdot\arctan\left(\frac{2\sqrt{\tilde{\xi}_2\tilde{r}}\,\sin\vartheta/2}{\tilde{r}-\tilde{\xi}_2}\right)\right]-\frac{2\sqrt{\tilde{\xi}_2}}{\pi}$$

with r and ϑ defined as before.

This result has most terms in common with eq. (79) which suggests, that the same computer subroutines can be used.

The third (iii) element is the trapezoidal element mentioned before (see Fig. 9)

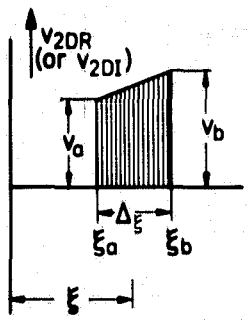

Fig. 9 Trapezoidal velocity element as inducing source element. $v = -\frac{1}{2} \cdot$ source strength.

The local distribution of v_{2D} (in the computation specified as v_{2DR} and v_{2DI}) is

$$\tilde{v}_{2D} = \tilde{v}_a + m\,(\tilde{\xi} - \tilde{\xi}_a) \tag{83}$$

with

$$m = \frac{\tilde{v}_b - \tilde{v}_a}{\tilde{\xi}_b - \tilde{\xi}_a} = \frac{\tilde{v}_b - \tilde{v}_a}{\Delta\tilde{\xi}} \,. \tag{84}$$

The integral

$$\Delta\tilde{u}_{2D} = -\frac{1}{\pi} \int_{\tilde{\xi}_a}^{\tilde{\xi}_b} \frac{(\tilde{v}_a + m(\tilde{\xi}-\tilde{\xi}_a)) \cdot (\tilde{x}-\tilde{\xi})}{(\tilde{x}-\tilde{\xi})^2+\tilde{y}^2}\, d\tilde{\xi} \tag{85}$$

can be solved analytically using the integral table in [35]. One obtains after some intermediate calculations:

$$(86)\qquad \Delta u_{2D} = -\frac{v_b - v_a}{v_a \cdot v_b}\left| y\left(\arctan\left(\frac{\xi_b - x}{\tilde{y}}\right) - \arctan\left(\frac{\xi_a - x}{\tilde{y}}\right)\right) - \right.$$

$$\left. - \left(\frac{v_a \cdot \Delta\xi}{v_b - v_a} - (\xi_a - x)\right) \cdot \frac{1}{2}\ln\frac{r_b^2}{r_a^2} - \Delta\xi \right|$$

with

$$(87)\qquad r_b^2 = (x - \xi_b)^2 + y^2 \text{ and } r_a^2 = (x - \xi_a)^2 + \tilde{y}^2,$$

This element (iii) will be used in all situations where v_{2D} is not zero or where the asymptotic solutions (i) and (ii) are not used.

At the end of the computations, the asymptotic solution u_{2H} (using eq. (68)) is added to obtain $u_2 = u_{2D} + u_{2H}$. The details of the computations are given in appendix E as well as tables with computed values of u_2. Here, we will show the modulus of u_2, because it can be measured in a straightforward way. In Fig. 10 a computed diagram of $|u_2|$ as a function of $\tilde{y}$ for various $\tilde{x}$ can be seen. We have used a logarithmic plot on the vertical axis of this figure. This allows to identify regions of the curves which show exponential behaviour; they will occur as straight lines.

After inspection of Fig. 10 we find that the curves for $|\tilde{u}_2|$ at $\tilde{x} > 1$ show an exponential decay in the -y direction. With equations (68) and (71) we can predict the induced velocities of the amplified instability wave; we obtain

$$(88)\qquad |\tilde{u}_2| = \frac{\tilde{a}}{4 \cdot \tilde{\alpha}^2} \cdot e^{\tilde{x}} \cdot e^{-|\tilde{y}|},$$

$$(\tilde{x} > 1.5)$$

This asymptotic behaviour is also given in the dotted lines in the upper half of Fig. 9. As we see, eq. (88) provides reasonable predictions already for $\tilde{x} > 1.5$. This indicates clearly, that

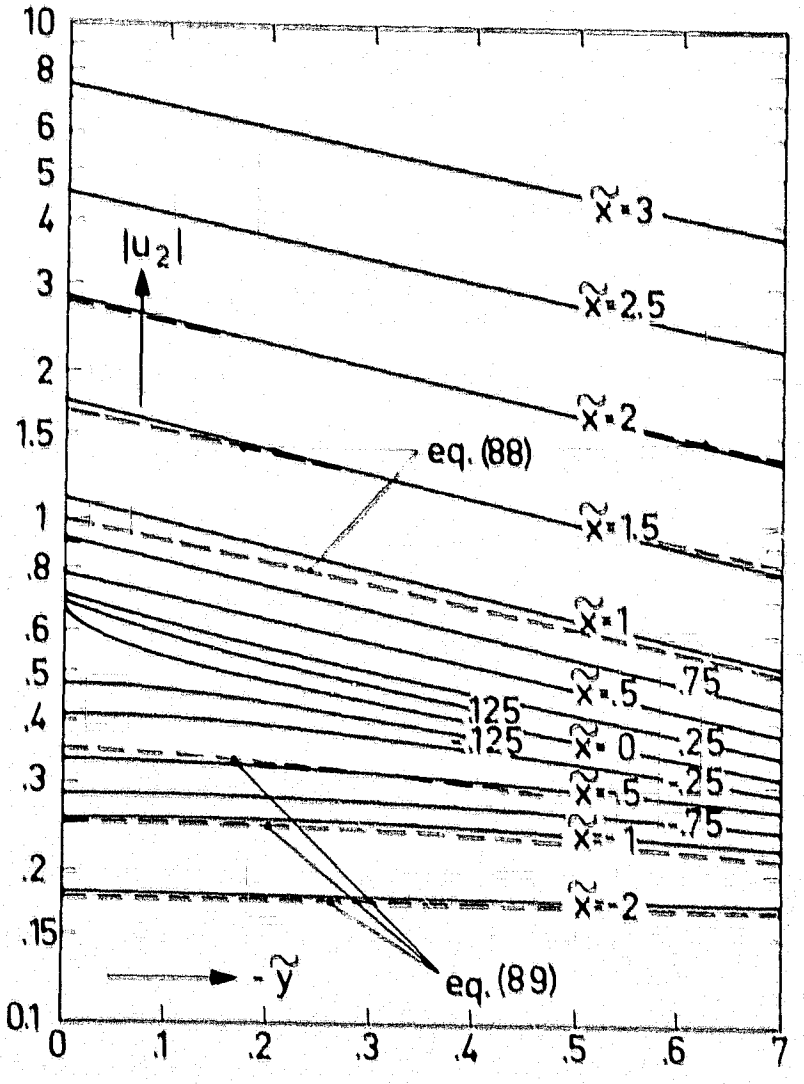

Fig. 10 Computed distribution of $|u_2|$ for various x and y.

downstream of, say, $\tilde{x} = 1 \div 1.5$ the instability waves dominate the induced $\tilde{u}$-field in the potential region outside the shear layer. It can be assumed, that this feature is exhibited more clearly in the u-component than in the v-component. This is due to the fact that the excitation has no u-component for positive x and small y (compare equation (69) for u and equations (49) and (50) for v).

One might argue, that there is also an asymptotic equation for $|u_2|$ at large negative x. In the region upstream of the plate edge, it is reasonable to assume that the excitation field dominates. Since the excitation pressure field is known (see eq. (33), note that x is inverted there), the u-velocity field can be calculated using the first Euler equation.

$$(1) \qquad -i\omega u + \bar{U}_o \frac{\partial u}{\partial x} + \frac{1}{\rho} \frac{\partial p}{\partial x} = o,$$

This is, with p known, a nonhomogeneous differential equation for u which can be solved in closed form and leads to a solution containing error functions of complex argument. This can be expanded for large x to provide a simple far field solution. We can produce, however, the same far field solution in a much simpler way. It is a reasonable assumption, that the gradients of the fluctuating $\tilde{u}$-flow become smaller with increasing distance from the plate edge. If, e.g., u is $\propto 1/\sqrt{-x}$, $\partial u/\partial x$ will become $\propto 1/(-x^{3/2})$ which means that $\partial u/\partial x$ will decrease more rapidly with increasing (negative) x. Consequently, for large negative x the fluctuating flow will behave as if no mean flow were there. After neglecting the second term in eq. (1) we obtain a simple solution, i.e., the parabolic flow created in a fluid at rest by the pressure distribution, eq. (33). We end up with

$$(89) \qquad |\tilde{u}_2| = \frac{1}{4\cdot\sqrt[4]{\tilde{x}^2+\tilde{y}^2}} \cdot \cos\left(\frac{1}{2} \arctan \left|\frac{\tilde{y}}{\tilde{x}}\right|\right).$$

$$(\tilde{x} < -1)$$

This asymptotic equation is also plotted (dotted lines) in the lower half of Fig. 10. It works quite well for $\tilde{x}$ smaller than -1.

We are left with a situation which can be considered to be ideal in computational fluid mechanics: The region where information relies on pure computation is limited and is imbedded into asymptotic solutions. How well the computation works is also shown by a comparison between numerically calculated values of $\tilde{u}_2$ at $\tilde{y} = o$ and analytic values from eq. (69).

In Table 1 these two sets of data are compared. The deviations are minimal in spite of the fact that our integration stepwidth is relatively coarse with $\Delta\tilde{\xi} = o.1$.

The most interesting regime of the $|u_2|$-curves is found near $\tilde{x} = o$ and for small $\tilde{y}$ (see Fig. 10). Indeed, as anticipated in section 2.2., the gradient of the computed curve becomes very steep there. If one extrapolated $|u_2|$ at $x = o$ and $y = o$ from data taken at $y \neq o$ one would underestimate the actual value there.

4. The relative importance of the edge region

In the preceding section, it had been mentioned, that under almost all conceivable circumstances, a parabolic pressure field is created close to the plate edge. The relevance of this region to the shear layer excitation will be shown with a simple model (see Fig. 11)

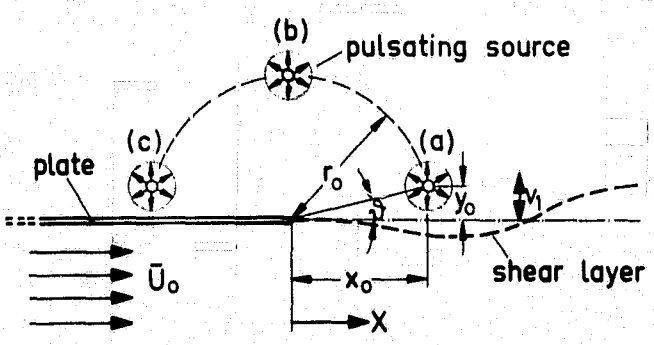

Fig. 11 Shear layer excitation by a monopole source.

$\tilde{x}$		0	0.125	0.25	0.5	0.75	1	1.5	2	2.5	3	4	5	10
$\tilde{u}_{2r}$	numerical	-0.486	-0.394	-0.301	-0.077	0.202	0.553	1.520	2.788	3.931	3.829	-9.134	-55.00	-1489.7
	analytical	-0.487	-0.397	-0.300	-0.076	0.203	0.554	1.520	2.788	3.931	3.829	-9.134	-55.00	-1489.7
$\tilde{u}_{2I}$	numerical	-0.489	-0.570	-0.647	-0.787	-0.899	-0.967	-0.825	0.066	2.313	6.446	18.184	5.80	8071.0
	analytical	-0.487	-0.570	-0.648	-0.787	-0.899	-0.967	-0.825	0.066	2.313	6.446	18.184	5.80	8071.0
$\lvert\tilde{u}_2\rvert$	numerical	0.689	0.693	0.714	0.790	0.921	1.114	1.729	2.789	4.561	7.497	20.349	55.30	8207.3
	analytical	0.688	0.695	0.714	0.790	0.922	1.114	1.730	2.789	4.561	7.497	20.349	55.30	8207.3
phase of $\tilde{u}_2$	numerical	-134.8°	-124.6°	-115.0°	-95.6°	-77.3°	-60.2°	-28.5°	1.4°	30.5°	59.3°	116.7°	174.0°	100.5°
	analytical	-135°	-124.9°	-114.9°	-95.5°	-77.3°	-60.2°	-28.5°	1.4°	30.5°	59.3°	116.7°	174.0°	100.5°

Table 1 Comparison of numerical and analytical data for u_2 at y = -o.

It will be shown, what the shear layer velocity v_1 is far downstream of the edge, if a pulsating (two-dimensional) monopole source is located at different positions (a) close to the shear layer, (b) above the edge or (c) upstream of the edge (see Fig.11). For the following calculation we will only consider the amplified instability wave constituent and not the decaying one, because this is irrelevant at great distances $x \gg \bar{U}_o/\omega$. We have from eq. (23)

$$(90) \qquad v_1 = -\frac{\omega}{\bar{U}_o} e^{\lambda_1 x} \int_o^\infty e^{-\lambda_1 x} v_{1f} dx \qquad x \gg \bar{U}_o/\omega$$

with $\lambda_1 = \frac{\omega}{\bar{U}_o}(i+1)$.

If the upper boundary of the integral in eq. (23) is set equal to infinity, like in eq. (90), the total influence of the excitation is included. This expansion will provide the magnitude of the instability wave downstream of the interaction region with the monopole field. In section 2, we had already given the induced field of a monopole field near a semi-infinite plate. We have for v_{1f} (see also [12]):

$$(26) \qquad v_{1f} = -\frac{Q}{4\pi}\sqrt{2(r_o - x_o)} \cdot \frac{1}{\sqrt{x}} \cdot \frac{x+r_o}{(x-x_o)^2+y_o^2}$$

with $r_o^2 = x_o^2 + y_o^2$ and Q being the source strength $Q = Q_o e^{-i\omega t}$. The last term of eq. (26) can be split into two parts

$$(91) \qquad \frac{x+r_o}{(x-x_o)^2-y_o^2} = \frac{1}{2}\left[\frac{\bar{T}}{x-z_o} + \frac{T}{x-\bar{z}_o}\right]$$

with

$$(92) \qquad z_o = x_o+iy_o;\ \bar{z}_o = x_o-iy_o;\ T = 1+\frac{i(r_o+x_o)}{y_o};\ \bar{T} = 1-\frac{i(r_o+x_o)}{y_o}$$

we are left with integrals of the type

$$(93) \qquad \int_0^\infty \frac{e^{-\lambda_1 x} dx}{\sqrt{x}(x+\tau)} = \frac{\pi}{\sqrt{\tau}} e^{\tau\lambda_1} \cdot \operatorname{erfc} \sqrt{\tau\lambda_1} .$$

The solution of the integral in eq. (93) can be found in tables for Laplace transforms or in the Handbook of Mathematical Functions [31, p. 302] by Abramovitz and Stegun. We end up with the following analytic solution *)

$$(94) \qquad \boxed{v_1 = + \frac{Q\omega\sqrt{2(r_o - x_o)}}{8\bar{U}_o} e^{\lambda_1 x} \left[\frac{\bar{T}}{\sqrt{-z_o}} e^{-z_o\lambda_1} \operatorname{erfc} \sqrt{-z_o\lambda_1} + \right.}$$

$$\boxed{\left. + \frac{T}{\sqrt{-\bar{z}_o}} e^{-\bar{z}_o\lambda_1} \operatorname{erfc} \sqrt{-\bar{z}_o\lambda_1} \right]}$$

The solution contains x only in the instability wave term $e^{\lambda_1 x}$, but the coefficient governing the magnitude of these waves is fairly complex. We will, therefore, expand the solution for two typical cases, i.e., an excitation by a monopole source further away from the lip ($\frac{r_o\omega}{D} \gg 1$) and an excitation directly at the lip of the semi-infinite plate.

For the excitation at large distances, we have to expand the complex error functions for large arguments. For an arbitrary complex argument z we have for large z [31]

$$(95) \qquad e^{z^2} \operatorname{erfc} z = \frac{1}{\sqrt{\pi} z} \left[1 + \sum_{m=1}^{\infty} (-1)^m \frac{1 \cdot 3 \ldots (2m-1)}{(2z^2)^m} \right].$$

If we take only the first term of the series expansion eq. (95)

*) This solution differs by the coefficient 1/2 from the solution given in [12], where this coefficient had been omitted erroneously.

we find after some intermediate calculations

$$(96) \qquad v_1 = \frac{Q\omega}{4\bar{U}_o} \cdot \frac{\sqrt{2(r_o - x_o)}}{r_o\sqrt{\pi\lambda_1}} \left[1 - \frac{1}{2\lambda_1 r_o}\left(1 - 2\frac{x_o^2}{r_o^2} - 2\frac{x_o}{r_o}\right)\right].$$

This equation can be expressed also in terms of the distance r_o between source and plate edge and in terms of the angle ϑ (see Fig. 11). We find

$$(97) \qquad v_1 = \frac{Q}{2\pi\sqrt{r_o}} \sin\frac{\vartheta}{2} \cdot \frac{\omega}{\bar{U}_o} \cdot \sqrt{\frac{\pi}{\lambda_1}}\, e^{\lambda_1 x}\left[1 + \frac{1}{\lambda_1 r_o}\left(\frac{1}{2}\cos 2\vartheta + \cos\vartheta\right)\right].$$

If we are interested in the modulus of v_1 only, we have

$$(98) \qquad |v_1| = \frac{Q}{2\pi\sqrt{r_o}} \sin\frac{\vartheta}{2} \cdot \sqrt{\frac{\omega}{\bar{U}_o}} \cdot \frac{\sqrt{\pi}}{\sqrt[4]{2}}\, e^{\frac{\omega x}{\bar{U}_o}} \left[1 + \frac{\bar{U}_o}{2\omega r_o}\left(\cos\vartheta + \frac{1}{2}\cos 2\vartheta\right)\right]$$

$$\text{for } \frac{\omega r_o}{\bar{U}_o} \gg 1 \text{ and } x \gg r_o.$$

The first part of this equation resembles very much the excitation velocity in the neighbourhood of the plate edge

$$(99) \qquad v_{1f} = -\frac{Q}{2\pi\sqrt{r_o}} \sin\frac{\vartheta}{2} \cdot \frac{1}{\sqrt{x}}$$

$$x \ll r_o.$$

One would obtain the following expression

$$(100) \qquad |v_1| = \frac{Q}{2\pi\sqrt{r_o}} \sin\frac{\vartheta}{2} \sqrt{\frac{\omega}{\bar{U}_o}} \cdot \frac{\sqrt{\pi}}{\sqrt[4]{2}}\, e^{\frac{\omega x}{\bar{U}_o}}$$

$$\text{for } \left(\frac{\omega x}{\bar{U}_o} \gg 1\right)$$

if one calculated the excitation by the parabolic field at the plate edge (eq. (99)) alone. Therefore, the expression in brackets reflects the additional interaction with the source field further downstream of the plate edge. The deviations from the pure interaction at the plate edge become small if $\omega r_o/\bar{U}_o > 1$.

The conclusion from this is, that the parabolic field at the plate edge dominates if the source is further away from the edge. Now consider the situation shown in Fig. 11. In which location (a), (b) or (c) of the source the interaction will it be the strongest? Equation (98) will give a clear answer: at (c), upstream of the shear layer!

In that context an interesting question is, how far an "exteriour excitation" can come from the turbulent shear layer downstream of the plate edge in a real flow situation. In our model, the pressure sources of the shear layer motion lie in the $y = o$ plane. Therefore, in this model, no feedback from the downstream perturbations is possible ($\sin \frac{\vartheta}{2} = o$). However, in a real situation $\nabla^2 p = o$ is still valid outside the shear layer. The pressure sources are in a region of small ϑ. Therefore a very weak feedback of the downstream turbulent flow is possible. This consideration is not that naïve as it seems at the first glance, because the equation $\nabla^2 p = -2\rho \frac{\partial U}{\partial y} \cdot \frac{\partial v}{\partial x}$ is also valid in three dimensions. The source term on the right hand side might look slightly different in a nonlinear flow situation, but the concept of having linearly superposable pressure sources in the shear layer will not break down, because the pressure is a linear quantity in all our equations, and deviations of this linearity will occur only if the pressure perturbation is of the same order as the ambient gas pressure. Anyway, eq. (98) shows clearly, why shear layers are highly sensitive to perturbations (such as sound) coming from upstream and not very sensitive to perturbations having their origin downstream of the edge in the shear layer.

Those who know recent experiments on excited jets know that an excitation close to the lip is very efficient. The preceding calculations did not consider this case, because it was assumed, that $\omega r_o/\bar{U}_o \gg 1$. Clearly, this assumption does not include the excitation directly at the plate edge. On the other hand, equation (94) can be also expanded for $\omega r_o/\bar{U}_o \ll 1$, which would include the lip excitation case. To do this, we use the following expansion of erfc z for small arguments of z (see [31]):

$$\text{(101)} \qquad \operatorname{erfc} z = 1 - \frac{2}{\sqrt{\pi}} e^{-z^2} \sum_{n=0}^{\infty} \frac{2n\, z^{2n+1}}{1 \cdot 3 \ldots (2n+1)} \,.$$

For small z, as in our case, we use only the first term of this expansion. It is no difficult problem, to extend the expansion further, but it will not provide much more insight. During the calculation it is also useful, to replace x_o by $-x_o$ to avoid ambiguity problems with complex roots. At the end, x_o is used in the previous sense again. After some intermediate calculations we find

$$\text{(102)} \qquad \boxed{v_1 = \frac{Q\omega}{2\bar{U}_o} e^{\lambda_1 x} \left[e^{-x_o \lambda_1} \cos(y_o \lambda_1) - 2\sqrt{\frac{r_o \lambda_1}{\pi}} \sin\frac{\vartheta}{2} \right]}$$

with $\lambda_1 = \frac{\omega}{\bar{U}_o}(i+1)$ and valid for $^{\omega r_o}/\bar{U}_o \ll 1$ and $^{\omega x}/\bar{U}_o \gg 1$.

For very small $r_o \omega/\bar{U}_o \to o$ we find a very simple result

$$\text{(103)} \qquad \boxed{v_1 = \frac{Q\,\omega}{2\bar{U}_o} e^{\lambda_1 x}}$$

This shows, that the source assumes its highest efficiency, if it is close to the lip, just above the shear layer. If we compare equations (100) and (103) in their relative efficiency, we find a coefficient n

$$\text{(104)} \qquad n = \frac{\sin\frac{\vartheta}{2}}{\sqrt{\pi} \cdot \sqrt[4]{2}} \cdot \sqrt{\frac{\bar{U}_o}{\omega r_o}} \,.$$

This shows, however, that the excitation via the interaction from upstream ($\sin\frac{\vartheta}{2} = 1$) and at a distance not too far away is not much worse than the excitation just at the lip.

There is some interesting physics hidden in eq. (102). Assume

$|y_o\lambda_1| \to +o$ and $\sqrt{r_o\lambda_1}\sin\frac{\vartheta}{2} \to o$. Then we have a source just above the shear layer at small, say, positive x_o. The source acts then as a δ-function with the strength Q/2 on the shear layer. Q/2 is just the flux which penetrates through the shear layer plane. With this in mind we reconsider the general solution for the shear layer motion, eq. (23) *)

$$(23) \qquad v_1 = -\frac{\omega}{\bar{U}_o} e^{\lambda_1 x} \int_o^x e^{-\lambda_1 x} v_{1f} dx + \frac{\omega}{\bar{U}_o} e^{\lambda_2 x} \int_o^x e^{-\lambda_2 x} v_{1f} dx ,$$

For v_{1f} we have here

$$(105) \qquad v_{1f} = -\frac{Q}{2}\delta(x-x_o) \qquad \text{at } y = +o$$

with eq. (23) we have the complete solution at once

$$(106) \qquad \boxed{v_1 = \frac{Q\omega}{2\bar{U}_o}\left[e^{\lambda_1 x}\cdot e^{-\lambda_1 x_o} - e^{\lambda_2 x}\cdot e^{-\lambda_2 x_o}\right]}$$

If both influences, the "local" δ-function influence and another term of the parabolic type are in competition, one sees, that the "local" influence can become weak in comparison to the parabolic type influence. In particular, if the source is further away from the plate edge, the parabolic influence at the edge has piled up to such high magnitudes by the exponential amplification so that a local influence (see position (a) in Fig. 11) would only contribute a term of the order

$$(107) \qquad v_{1\ \text{local}} = \frac{Q\omega}{2\bar{U}_o} e^{\lambda_1(x-x_o)} .$$

For the pure "local" excitation with $|\lambda_1 x_o| \to o$ we have, on the other hand, a simple analytic solution which might be utilized if the free shear layer is really excited just at the plate edge

*) with $G_1 = G_2 = o$

$$v_1 = \frac{Q\omega}{2\bar{U}_o}\left(e^{\lambda_1 x} - e^{\lambda_2 x}\right) \tag{108}$$

Also the u-distribution in the whole ambient field can be written in closed form. It contains exponential integrals of complex argument for the induced field of the instability waves truncated at $x = o$ ($v_1 = o$ for $x < o$) and of the induced field of the source. The details can be seen in appendix C*) where just this calculation is given in another context. For distances further downstream, we have a ultra-simple equation for the magnitude of the instability waves, where $|v_1| = |v_2| = |u_1| = |u_2|$. We find

$$|u_2| = \frac{Q\omega}{2\bar{U}_o} e^{\frac{\omega x}{\bar{U}_o}} \qquad \text{at } y = -o \tag{109}$$

with the usual decay in $\pm y$ direction

$$|u_{1,2}| = \frac{Q\omega}{2\bar{U}_o} e^{\frac{\omega(x-|y|)}{\bar{U}_o}} \qquad \begin{matrix} x > u_o/\omega \\ y \neq o \end{matrix} \tag{110}$$

Q is the volume flux (say, in m^2/s) of the excitation source. In a real situation with an arrangement like the one shown below (see Fig. 12) we suspect, that more than half of the volume flux Q penetrates through the $y = o$ plane. Therefore, the efficiency might be even slightly higher than suggested by eq. (110).

*) For numerical computations in the potential field outside the shear layer, it is also recommended, to use the calculations in [36].

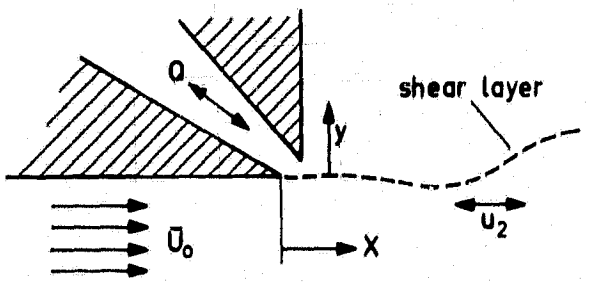

Fig. 12 real edge excitation configuration.

5. Two streams with different densities

As we will see, there is no simple transformation to convert the results of the case with a single stream ($\bar{U}_1 = o$ for $y > o$; $\bar{U}_2 = \bar{U}_o$ for $y < o$; $\rho_1 = \rho_2$) to the case with two streams ($\bar{U}_1 \neq o$; $\bar{U}_2 \neq o$; $\rho_1 \neq \rho_2$). Nevertheless, it will turn out that the results of this section will be still very similar to those of section 2. However, the mathematics is much more tedious. Since it would not provide any specific insight to show all details of the calculations, we will provide here only the basic ideas and steps.

We start, as in section 2, with the condition of equal displacement h at both sides of the shear layer

$$(111) \quad \left\{ \begin{array}{l} v_1 = \frac{\partial h}{\partial t} + \bar{U}_1 \frac{\partial h}{\partial x} \\ \\ v_2 = \frac{\partial h}{\partial t} + \bar{U}_2 \frac{\partial h}{\partial x} \end{array} \right\} .$$

By using $h \propto e^{-i\omega t}$ and by eliminating h from equation (111) we

obtain one condition relating v_1 and v_2

$$(112) \qquad \boxed{v_1 + i\,\frac{\bar{U}_2}{\omega}\,\frac{\partial v_1}{\partial x} = v_2 + i\,\frac{\bar{U}_1}{\omega}\,\frac{\partial v_2}{\partial x}}\,.$$

This equation holds for all x and is also valid for $\rho_1 \neq \rho_2$, since it is a merely kinematic condition. To create a second condition for v_1 and v_2 we rely again on a consideration of the pressure field. Since the density jump is assumed to occur in the shear layer as well as the mean velocity jump, we obtain again $\nabla^2 p = 0$ outside the shear layer and with exception of the location of the exteriour source. Therefore, we can again use the second Euler equation (2)

$$(113) \qquad \left\{ \begin{array}{l} \rho_1 \left(-i\omega v_1 + \bar{U}_1 \dfrac{\partial v_1}{\partial x}\right) = -\dfrac{\partial p_1}{\partial y} \\[2ex] \rho_2 \left(-i\omega v_2 + \bar{U}_2 \dfrac{\partial v_2}{\partial x}\right) = -\dfrac{\partial p_2}{\partial y} \end{array} \right\}.$$

The procedure to split the pressure field into two constituents, the forcing terms (index "f") and the shear layer terms (index "s") is still possible. The "f" pressure gradient is continuous through the shear layer and the "s" pressure gradient is symmetric with respect to the shear layer. We have

$$(114) \qquad \left\{ \begin{array}{l} \rho_1 \left(-i\omega v_{1f} + \bar{U}_1 \dfrac{\partial v_{1f}}{\partial x}\right) = \rho_2 \left(-i\omega v_{2f} + \bar{U}_2 \dfrac{\partial v_{2f}}{\partial x}\right) \\[2ex] \rho_1 \left(-i\omega v_{1s} + \bar{U}_1 \dfrac{\partial v_{1s}}{\partial x}\right) = -\rho_2 \left(-i\omega v_{2s} + \bar{U}_2 \dfrac{\partial v_{2s}}{\partial x}\right) \end{array} \right\}$$

where $v_1 = v_{1f} + v_{1s}$; $v_2 = v_{2f} + v_{2s}$. Equation (93) can be condensed into

$$(115) \qquad \frac{\rho 1}{\rho_2}\left(v_1 + i\,\frac{\bar{U}_1}{\omega}\,\frac{\partial v_1}{\partial x}\right) + v_2 + i\,\frac{\bar{U}_2}{\omega}\,\frac{\partial v_2}{\partial x} = 2\left(v_{2f} + i\,\frac{\bar{U}_2}{\omega}\,\frac{\partial v_{2f}}{\partial x}\right),$$

Since it is more convenient to calculate the forcing pressure field (which is still parabolic around the semi-infinite plate), we prefer to express the right hand side of eq. (115) in terms of the pressure field. We have from the second Euler equation

$$(116) \qquad v_{2f} + i\,\frac{\bar{U}_2}{\omega}\,\frac{\partial v_{2f}}{\partial x} = -\,\frac{i}{\rho_2 \omega}\,\frac{\partial p_{2f}}{\partial y}$$

where the pressure gradient in y-direction is taken at y = o. We will abbreviate in the following calculations

$$(117) \qquad \dot{p} = -\,\frac{2i}{\rho_2 \omega}\,\frac{\partial p_{2f}}{\partial y} \;;\; \sigma = \frac{\bar{U}_1}{\bar{U}_2} \;;\; \beta = \frac{\rho_1}{\rho_2} \,.$$

Consequently, we can grite eq. (94)

$$(118) \qquad \boxed{\beta\left(v_1 + i\,\frac{\bar{U}_1}{\omega}\,\frac{\partial v_1}{\partial x}\right) + v_2 + i\,\frac{\bar{U}_2}{\omega}\,\frac{\partial v_2}{\partial x} = \dot{p}}$$

with the right hand side being known and proportional to $1/\sqrt{x}$. Equations (118) and (112) can be used to provide a single non-homogeneous differential equation for v_1

$$(119) \qquad \boxed{(1+\beta)\,v_1 + \frac{2i\bar{U}_2}{\omega}\,(1+\sigma\beta)\frac{dv_1}{dx} - \frac{\bar{U}_2^2}{\omega^2}(1+\sigma^2\beta)\frac{d^2 v_1}{dx^2} = \dot{p} + \frac{i\sigma\bar{U}_2}{\omega}\,\frac{d\dot{p}}{dx}} \,.$$

The homogeneous solutions (Helmholtz solutions) are

$$(120) \qquad \varphi_1 = C_2 e^{\lambda_1 x} \;;\; \varphi_2 = C_2 e^{\lambda_2 x}$$

with

$$(121) \qquad \lambda_{1,2} = \frac{\omega}{\bar{U}_2} \cdot \frac{1}{1+\sigma^2\beta}\left[i(1+\sigma\beta) \pm (1-\sigma)\sqrt{\beta}\right] \,.$$

The complete solution is

$$(122)\qquad v_1 = +\frac{\bar{U}_2}{2\omega}\cdot\frac{(1+\sigma^2\beta)}{\sqrt{\beta}(1-\sigma)}\cdot\left[e^{\lambda_1 x}\int_{G_1}^{x} e^{-\lambda_1 x}\,RS\,dx - e^{\lambda_2 x}\int_{G_2}^{x} e^{-\lambda_2 x}\,RS\,dx\right]$$

where "RS" stands for the right hand side of eq. (119). With the same arguments as those given in appendix 2 for $\sigma = 0$ and $\beta = 1$ we can set $G_1 = G_2 = 0$. We can further evaluate eq. (122)

$$(123)\qquad v_1 = -\frac{\omega}{2\bar{U}_2\sqrt{\beta}}\cdot\frac{1}{1+\sigma^2\beta}\left[(1+i\sigma\sqrt{\beta})e^{\lambda_1 x}\int_{0}^{x} e^{-\lambda_1 x}\hat{p}\,dx - (1-i\sigma\sqrt{\beta})e^{\lambda_2 x}\int_{0}^{x} e^{-\lambda_2 x}\hat{p}\,dx\right].$$

For a parabolic pressure field around the semi-infinite plate we have from eq. (33) in section 2.1.

$$(124)\qquad \hat{p} = -\frac{2i}{\rho_2\omega}\cdot\frac{\partial p_{2f}}{\partial y} = -\frac{2i}{\omega\rho_2}\cdot\frac{\Delta p_{12}}{4\sqrt{lx}}\,.$$

Consequently, we can again relate all quantities in our flow field to the excitation, characterized by the pressure difference Δp_{12} at both sides of the plate at the distance l from the plate edge. Therefore, we can introduce dimensionless quantities similar to those used in section 2:

$$(125)\qquad \left\{\begin{array}{l} \tilde{v}_1 = \dfrac{v_1\cdot\rho_2\sqrt{\omega\bar{U}_2 l}}{\Delta p_{12}}\;;\quad \tilde{v}_2 = \dfrac{v_2\cdot\rho_2\sqrt{\omega\bar{U}_2 l}}{\Delta p_{12}} \\[2ex] \tilde{\lambda}_{1,2} = \dfrac{1}{1+\sigma^2\beta}\left[i(1+\sigma\beta) \pm (1-\sigma)\sqrt{\beta}\right] \\[2ex] \tilde{x} = \dfrac{\omega x}{\bar{U}_2}\;;\quad \sigma = \dfrac{\bar{U}_1}{\bar{U}_2}\;,\ \beta = \dfrac{\rho_1}{\rho_2} \end{array}\right\}.$$

In the expression for $\tilde{\lambda}$ the positive sign in the brackets corresponds to $\tilde{\lambda}_1$, the negative sign to $\tilde{\lambda}_2$, respectively. With these abbreviations we obtain the final result for $\tilde{v}_1$, after

integration of eq. (12)

$$(126)\qquad \bar{v}_1 = \frac{i\sqrt{\pi}}{4\sqrt{\pi}(1+\alpha^2\beta)}\left[\frac{1+i\alpha\sqrt{\pi}\beta}{\sqrt{\lambda_1}}\, e^{\lambda_1 x}\operatorname{erf}\sqrt{\lambda_1 x} - \frac{1-i\alpha\sqrt{\pi}\beta}{\sqrt{\lambda_2}}\, e^{\lambda_2 x}\operatorname{erf}\sqrt{\lambda_2 x}\right]$$

$(x > 0,\ y = +0)$

To obtain $\bar{v}_2$ we can either derive a similar equation as eq. (119) from the same initial equations (112) and (118) or utilize eqs. (112) and (118) together with eq. (124) to obtain v_2 from $\bar{v}_1$. We end up with

$$(127)\qquad \bar{v}_2 = -\frac{i\sqrt{\pi}}{4(1+\alpha^2\beta)}\left[\frac{1+i\alpha\sqrt{\pi}\beta}{\sqrt{\lambda_1}}\, e^{\lambda_1 x}\operatorname{erf}\sqrt{\lambda_1 x} + \frac{1-i\alpha\sqrt{\pi}\beta}{\sqrt{\lambda_2}}\, e^{\lambda_2 x}\operatorname{erf}\sqrt{\lambda_2 x}\right]$$

$(x > 0,\ y = -0)$

Besides the differences between $\bar{v}_1$ and $\bar{v}_2$ which resemble those in section 2, we have a different coefficient ($\sqrt{\pi}\beta$) in the denominator in front of the brackets. This leads to different velocities of the instability waves on both sides of the shear layer. Nevertheless, the displacement h at both sides of the shear layer is the same, as postulated in the beginning.

Before we determine the corresponding u-distributions we will discuss the behaviour of $\bar{v}_1$ and $\bar{v}_2$ for small and large $\bar{x}$. For small x the expansion of eq. (126) and (127) yield

$$(128)\qquad \bar{v}_1 = -\frac{\sqrt{\bar{x}}}{1+\alpha^2\beta}\,, \qquad \bar{v}_2 = -\frac{\sqrt{\bar{x}}}{1+\alpha^2\beta}$$

$(x > 0)$

In both cases the envelope of the displacement h is $h \sim \bar{x}^{1.5}$, consequently the mean flow leaves the trailing edge of the plate tangentially, which is equivalent to the Kutta condition. For $\bar{U}_1 > 0$ and $\alpha > 0$ higher order terms in the expansion for $\bar{v}_1$,

take over, so that h is still $h \sim \tilde{x}^{1.5}$.

For large $\tilde{x}$ we obtain for $\tilde{v}_1$ and $\tilde{v}_2$

$$(129)\qquad \tilde{v}_1 = \frac{i\sqrt{\pi}\sigma e^{\tilde{\lambda}_1\tilde{x}}}{4\sqrt{\beta}(1-i\sigma\sqrt{\beta})\sqrt{\tilde{\lambda}_1}} - \frac{1}{4\sqrt{\tilde{x}}} \cdot \frac{2}{1+\beta}$$

$(\tilde{x} \to \infty)$

$$(130)\qquad \tilde{v}_2 = -\frac{\sqrt{\pi}\sigma e^{\tilde{\lambda}_1\tilde{x}}}{4(1-i\sigma\sqrt{\beta})\sqrt{\tilde{\lambda}_1}} - \frac{1}{4\sqrt{\tilde{x}}} \cdot \frac{2}{1+\beta}$$

$(\tilde{x} \to \infty)$.

We again have a Helmholtz-type solution (first terms of eqs. (129) and (130)) in the far field and another contribution due to the excitation being proportional to $1/\sqrt{x}$. The interesting thing is, that nature takes here an <u>average value of the densities</u> represented by the coefficient $2/1+\beta$. However, the Helmholtz-type solutions are different in their magnitude by the coefficient $\sqrt{\beta}=\sqrt{\rho_1/\rho_2}$ in the different flow regimes.
The u-velocities are calculated in exactly the same way as the v-velocities above, with an approach identical to that used in section 1. We end up with

$$(131)\qquad \tilde{u}_1 = + \frac{\sqrt{\pi}}{4\sqrt{\beta}(1+\sigma^2\beta)} \left[\frac{1+i\sigma\sqrt{\beta}}{\sqrt{\tilde{\lambda}_1}} e^{\tilde{\lambda}_1\tilde{x}} - \frac{1-i\sigma\sqrt{\beta}}{\sqrt{\tilde{\lambda}_2}} e^{\tilde{\lambda}_2\tilde{x}}\right]$$

$(x > o;\ y = +o)$

$$(132)\qquad \tilde{u}_2 = - \frac{i\sqrt{\pi}}{4(1+\sigma^2\beta)} \left[\frac{1+i\sigma\sqrt{\beta}}{\sqrt{\tilde{\lambda}_1}} e^{\tilde{\lambda}_1\tilde{x}} + \frac{1-i\sigma\sqrt{\beta}}{\sqrt{\tilde{\lambda}_2}} e^{\tilde{\lambda}_2\tilde{x}}\right]$$

$(x > o;\ y = -o)$

$$(133)\qquad \tilde{u}_1 = \frac{\sqrt{\pi}}{4\sqrt{\beta}(1+\sigma^2\beta)} \left[\frac{1+i\sigma\sqrt{\beta}}{\sqrt{\tilde{\lambda}_1}} e^{\tilde{\lambda}_1\tilde{x}} \operatorname{erfc}\sqrt{\tilde{\lambda}_1\tilde{x}} - \frac{1-i\sigma\sqrt{\beta}}{\sqrt{\tilde{\lambda}_2}} e^{\tilde{\lambda}_2\tilde{x}} \operatorname{erfc}\sqrt{\tilde{\lambda}_2\tilde{x}}\right]$$

$(x < o;\ y = +o)$

$$(134)\qquad \tilde{u}_2 = - \frac{i\sqrt{\pi}}{4(1+\sigma^2\beta)} \left[\frac{1+i\sigma\sqrt{\beta}}{\sqrt{\tilde{\lambda}_1}} e^{\tilde{\lambda}_1\tilde{x}} \operatorname{erfc}\sqrt{\tilde{\lambda}_1\tilde{x}} + \frac{1-i\sigma\sqrt{\beta}}{\sqrt{\tilde{\lambda}_2}} e^{\tilde{\lambda}_2\tilde{x}} \operatorname{erfc}\sqrt{\tilde{\lambda}_2\tilde{x}}\right]$$

$(x < o;\ y = -o)$

with $\tilde{u}$ in dimensionless form like $\tilde{v}$.

For large $\tilde{x}$ only the amplified Helmholtz-solutions survive (terms with λ_1 in eqs (131) and (132)).The modulus of these amplified waves is for $x \gg 1$

(135) $$|\tilde{u}_1| = \frac{\sqrt{\pi} e^{\sqrt{\beta}(1-\sigma)\tilde{x}}}{4\sqrt{\beta} \cdot \sqrt[4]{(1+\beta)(1+\sigma^2\beta)}} \qquad \tilde{x} \gg 1$$

and

(136) $$|\tilde{u}_2| = \sqrt{\beta} \cdot |\tilde{u}_1| \qquad \tilde{x} \gg 1$$

If we return to dimensional quantities, we have for eq. (135)

(137) $$|u_1| = \frac{\Delta p_{12}}{\rho_2 \sqrt{\omega \bar{U}_2 1}} \cdot \frac{\sqrt{\pi}}{4} \cdot \frac{e^{\left(\sqrt{\frac{\rho_1}{\rho_2}}\left(1-\frac{\bar{U}_1}{\bar{U}_2}\right) \cdot \frac{\omega x}{\bar{U}_2}\right)}}{\sqrt{\frac{\rho_1}{\rho_2}} \cdot \sqrt[4]{(1+\rho_1/\rho_2)\left(1+\frac{\rho_1 \bar{U}_1^2}{\rho_2 \bar{U}_2^2}\right)}}$$

6. Theoretical considerations related to experiments

Parallel to this theoretical investigation also experiments were carried out. On these experiments we will report later. During the experiments a number of typical problems arose which can be settled theoretically rather than experimentally.

A point of particular interest is, that the phase speed of the instability waves in the experiments was lower than that of our theoretical model. Phase speed and wave number are inversely proportional to each other. Since the wave number is coupled to the exponential decay rate (of the fluctuations) perpendicular

to the shear layer, this has a significant influence on the induced field (see eq. (68) in section 2.2.). Conditions which can change the phase speed are:"overshoot" of the mean velocity profile (section 6.1.), finite shear layer thickness and entrainment effects (section 6.2.). Finally, we have to consider the effects of additional walls in a test facility. We will consider the case of a shear layer in the symmetry plane of a rectangular channel (section 6.3.).

6.1. "Overshoot" of the mean velocity profile

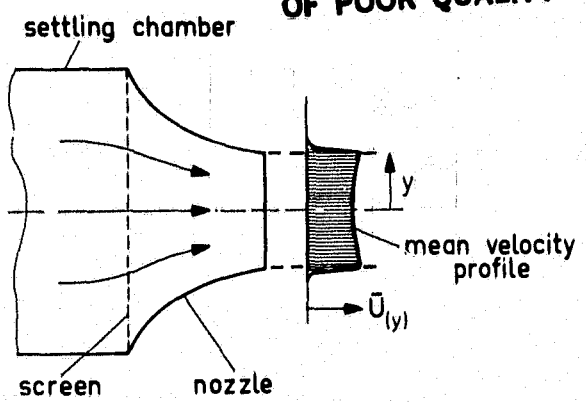

Fig. 13 Interaction between nozzle and screen.

In Fig. 13 it can be seen how an "overshoot" of the mean velocity profile can be (inadvertedly) generated. A flow penetrates through a screen of high resistance at (almost) constant speed. The following contraction in a nozzle leads to different acceleration of the different streamlines. In particular, the regions closer to the wall are accelerated more than the flow in the center of the nozzle. This creates the "overshoot" of the mean velocity profile. Since it occurs often in experiments it is worth investigating its influence with a simple theoretical

model. As we will see, the deviations due to this effect cannot be neglected.

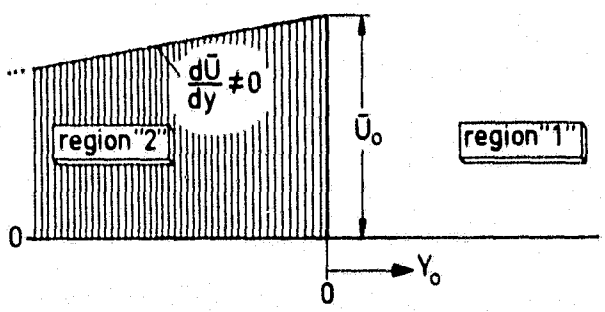

Fig. 14 Mean flow with gradient and shear layer.

The model which we are going to consider can be seen in Fig. 14. Since we cannot use our pressure gradient considerations as in the preceding section we will proceed with a slightly different approach. In addition, we will restrict ourselves to the discussion of conventional spatial instability waves extended from $x = -\infty$ to $x = +\infty$. The aim is to find how the wave number and the amplification rate will change if we introduce a mean flow gradient (see Fig. 14).

We start with the same basic equations as in section 2., i.e., the linearized Euler equations (1) and (2) and the continuity equation (3). If we subtract the x-derivative of (2) from the y-derivative of (1) we can eliminate the pressure and obtain

$$(138) \qquad -i\omega \left(\frac{\partial u}{\partial y} - \frac{\partial v}{\partial x}\right) + \bar{U}\frac{\partial}{\partial x}\left(\frac{\partial u}{\partial y} - \frac{\partial v}{\partial x}\right) + \nu\frac{\partial^2 \bar{U}}{\partial y^2} = 0$$

This is what remains from the inviscid vorticity transport equation if we consider a linearized fluid motion which is harmonic in time ($\propto e^{-i\omega t}$) and takes place in a parallel mean flow with velocity $\bar{U}_{(y)}$. If we assume a potential flow with $u = \partial\phi/\partial x$ and $v = \partial\phi/\partial y$ we have from eq. (138)

$$(139) \qquad \frac{\partial \phi}{\partial y} \cdot \frac{\partial^2 \bar{U}}{\partial y^2} = 0.$$

This means that we can use a potential flow approach in regions where $\partial^2\bar{U}/\partial y^2 = 0$. This condition is fulfilled outside the shear layer. At both sides of the shear layer we have to match the displacement h and the pressure p, as before. We use the following ansatz for the stability waves

$$(140) \quad \left\{ \begin{array}{l} \text{for } y > 0\text{: } \bar{U}_1 = 0 \; ; \quad \phi_1 = Ae^{i\alpha(x+iy)} \\ \\ \text{for } y < 0\text{: } \bar{U}_2 = \bar{U}_0 + \frac{d\bar{U}}{dy} \cdot y \; ; \; \phi_2 = Be^{i\alpha(x-iy)} \end{array} \right\} .$$

Since ϕ is a function of $x+iy$, the continuity equation written in terms of the potential, i.e., $\nabla^2\phi = 0$ is satisfied. The potentials fulfill also the boundary conditions at $y = \pm\infty$, because the induced velocities become zero there. α is the complex wave number defined as usual in stability theory. A and B are magnitudes of the potentials which are still arbitrary at this stage of the calculations.

The kinematic condition of equal displacement h at both sides of the shear layer is, as in section 2:

$$(141) \qquad v_2 = v_1 + i \frac{\bar{U}_0}{\omega} \frac{\partial v_1}{\partial x} \quad .$$

Using eq. (140) we obtain

$$(142) \qquad B = -A \left(1 - \frac{\alpha \bar{U}_0}{\omega}\right) .$$

The second condition is, that the pressures or the pressure gradients should be equal at both sides of the shear layer. For $y > 0$ we have from the first Euler equation (1):

$$(143) \qquad \frac{\partial p_1}{\partial x} = i\rho\omega u_1$$

and for y < o we obtain from the same equation (1)

$$(144) \qquad \frac{\partial p_2}{\partial x} = -\rho(-i\omega u_2 + \bar{U}_o \frac{\partial u_2}{\partial x} + \frac{d\bar{U}}{dy} \cdot v_2) \ .$$

If equations (143) and (144) are set equal and with eq. (140) we have

$$(145) \qquad A = B \ (1 - \frac{\bar{U}_o \alpha}{\omega} + \frac{1}{\omega} \cdot \frac{d\bar{U}}{dy}).$$

Equations (142) and (145) provide a quadratic equation for α with the solutions

$$(146) \qquad \alpha_{1,2} = \frac{\omega}{\bar{U}_o} \left[(1 + \frac{d\bar{U}/dy}{2\omega}) \pm i \sqrt{1 - (\frac{d\bar{U}/dy}{2\omega})^2} \right] .$$

If we compare this to our previous nomenclature, using $\lambda_{1,2} = i\alpha_{1,2}$ we find

$$(147) \qquad \lambda_{1,2} = \frac{\omega}{\bar{U}_o} \left[i \ (1 + \frac{d\bar{U}/dy}{2\omega}) \pm \sqrt{1 - (\frac{d\bar{U}/dy}{2\omega})^2} \right] .$$

In comparison to the situation, which we had before with $d\bar{U}/dy = o$, we have now an increased wave number (imaginary part of eq. (147)), which will cause a more rapid decay of the induced field in the y-direction. The deviations can be, for a typical situation in an experiment, in the order of 10-20 %. On the other hand, the influence on the amplification rate (real part of eq. (147)) is much weaker and will be in the order of typically 1-2%.

6.2. Entrainment and finite shear layer thickness effects

If one considers the effect of entrainment alone for an infinitesimally thin shear layer, one can extract the relevant informations from section 3, equation (121). For constant density, the wave number is

$$(148) \qquad \text{Im } (\lambda) = \frac{\omega}{\bar{U}_2} \cdot \frac{1 + \bar{U}_1/\bar{U}_2}{1 + (\bar{U}_1/\bar{U}_2)^2} \ .$$

For small $\sigma = \bar{U}_1/\bar{U}_2$, say $\sigma = 0.1$, we have a wave number increased by $\approx$ 9 %. This enhances also the exponential decay rate in the y-direction by 9 %.

As expected, the downstream growth rate decreases with increasing σ. We have for the growth rate

$$\text{(149)} \qquad \mathrm{Re}\,(\lambda) = \frac{\omega}{\bar{U}_2} \cdot \frac{1 - \bar{U}_1/\bar{U}_2}{1 + (\bar{U}_1/\bar{U}_2)^2} .$$

For, say, $\sigma = 0.1$ we have a growth rate decreased by $\approx$ 11 %. These considerations are valid for a "thin" shear layer.

We cannot really neglect, however, the effect of finite shear layer thickness. A typical parameter of the stability analysis of shear layers of finite thickness is the Strouhal number $S_\theta = \theta \cdot f/\bar{U}_2$ where f is the frequency and θ is the momentum thickness. The momentum thickness is defined as

$$\text{(150)} \qquad \theta = \int_{-\infty}^{+\infty} \frac{\bar{U}}{\bar{U}_2} \left(1 - \frac{\bar{U}}{\bar{U}_2}\right) dy .$$

For a typical shear layer profile, which might be approximated with good accuracy by a tanh-profile we have the situation displayed in Fig. 15

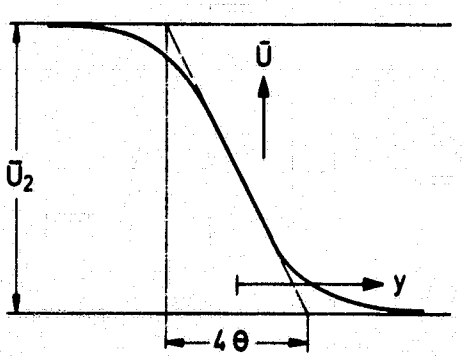

Fig. 15 Shear layer profile.

The amplification rate and the phase speed, according to Michalke [6] are given in Fig. 16

As we see from Fig. 16, the deviations in the wave number are much more significant for increasing S_θ (and thus deviating from the "thin" shear approach) than for the amplification rate. Therefore, the finite thickness causes an increasing wave number and enhances again the decay of the induced field in the y-direction. This influence can be quantified with the numerical data available in the literature [6, 37]. Also the combined influence of entrainment and finite shear layer can be extracted from [37], where calculations are given for a shear layer of finite thickness between two streams of different velocity $\bar{U}_1$ and $\bar{U}_2$.

6.3. Channel effects

In an experiment, one cannot offer a facility with infinitely extended streams at both sides of a shear layer. Therefore, we will have to consider effects due to the finite dimensions of the two streams. The experimental setup which can be modeled with the least complication is that of a free shear layer in the symmetry line of a two-dimensional channel. At the rigid walls the velocities and pressure gradients normal to the surface have to be zero. Thus, the boundary conditions at both sides of the shear layer are the same. Consequently, our basic approach which takes advantage of splitting the pressure field into a symmetric and an antisymmetric part, is still valid. This has been shown already in a different, more involved way in [12]. Therefore, the general solutions for the v-velocity component are still valid (eqs.(23) and (123)). However, we will have to discuss the deviations in the actual velocities and pressures which will occur in

(i) the excitation field (v-velocities)

(ii) the resulting shear layer motion (v-velocities)

(iii) the induced u-velocities

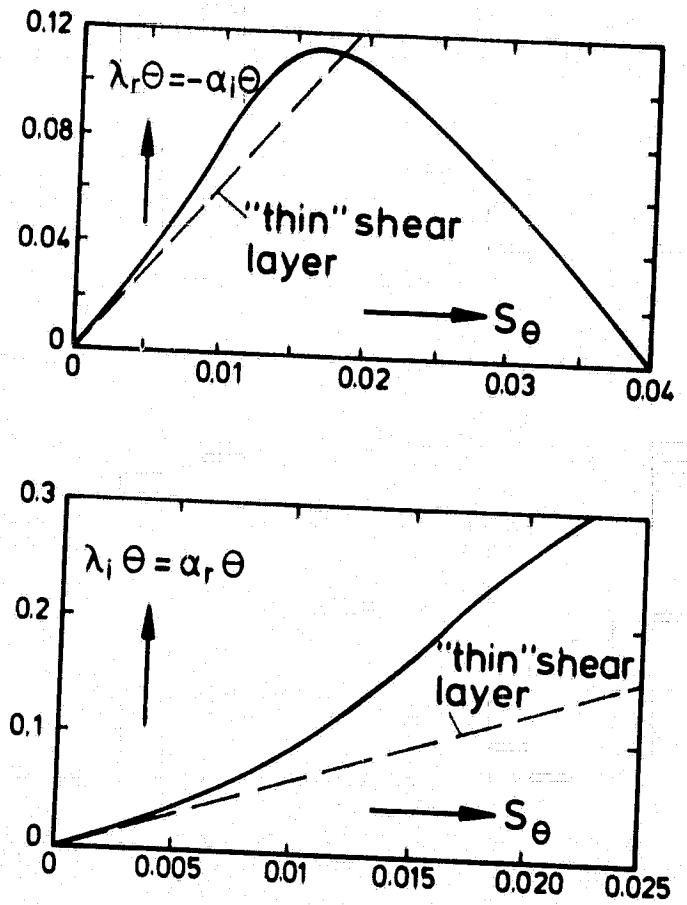

Fig. 16 Amplification rate ($\lambda_r\theta$) and wave number ($\lambda_i\theta$) of a shear layer with finite thickness, according to [6].

6.3.1 Effects on the excitation field

There is no doubt, that the structure of the excitation field will be still parabolic if we are close enough to the edge of the semi-infinite plate. Therefore, there will be particular conditions when the solutions calculated in the preceding section are still valid. The restrictions of these conditions will be discussed below. We will calculate the fluctuating flow (without shear layer and mean flow) in a simplified test section, which can be seen in Fig. 17, left hand side.

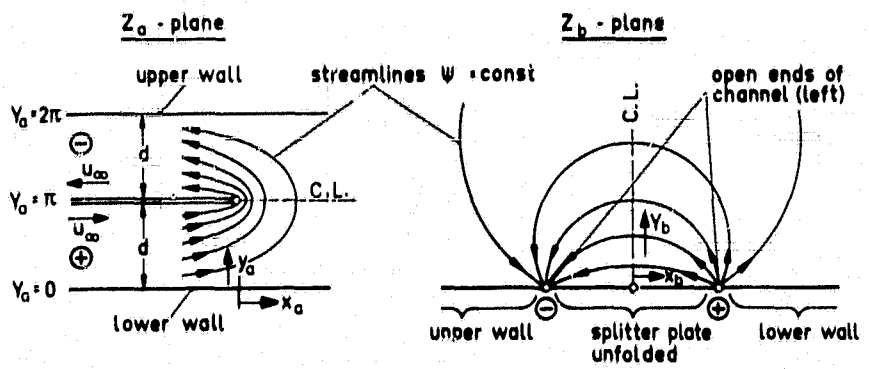

z_a-plane (physical) z_b-plane (image)

Fig. 17 Simplified test section and its conformal image.

The test section is simplified in so far as the nozzle and the settling chamber on the left hand side have not been considered. The excitation is assumed to be generated at great distance on the left hand side inside the bisected channel by two sources of opposite sign*). This would be a good model for the situation

*) A similar procedure as the one described here could be used if the source were in the lower and upper wall, created physically by vibrating plates.

with sound excitation by loudspeakers connected to two settling chambers upstream of the bisected channel.

If the sound wavelength is much greater (say, at least ten times) than a typical dimension of the problem, (e.g., the channel width), one can describe the alternating flow in the vicinity of the plate end by incompressible flow theory. In that case, we can use the very powerful tool of conformal mapping to solve the problem completely. For configurations like the one shown in Fig. 17, one can use the Schwartz-Christoffel-transformation to map the flow in the interiour of the channel into the flow in a half-plane (Fig. 17, right hand side). Our channel and splitter plate walls will be stretched into the straight line $y_b = o$ (see Fig. 17). The open ends at the left hand side of the bisected channel will be mapped into the two points at $x_b = +1$ and $x_b = -1$ on the x_b-axis. If we install a positive source at $x_b=1$ and a negative source at $x_b= -1$ we have already the image of the flow field in the z_b-plane.

The mapping function relating the z_a and z_b planes can be found in Kober's dictionary of conformal representations [38]. We have

$$z_b = \sqrt{1+e^{z_a}} \tag{151}$$

with $z_a = x_a + iy_a$ (physical plane) and $z_b = x_b + iy_b$ (image plane). This mapping function corresponds to the specific dimensions given in Fig. 17. We introduce the complex potential $\Phi = \phi + i\Psi$ where the potential function ϕ and the stream function ψ are defined as usual in plane flow problems. The complex potential of a source at the origin is $\Phi = \ln z$. Thus we have for the potential of the positive and negative source in the z_b-plane, located at $x_b = \pm 1$

$$\Phi = A \left[\ln (z_b-1) - \ln (z_b+1)\right] \tag{152}$$

where A is a constant (proportional to the strength of the sources). With the transformation equation (151) we have in the

z_a-plane

(153) $$\Phi = A \left[\ln \left(\sqrt{1+e^{z_a}} - 1 \right) - \ln \left(\sqrt{1+e^{z_a}} + 1 \right) \right] .$$

We are first interested in the v-velocity (in our previous nomenclature v_{1f}) at the center line of the channel. The complex velocity is

(154) $$\frac{d\Phi}{dz_a} = u - iv \quad .$$

Taking the derivative of eq. (153) we obtain

(155) $$u - iv = \frac{A}{\sqrt{1+e^{z_a}}} \quad .$$

The center line of the channel is located at $y_a = \pi$; there we have $z_a = x_a + i\pi$. With $e^{i\pi} = -1$ we obtain

(156) $$u - iv = \frac{A}{\sqrt{1-e^{x_a}}} \quad \text{at the center line (C.L.)} .$$

For $x_a < o$ this is purely real, which means that $v = o$ there. For $x_a \to -\infty$ we have $u_{C.L.} \to u_\infty$, the homogeneous velocity at large negative distances in the bisected channel. Therefore is $A = u_\infty$. Equation (156) becomes purely imaginary (and $u = o$ at the center line) for $x_a > o$.

Before we write down our equations in real physical quantities such as u_∞, we have to relate x also to the only real physical dimension of the problem, i.e., the channel half-width d (see Fig. 17). Therefore, we will replace x_a by a dimensionless quantity, i.e., $\frac{x \cdot \pi}{d}$. The coefficient π occurs, because in the initial coordinate system the channel width had this value. We end up with the following equations for the velocities at the center line $y = \pm o$:

	$x < o$	$x > o$
(157)	$v = o$	$v = \frac{u_\infty}{\sqrt{e^{\frac{x\pi}{d}} - 1}}$
(158)	$u = \mp \frac{u_\infty}{\sqrt{1 - e^{\frac{x\pi}{d}}}}$	$u = o$

For small positive x we have

(159) $$v \approx u_\infty \cdot \sqrt{\frac{d}{\pi}} \cdot {}^{1}/_{\sqrt{x}} \ .$$

This is the expected ${}^{1}/_{\sqrt{x}}$ behaviour of v. On the other hand, it can be seen from eqs. (157), that the deviations from this behaviour can become significant.

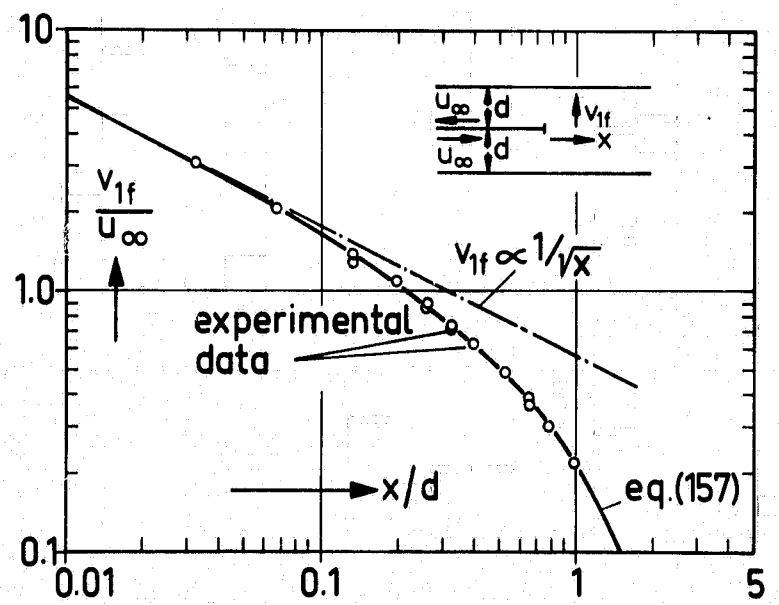

Fig. 18 v-velocity distribution (excitation).

Fig.18 shows a log-log plot of eq. (157) as well as some own experimental data*). As we see, the theory works quite well. A second question of major importance is how far the parabolic pressure field is valid upstream of the plate edge (see Fig. 19). In particular, we are interested in $\Delta p_{12}/\sqrt{l}$ as a reference quantity.

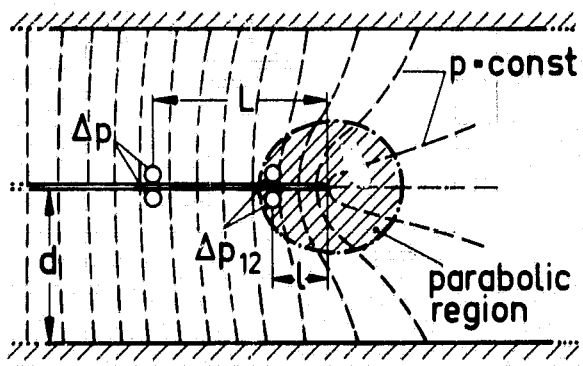

Fig. 19 Reference pressure locations in the test section

Since we can expect a parabolic pressure field only in the near vicinity of the plate edge, we would run into difficulties with measurements of $\Delta p_{12}/\sqrt{l}$ for the following reasons: The pressure difference of the excitation field Δp_{12} becomes small at small distances l from the edge. This leads to poor measurement accuracy. Close to the lip the signals from the (symmetric) pressure field induced by the shear layer dominate and determine the setting of the measurement system. However, for the measurement of the relatively low magnitudes of the pressure difference, the measurement system is then poorly adjusted and the measurements become unsatisfactory. The situation would improve con-

*) The points correspond to pressure gradient measurements $(\partial p/\partial y)$ taken with a probe microphone of ≈1.5 mm resolution, in air at room temperature (22°C) and at a frequency of 200 Hz; d was 75 mm.

siderably, if we could take data of Δp (still at both sides of the splitter plate) further upstream where the pressure levels of the excitation are higher and the induced (symmetric) pressure level of the shear layer would be lower. Consequently, it would be desirable to determine $\Delta p_{12}/\sqrt{I}$, which refers to the parabolic field near the lip, out of a measurement Δp further upstream. We will achieve this with the same method of conformal mapping which we have used before. As we have discussed in section 2.1., the pressure is proportional to the potential for a fluctuating flow field with no mean flow. In analogy to eq. (153) we can set

$$(160) \qquad p = B \cdot \mathrm{Re}\{\ln(\sqrt{1+e^{z_a}}-1) - \ln(\sqrt{1+e^{z_a}}+1)\}$$

where B is a constant which we will determine later. We restrict ourselves to the center line of the channel with $y_a = \pi$ and we replace later x by $\pi x/d$, as before. We find

$$(161) \qquad p = B \cdot \mathrm{Re}\left\{\ln\left(\frac{\sqrt{1-e^{\pi x/d}}-1}{\sqrt{1-e^{\pi x/d}}+1}\right)\right\} .$$

The denominator of the argument of the logarithm will become negative. Since $\ln(-1) = \pm i\pi$. this negative sign will only contribute to the imaginary part of p which we do not consider here. We have therefore as the real part of p

$$(162) \qquad p = B \cdot \ln\left(\frac{1-\sqrt{1-e^{\pi x/d}}}{1+\sqrt{1-e^{\pi x/d}}}\right) .$$

For small x we obtain

$$(163) \qquad p = -2B\sqrt{\pi/d} \cdot \sqrt{-x} \qquad x \to o .$$

This is the expected parabolic pressure field near the plate edge (see also eq. (33) in section 2.1.). On the other hand we

should have

$$(164) \qquad \frac{\Delta p_{12}}{\sqrt{I}} = \frac{2p}{\sqrt{-x}} ,$$

because the pressure difference Δp at both sides of the semi-infinite plate has double the value of the pressure at one side alone. Using equations (163) and (164), we can determine the constant B:

$$(165) \qquad B = -\frac{1}{4}\sqrt{\frac{d}{\pi}} \cdot \frac{\Delta p_{12}}{\sqrt{I}} .$$

Using $\Delta p = 2p$, equations (162), (165) and replacing -x by L (see Fig. 19) we obtain as a final result

$$(166) \qquad \boxed{\frac{p_{12}}{\sqrt{I}} = \frac{\Delta p}{\sqrt{d}} \cdot \frac{2\sqrt{\pi}}{\ln\left(\frac{1+\sqrt{1-e^{-\pi L/d}}}{1-\sqrt{1-e^{-\pi L/d}}}\right)}}$$

This provides the desired relation between the pressure difference Δp at both sides of the splitter plate, measured at an arbitrary distance L from the plate end, the channel width d and the reference quantity $\Delta p_{12}/\sqrt{I}$ (see also Fig. 19). Eq. (166) can be expanded also for $L >> d$ which gives

$$(167) \qquad \frac{\Delta p_{12}}{\sqrt{I}} = \frac{\Delta p}{L} \cdot \sqrt{d} \cdot \frac{2}{\sqrt{\pi}}$$

$$\text{at} \quad (L >> d) .$$

One should keep in mind, however, that L should be much smaller than the acoustic wavelength, which restricts the applicability of eq. (167). It is, therefore, more likely that eq. (166) will be applied in an experiment.

6.3.2. Effects on the resulting shear layer motion

We restrict our considerations to the single stream case where we have a mean flow $\bar{U}_o$ in the lower half of our channel. The general solution for v is still valid, as mentioned above

$$(23) \qquad v_1 = -\frac{\omega}{\bar{U}_o} e^{\lambda_1 x} \int_o^x e^{-\lambda_1 x} v_{1f} dx + \frac{\omega}{\bar{U}_o} e^{\lambda_2 x} \int_o^x e^{-\lambda_2 x} v_{1f} dx$$

with $\lambda_{1,2} = \frac{\omega}{\bar{U}}$ $(i \pm 1)$. For the vertical excitation velocity v_{1f} we have to use now eq. (157)

$$(157) \qquad v_{1f} = \frac{u_\infty}{\sqrt{e^{\frac{x\pi}{d}} - 1}} \quad .$$

We will focus our interest on simple results downstream of the interaction region. In this situation we can neglect the second term of our general solution (eq. (23)), because it represents a rapidly decaying wave. As we know from our previous results, the interaction region is limited to a distance of less than one wavelength of the instability waves. Since v_{1f} is now decaying even more rapidly, we can replace the upper limit of the integral in eq. (23) by infinity. This will provide completely reliable results for $\frac{\omega x}{\bar{U}_o} \gg 1$. So we are left with

$$(168) \qquad v_1 = -u_\infty \cdot \frac{\omega}{\bar{U}_o} \cdot e^{\lambda_1 x} \int_o^\infty \frac{e^{-\lambda_1 x}}{\sqrt{e^{\frac{\pi x}{d}} - 1}} dx$$

for $(\frac{\omega x}{\bar{U}_o} \gg 1)$.

The integral in this equation can be rewritten in the following form

$$(169) \qquad I_1 = \int_0^\infty \frac{e^{-\lambda_1 x}}{\sqrt{e^{\frac{\pi x}{d}}-1}}\,dx = \int_0^\infty \frac{e^{-(\lambda_1+\frac{\pi}{2d})x}}{(1-e^{-\frac{\pi x}{d}})^{\frac{1}{2}}}\,dx \cdot$$

This latter integral can be found between the Laplace transforms in [39]. We obtain

$$(170) \qquad I_1 = \frac{d}{\pi} \cdot B\left(\left(\frac{1}{2} + \frac{\lambda_1 d}{\pi}\right), \frac{1}{2}\right),$$

where B (x,y) is the Beta function (or the Eulerian Integral of the first kind), defined as

$$(171) \qquad B(x,y) = \int_0^1 t^{x-1}(1-t)^{y-1}dt \quad .$$

The function B(x,y) is related to the Γ function

$$(172) \qquad B(x,y) = B(y,x) = \frac{\Gamma(x) \cdot \Gamma(y)}{\Gamma(x+y)}$$

The Γ function (or the Eulerian Integral of the second kind) is defined as

$$(173) \qquad \Gamma(z) = \int_0^\infty e^{-t} \cdot t^{z-1}dt \qquad \text{with } Re(z) > o.$$

Using eqs. (170), (172) and $\Gamma(\frac{1}{2}) = \sqrt{\pi}$ we find

$$(174) \qquad v_1 = -u_\infty \cdot \frac{\omega d}{\bar{U}_o} \cdot \frac{1}{\sqrt{\pi}} \cdot \frac{\Gamma\left(\frac{1}{2} + \frac{\lambda_1 d}{\pi}\right)}{\Gamma\left(1 + \frac{\lambda_1 d}{\pi}\right)} \quad .$$

Before we proceed with the discussion the Γ functions, we have

to establish a relation between u_∞ and our reference quantity $\Delta p_{12}/\sqrt{1}$. We have to expand eq. (157) for small x to obtain the parabolic flow region of the excitation, to which the reference quantity $\Delta p_{12}/\sqrt{1}$ belongs. We find

$$(175) \qquad v_{1f} = u_\infty \sqrt{\frac{d}{\pi x}} \qquad x \to o$$

on the other hand we had (eq. (36))

$$(176) \qquad v_{1f} = -\frac{1}{\sqrt{x}} \cdot \frac{i}{4\rho\omega} \cdot \frac{\Delta p_{12}}{\sqrt{1}} \, .$$

Comparing (175) and (176), we can replace u_∞ in (174)

$$(177) \qquad v_1 = \frac{\Delta p_{12}}{\rho \sqrt{\bar{U}_o \omega l}} \cdot \frac{i}{4} \cdot \sqrt{\frac{\omega d}{\bar{U}_o}} \cdot e^{\lambda_1 x} \cdot \frac{\Gamma(\frac{1}{2} + \frac{\lambda_1 d}{\pi})}{\Gamma(1 + \frac{\lambda_1 d}{\pi})}$$

or, if we use a dimensionless $\tilde{v}_1$, as in section 2

$$(178) \qquad \boxed{\tilde{v}_1 = \frac{i}{4} \cdot \sqrt{\frac{\omega d}{\bar{U}_o}} \cdot \frac{\Gamma(\frac{1}{2} + \frac{\lambda_1 d}{\pi})}{\Gamma(1 + \frac{\lambda_1 d}{\pi})} \cdot e^{\lambda_1 x} \qquad \frac{x\omega}{\bar{U}_o} \gg 1}$$

This is a new analytic solution for the excited instability waves in a channel at $\frac{\omega x}{\bar{U}_o} \gg 1$. The Γ function is tabulated for complex arguments in [31]. However, it is difficult to see what eq. (178) really means. In particular, we are interested to see what the errors are if we use the equations for a free shear layer without walls (section 2) in the present situation in a channel with walls. We want to see by a quantitative calculation under which conditions the previous approach will fail. It makes sense, therefore, to expand eq. (178) for large values of $\lambda_1 d/\pi$.

We will expect then, for decreasing values of $\lambda_1 d/\pi$ (which is proportional to the channel width divided by the wavelength of the instability waves) an increasing deviation from the previous approach.

Fractions of the Γ function can be expanded for large arguments in the following way [31]

$$(179) \qquad \frac{\Gamma(z+a)}{\Gamma(z+b)} = z^{a-b}\left(1+\frac{(a-b)(a+b-1)}{2z}+O(z^{-2})\right).$$

Using this expansion, we end up with:

$$(180) \qquad \tilde{v}_1 = i\,\frac{\sqrt{\pi}}{4\sqrt{i+1}}\left(1-\frac{\pi}{8(i+1)}\cdot\frac{\bar{U}_o}{\omega d}\right) e^{\lambda_1 x}$$

for $\frac{\omega x}{\bar{U}_o} >> 1$ and $\frac{\omega d}{\bar{U}_o} >> 1$.

With exception of the term in brackets, which quantifies the deviation caused by the channel walls, we have obtained the same result as in section 2 (eq. (49) , first term of the instability waves). We are also interested in the modulus of v_1, which is

$$(181) \qquad \boxed{|\tilde{v}_1| = \frac{\sqrt{\pi}}{4\cdot\sqrt[4]{2}}\left(1-\frac{\pi}{16}\cdot\frac{\bar{U}_o}{\omega d}\right) e^{\tilde{x}}}$$

for $\omega x/\bar{U}_o >> 1$ and $\omega d/\bar{U}_o >> 1$, as before. The abbreviations in eq. (181) are the same as in section 2, i.e., $\tilde{x} = \omega x/\bar{U}_o$ and $\tilde{v}_1 = v_1 \rho\sqrt{\omega \bar{U}_o l}/\Delta p_{12}$. Equation (181) is simple enough for a straightforward error analysis. Consider a simple example: $d = 75$ mm, $\omega = 2\pi \cdot 82$ Hz, $\bar{U}_o = 12$ m/s. We end up with a value for $|\tilde{v}_1|$ being about 6 % lower than predicted for a free shear layer without channel walls. This deviation reflects the influence of the limited size of the parabolic excitation region around the end of the semi-infinite plate.

6.3.3. The induced u-velocities

It would be quite complicated to calculate the whole u-velocity field. Therefore, we will restrict ourselves to $\frac{\omega d}{\bar{U}_o} \gg 1$ where we have to consider basically deviations from the $\bar{U}_o$ field computed in section 2. It is quite obvious, that close to the edge of the semi-infinite plate the flow field will be the same as in section 2. If we consider the field upstream of the edge, it is reasonable to assume that the field is dominated by the excitation. Consequently, at sufficient distance upstream of the edge we will obtain $u = \pm u_\infty$ at both sides of the plate. In the intermediate range upstream of the edge, but closer to the edge, the field becomes more complicated. For the upper region with no flow, the u-velocity field can be derived from the known pressure field in a straight forward way, using the first Euler equation. With other words, u is proportional to the x-derivative of the pressure. In the lower half of the flow field, the first Euler equation produces a first order differential equation for u, which has to be solved. The same situation arises, by the way, also for the parabolic flow field in section 2, with the difference, that the resulting functions (error functions) are there easier to deal with.

The situation far downstream from the plate edge becomes much simpler. Here, the amplified instability wave dominates the velocity field. The effect of the channel walls can be taken into account by a simple imaging technique (see Fig. 20)

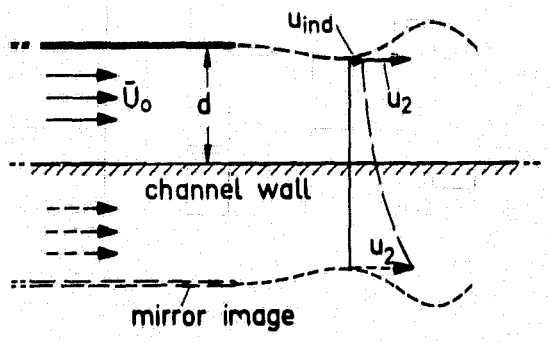

Fig. 20 Imaging technique to model the channel wall.

The decay of the induced velocities in the -y-direction is proportional to $e^{-\frac{|y|\omega}{\bar{U}_o}}$. We know then, that the u_2-velocity at the shear layer will be increased by an amount $(1 + e^{-\frac{2\omega d}{\bar{U}_o}})$. Using the fact, that at $\frac{\omega x}{\bar{U}_o} \gg 1$ we have $|v_1| = |v_2| = |u_1| = \bar{U}_o |u_2|$ for a shear layer without walls, we obtain for the situation in the channel

$$|u_2| = |v_1| \cdot (1+e^{-\frac{2\omega d}{\bar{U}_o}}) \quad (182)$$

$$(\frac{\omega x}{\bar{U}_o} \gg 1).$$

To give a numerical example, we take the same data as before, namely: $d = 75$ mm, $\omega = 2\pi \cdot 82$ Hz, $\bar{U}_o = 12$ m/s. We find a very weak influence of the wall of 0.16 %. This influence will become even weaker because the decay rate in y-direction will become higher in a real experimental situation, as discussed in sections 6.1. and 6.2. We end up with the conclusion in this section, that the enhancing influence of direct reflection on the u-velocity at the wall is usually much smaller than the more indirect decreasing influence via the change of the excitation field.

7. Speculations

One may contemplate about the question on how far the present approach can be stretched to really include the excitation of a shear layer with small, but finite thickness. In section 5 (two stream case) we have considered an example where the amplification rate and the wave number can depend, albeit differently, on exteriour parameters like $\sigma = \bar{U}_1/\bar{U}_2$ and $\beta = \rho_1/\rho_2$. It is tempting to write an equation like eq. (119) where the coefficients on the left hand side are made up from amplification rates and wave numbers obtained from numerical results of the stability theory of infinitely extended shear flows, such as [6] and [37]. It is not clear, whether or not this idea leads to a viable and correct analytic approach. However, it would be interesting to see how far the concept can be generalized, that the resulting excited instability wave is a finite Laplace trans-

form (such as eqs. (37)and (123))of an exteriour excitation field. In addition, extensions of such an approach to other configurations like jets or even to the excitation of instability waves on a flat plate might be conceivable.

Another relevant question is, how far free stream turbulence (or other types of turbulence) and its wavy predecessors which we investigate here, are "natural" or dependent on exteriour forcing. We might consider whether or not an influence from the downstream nonlinear development might provide a sufficient or even dominant feedback. Our pressure source approach is still useful to provide a feeling for this situation. The pressure linearization is the last to break down with increasing fluctuation magnitude and it works nicely for subsonic flows. The effect of the nonlinear flow evolution on the pressure sources is this: During the vortex roll-up we have a limitation to the magnitude of the pressure sources. The reaction to the trailing edge is necessarily very small*), because the pressure sources are still only located in the shear layer (outside the shear layer we still have $\nabla^2 p = 0$), i.e., in the symmetry plane and we get a situation close to creating a stagnation point of the induced flow at the trailing edge (see also section 4). The feedback is therefore strongly dependent upon the local displacements of the shear layer. Therefore, a feedback is likely to be a nonlinear effect, and it is very weak. Thus, it can be easily dominated by sound waves or convected vorticity, as shown in numerous experiments. Nevertheless, we cannot completely reject this mechanism,because the upstream influence decreases in a non-exponential manner in the upstream direction whereas the downstream amplification of the instability waves is exponential. Under these circumstances (and with an unstable shear layer), there is no way to keep the flow laminar even if there is only Brownean motion as an initial excitation somewhere.

There is, however, another way in which feedback may come into play.

*) The situation changes dramatically if a rigid body, like an additional wedge, is introduced into the flow field. Then, an asymmetric pressure field is created which has a strong influence on the trailing edge.

All our previous considerations were based on symmetric boundary conditions. To provide a feeling for slightly asymmetric conditions we consider the geometrically symmetric configuration of section 6, where we excited a shear layer in the center line of a channel. If the conditions upstream of the splitter plate are not symmetrical (caused, say, by a difference in the acoustic impedance in both legs of the bisected channel), a pressure source in the shear layer creates an asymmetric pressure field in the channel and hence a parabolic local field at the edge of the splitter plate. In this way, in particular if there is resonance in one leg of the bisected channel, a linear feedback is conceivable.

8. Conclusions and survey of essential results

The acoustic excitation of a free shear layer shed from a semi-infinite plate has been studied. The shear layer is assumed to be infinitesimally thin. The present consideration is limited to a low Mach number mean flow and to the situation where all typical dimensions of the problem are small compared to the acoustic wavelength. This leads to an incompressible flow approach relevant to the interaction region near the end of the plate. The basic contributions and findings of this paper are listed below.

1) The basic shear layer - sound interaction model is outlined. The solutions are obtained by splitting the pressure field into two constituents:

   (a) the forcing pressure field of the exteriour excitation and

   (b) the pressure field which is radiated by the shear layer itself.

   The consideration of the pressure gradients perpendicular to the shear layer leads to an equation for the v-velocity components v_1 and v_2 at both sides of the shear layer. A second equation for both components is derived from the

condition, that the displacement h on both sides of the shear layer should be equal. Both equations can be condensed into one nonhomogeneous differential equation for v_1. A general solution for this equation is derived. For a parabolic excitation pressure field around the plate, which is the most common case, a special solution is given. So far the basic approach of this paper follows a previous one [12].

2) It is proved that only the "Kutta condition" solution fulfills the boundary conditions of equal displacement and pressure on both sides of the shear layer. Within the limits of this model, it is proved, that only forced instability waves exist. It is shown, that no ambiguity is left in the excitation mechanism.

3) For the parabolic excitation field, also analytic solutions for u_1 and u_2 at both sides of the shear layer are calculated. For $x > o$ this solution consists only of a damped and an amplified instability wave.

4) Numerical calculations of u_2 (velocity fluctuations in the region of existing mean flow) are carried out for $y \neq o$. The u_2 computations are of crucial importance for the comparison with experimental data. The calculation utilizes a source distribution approach and is based on the analytically given v_2 velocity distribution. Also simple asymptotic formulae for the field outside the interaction region at the plate edge are given. Thus, the region of numerically computed velocities is completely imbedded into asymptotic equations and fits also the analytic solution at $y = -o$. In addition, the computations have been carried out by two different persons using different mathematical procedures, computer languages and computers. Therefore, the numerical computations can be considered as a reliable bridge between the analytical solutions for u and v, derived from separate calculations. This is also part of the proof 2) that the forced instability waves do

fulfill all boundary conditions and additional arbitrary instability waves do not exist.

5) The excitation by different types of sources in various locations is discussed. With the exception of the (singular) cases if either

   (a) the excitation field has a stagnation point at the plate edge or

   (b) the excitation is directly located at the plate edge itself,

   the exteriour excitation creates a parabolic pressure near field at the plate edge which dominates the control of the shear layer. The possible existence of a stagnation point (case (a)) is demonstrated with a dipole excitation at a certain orientation with respect to the plate. The effect of a monopole source on the shear layer is investigated in detail (see Fig. 21).

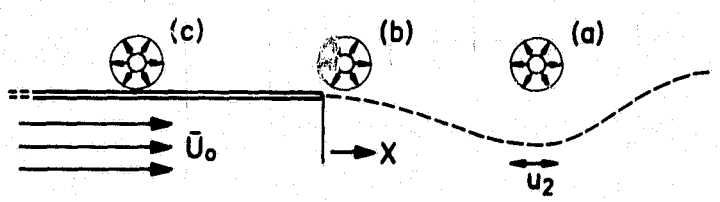

Fig. 21 Excitation by a monopole source in different locations

A monopole in position (a) nearly creates a stagnation point at the plate edge. Therefore, this type of excitation is very inefficient. The excitation by a feedback from downstream turbulence would be also of this type. A source in position (c) would produce a strong parabolic excitation

field and would be by orders of magnitude more efficient than an excitation in position (a). This is the reason why free shear layers are so sensitive to sound waves from upstream and so insensitive to the strong near field pressure created by the turbulence.

The excitation directly at the plate edge (b) has been used in some recent experiments. It was not clear, however, what the relevant reference quantities were. An expansion for small distances provides an elegant and simple result:

$$(183) \qquad |u_2| = \frac{Q\omega}{2\bar{U}_o} \cdot e^{\frac{\omega(x-|y|)}{\bar{U}_o}} \qquad \text{for } \frac{\omega x}{\bar{U}_o} > 1$$

For this case also a complete solution for the shear layer motion at all x can be given, as well as an analytic solution for the whole induced field at $y \neq o$, in terms of exponential integrals of complex arguments (this function is tabulated in [31]). The result in eq. (183) refers to the fact, that 1/2 of the volume flux Q of the source penetrates through the line y = o. In a real experimental situation, this ratio might be higher, maybe closer to 1, depending on the individual configuration of the excitation device at the lip.

6) The major part of this paper, however, deals with the excitation by a parabolic field at the plate edge, which is created by any source far away from the edge. It is shown, that in this "parabolic" case the interaction takes place within less than one wavelength (of the instability waves) downstream of the plate edge. Downstream of this interaction region, the v-velocity field (at $y = \pm o$) splits into one contribution of a pure amplified instability wave and another contribution from the excitation alone.

7) The theory is also extended to the "two stream case", where we have two different mean velocities and densities above

$(\bar{U}_1,\rho_1)$ and below $(\bar{U}_2,\rho_2)$ the shear layer. Although the details of the calculations become somewhat awkward, the mathematical results are still very similar to the preceding ones. The quantity in the excitation field that is most easily dealt with is again the pressure, and it becomes clear, that pressure gradients $(\partial p/\partial y)$ rather than velocities drive the shear layer. Again, the far field downstream of the interaction region splits into an amplified instability wave and a forcing velocity distribution which is continuous through the shear layer. Since the densities on both sides of the shear layer are different, nature prefers the average value of both densities as a coefficient in front of this forcing velocity. The consequences of the introduction of the new parameters $\sigma = \bar{U}_1/\bar{U}_2$ and $\beta = \rho_1/\rho_2$ are the following:

(a) the downstream amplification rate of the instability waves is reduced for reduced difference of the velocities, as expected;

(b) if the low speed region has a lower density than the high speed region, the amplification rate is also reduced.

8) The present theory predicts potential fluctuations outside an infinitesimally thin shear layer. In an experiment, however, we have always a shear layer of finite thickness. Nevertheless, at low Strouhal numbers S_θ, both theories provide the same potential field outside the shear layer (if the instability wave is fully established downstream of the plate). By matching both (identical) potential fields, we can predict also the motion inside the shear layer, as calculated by Michalke [6].

9) Obviously, the influence of finite shear layer thickness leads also to deviations from the present model. If the data acquisition in an experiment relies on measurements in the potential field outside the shear layer, we have to consider in how far the wave number in the real case

deviates from our idealized case. The wave number is an essential quantity, because it determines the decay rate of the induced field perpendicular to the shear layer (y-direction). From Michalke's [6] and Freymuth's [7] results it is clear that the wave number becomes higher than in our model for increasing S_θ. This leads also to an increased decay rate in the y direction.

10) Another typical deviation in experimental setups is the "overshoot" (mean flow gradient) near the shear layer. It is not too difficult to model this. The analysis yields an increased wave number, which again enhances the decay rate of the induced velocities in the y-direction. Interestingly enough, the downstream amplification rate of the instability waves remains almost unchanged.

11) In a typical experimental situation the two streams at both sides of the shear layer are limited in their width. Thus, in reality, we have a shear layer in a channel rather than a free shear layer in an unlimited flow. There are several things to be considered:

(a) the general solution of the shear layer motion is still the same,

(b) the excitation pressure field, however, is changed. There is no difficulty, though, to calculate it with conformal mapping. The excitation pressure field is still parabolic in the vicinity of the splitter plate edge, but it falls off exponentially beyond a certain distance in the downstream direction.

(c) With this new excitation pressure field the shear layer motion can be calculated, at least downstream of the interaction region. The analytical solution contains Γ-functions of complex argument. Since this solution is quite awkward to handle, it is expanded for large $\omega d/\bar{U}_o$, where d is the channel halfwidth. This means that the wavelength of the instability

waves should be relatively small compared to the channel half-width. We end up with a reduction of the instability wave magnitude, represented by the coefficient $(1-\pi\omega d/16\bar{U}_o)$. In comparison to this quite significant influence on the magnitude, it turns out, that

(d) the direct reflection influence of the channel walls on the velocity distribution is quite insignificant (close to the shear layer) as far as the instability wave downstream of the plate edge is concerned.

12) Perhaps the most significant finding of the present paper is a reference quantity for the excitation of a shear layer by a parabolic pressure field, which is a fairly general case, as discussed in paragraph 5). It is the

reference quantity $\Delta p_{12}/\sqrt{l}$

The significance of Δp_{12} and l can be seen in Fig. 22. $\Delta p_{12}/\sqrt{l}$ is related to the excitation field only. It will not change, e.g., if the mean flow $\bar{U}_o$ is switched off. For instance, the u_2-velocity of the instability waves close to the shear layer depends on $\Delta p_{12}/\sqrt{l}$ in the following way:

$$(184) \qquad |u_2| = \frac{|\Delta p_{12}|}{\sqrt{l}} \cdot \frac{1}{\rho\sqrt{\omega\bar{U}_o}} \cdot \frac{\sqrt{\pi}}{4\cdot\sqrt[4]{2}} \cdot e^{\frac{\omega x}{\bar{U}_o}}$$

valid for $\omega x/\bar{U}_o > 2$

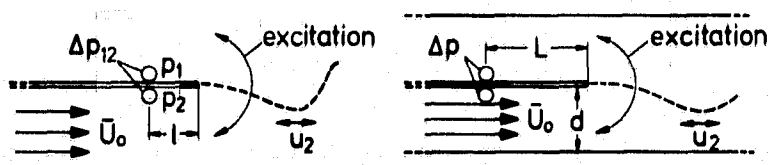

Excitation in free conditions

Excitation in a channel

Fig. 22 Configurations for shear layer excitation.

Equation (184) is well confirmed by recent, yet unpublished, measurements of the author.

For an experiment in a channel (see Fig. 22), the situation changes slightly. If the two microphones used to measure Δp at both sides of the splitter plate are moved further upstream (to improve the accuracy of the measurements), we have

$$(185) \qquad \frac{\Delta p_{12}}{\sqrt{l}} = \frac{\Delta p}{\sqrt{d}} \cdot \frac{2\sqrt{\pi}}{\ln\left[\frac{1+\sqrt{1-e^{-\pi L/d}}}{1-\sqrt{1-e^{-\pi L/d}}}\right]}$$

The significance of L and d can be seen in Fig. 22. The magnitude of the instability waves is then the value provided by eq. (184), but multiplied by the coefficient $(1-\pi\omega d/16\ \bar{U}_o)$. The latter coefficient (see paragraph 11) reflects the limited size of the parabolic pressure distribution at the plate edge in the channel.

Acknowledgement

The present work has been sponsored partly by NASA Lewis and by the Deutsche Forschungsgemeinschaft. The field calculations in section 3 are a repetition of earlier computations done by Dr. M.

Nallasamy (University of Houston). He was also responsible for the elimination of some numerical convergence problems in this section. The author was encouraged by Professor A.K.M.F. Hussain (University of Houston) to carry out this research. He arranged also for the author's visit to Houston in this joint U.H.-DFVLR project. The author is also indebted to Dr. W.F. King, DFVLR Berlin, for a careful review of this paper. In addition to the present theoretical study, an experimental investigation was also carried out. These results will be published separately.

9. References

[1] Leconte, J. — On the influence of musical sounds on the flame of a jet of coal-gas. The London, Edinburgh, and Dublin Philosophical Magazine and Journal of Science. 15 (1858), pp. 235-239.

[2] Tyndall, J. — Sound.
London: Longmans, 1867.
Also available in German:
Der Schall.
(Editors: H. v. Helmholtz and G. Wiedemann)
Braunschweig: Viehweg, 1874.

[3] Rayleigh, Lord, J.W.S. — On the stability, or instability, of certain fluid motions.
Proc. of the London Math. Soc. 11 (1880), pp. 57-70.

[4] Gaster, M. — A note on the relation between temporally-increasing and spatially-increasing disturbances in hydrodynamic stability.
J. Fluid Mech. 14 (1962), pp. 222-224.

[5] Watson, J. — On spatially-growing finite disturbances in plane Poiseuille flow.
J. Fluid Mech. 14 (1962), pp. 211-221.

[6] Michalke, A. — On spatially growing disturbances in an inviscid shear layer.
J. Fluid Mech. 23 (1965), pp. 521-544.

[7] Freymuth, P.
On transition in a separated laminar boundary layer.
J. Fluid Mech. 25 (1966), pp. 683-703.

[8] Tam, C.K.W.
Excitation of instability waves in a two-dimensional shear layer by sound.
J. Fluid Mech. 89 (1978), pp. 357-371.

[9] Orszag, S.A.
Crow, S.C.
Instability of a vortex sheet, leaving a semi-infinite plate.
Studies Appl. Math. 49 (1970), pp. 167 - 181.

[10] Crighton, D.G.
Leppington, F.G.
Radiation properties of the semi-infinite vortex sheet: the initial value problem.
J. Fluid Mech. 64 (1974), pp. 393-414.

[11] Howe, M.S.
The influence of vortex shedding on the generation of sound by convected turbulence.
J. Fluid Mech. 76 (1976), pp. 711-740.

[12] Bechert, D.W.
Michel, U.
The control of a thin free shear layer with and without a semi-infinite plate by a pulsating flow field.
ACUSTICA 33 (1975), pp. 287-307.

[13] Möhring, W.
On flows with vortex sheets and solid plates.
J. Sound & Vibr. 38 (1975), pp. 403-412.

[14] Bechert, D.W.
Die Steuerung eines ebenen turbulenten Freistrahls durch eine seitliche Wechselströmung, erzeugt in einem Schallfeld.
Z. Flugwiss. 24 (1976), pp. 25-33.

[15] Crow, S.C.
Champagne, F.H.
Orderly structure in jet turbulence.
J. Fluid Mech. 48 (1971), pp. 547-591.

[16] Brown, G.L.
Roshko, A.
On density effects and large structure in turbulent mixing layers.
J. Fluid Mech. 64 (1974), pp. 775-816.

[17] Mensing, P.
Einfluß kontrollierter Störungen auf eine ebene turbulente Scherschicht.
Dissertation: Techn. Univ. Berlin, Fachbereich 9, 1981.

[18] Dziomba, B.
Experimentelle Untersuchung zum Einfluß von Anfangs- und Randbedingungen auf die Ausbreitung einer freien zweidimensionalen Scherschicht.
Dissertation: Techn. Univ. Berlin, Fachbereich 9, 1981.

[19] Bechert, D.W.
Pfizenmaier, E.
On the amplification of broad band jet noise by a pure tone excitation.
J. Sound & Vibr. 43 (1975), pp. 581-587.

[20] Bechert, D.W.
Pfizenmaier, E.
Amplification of jet noise by a higher-mode acoustical excitation.
AIAA Journal 15 (1977), pp. 1268-71.

[21] Moore, C. J.
The role of shear-layer instability waves in jet exhaust noise.
J. Fluid Mech. 80 (1977), pp. 321-367.

[22] Deneuville, P.
Jaques, J.
Jet noise amplification: a practically important problem.
AIAA 4th. Aeroacoustics conference, Atlanta/Ga., Oct. 3-5, 1977
AIAA paper 77-1368.

[23] Schmidt, C.
Aerodynamic characterization of excited jets.
J. Sound & Vibr. 61 (1978), pp. 148-152.

[24] Hodge, C.G.
Tam, C.K.W.
Aeroacoustics in: Aerospace highlights 1981.
Astronautics & Aeronautics (1981), pp. 28-29.

[25] Vlasov, Y.V.
Ginevski, A.S.
Generation and suppression of turbulence in an axisymmetric turbulent jet in the presence of an acoustic influence.
NASA TT F-15721
Translation of: Generatsiya i podavleniyo turbulentnosti v osesimmetrichnoy turbulentnoy struye pri akusticheskom vordeystvii.
Izvestiya Akademiya Nauk SSSR, Mekhanika Zhidk., Gaza 6, Nov.-Dec. 1973, pp. 37-43.

[26] Zaman, K.B.M.Q.
Hussain, A.K.M.F.
Turbulence suppression in free shear flows by controlled excitation.
J. Fluid Mech. 103 (1981), pp. 133-159.

[27] Mechel, F.
Ronneberger, D.
Experimentelle Untersuchung der Schallausbreitung in luftdurchströmten Rohren mit Querschnittsänderungen.
5th. International Congress on Acoustics, Liège, 1965. Paper K23.

[28] Bechert, D.W.
Sound absorption caused by vorticity shedding, demonstrated with a jet flow.
J. Sound & Vibr. 70 (1980), pp. 389-405.

[29] Howe, M.S.
Attenuation of sound in a low Mach number nozzle flow.
J. Fluid Mech. 91 (1979), pp. 209-229.

[30] Howe, M.S.
The dissipation of sound at an edge.
J. Sound & Vibr. 70 (1980), pp. 407-411.

[31] Abramovitz, M.
Stegun, I.A.
(Editors)
Handbook of mathematical functions.
New York: Dover Publications, 1970.

[32] Pfizenmaier, E.
Zur Instabilität des schallbeeinflußten Freistrahls.
DLR-FB 73-69, (1973).
Available in English:
On the instability of a sound-influenced free jet.
ESRO TT 122.

[33] Möhring, W.
personal communication.
Max-Planck-Institut für Strömungsforschung, Göttingen, 1973.

[34] Howe, M.S. — personal communication. Bolt, Beranek & Newman, Cambridge/ Mass., USA, 1981.

[35] Bronstein, I.N. Semendjajew, K.A. — Taschenbuch der Mathematik 19. Auflage. Frankfurt/M.: Verlag Harri Deutsch, 1980. (Translation from Russian, also available in English).

[36] Bechert, D.W. Michel, U. — The control of a thin free shear layer with and without a semi-infinite plate with a pulsating monopole or dipole. Some new closed form solutions. DLR-FB 74-22, (1974).

[37] Monkewitz, P.A. Huerre, P. — Influence of the velocity ratio on the spatial instability of mixing layers. to be published in: Phys. of Fluids.

[38] Kober, H. — Dictionary of conformal representations. New York: Dover Publications, 1957.

[39] Gradstein, I.S. Ryshik, I.M. — Tables of series, products and integrals. Frankfurt/M.: Verlag Harri Deutsch, 1981 (Translation from Russian).

[40] Spurk, J.H. — personal communication. Technical University of Darmstadt, 1976.

[41] Bechert, D.W.
Pfizenmaier, E.
Optical compensation measurements on the unsteady exit condition at a nozzle discharge edge.
J. Fluid Mech. 71 (1975), pp. 123-144.

[42] Bechert, D.W.
Pfizenmaier, E.
On the Kutta condition at the nozzle discharge edge in a weakly unsteady nozzle flow.
RAE Lib. Trans. No. 1617 (1971),
Translation from: DLR-FB 71-09 (1971).

C-2

10. Appendices

10.1. Appendix A

Glossary of symbols

a_o	sound speed
$a_1 \div a_6$	constants in the numerical representation of the error function erf of a real argument
b_1, b_2	lower and upper boundary of a vorticity distribution on the x-axis (see Fig. 7)
c_{ph}	phase velocity of an instability wave
$c_{ph\ rel}$	relative phase velocity of an instability wave $c_{ph\ rel} = c_{ph}/\bar{U}_2$
d	half width of a two-dimensional channel (see Fig. 17)
erf(z)	error function, defined as $\mathrm{erf}(z) = \frac{2}{\sqrt{\pi}} \int_0^z e^{-t^2} dt$
erfc(z)	complementary error function erfc(z) = 1-erf(z)
f	frequency of the excitation $f = \omega/2\pi$
g_1, g_2	lower and upper boundary of a source distribution on the x-axis (see Fig. 8)
h	displacement of the shear layer due to the instability waves and the excitation field
i	imaginary unit $i = \sqrt{-1}$
l	distance between the edge of the semi-infinite plate and the pressure pickup devices (e.g., microphones) at both sides of the plate

m, n	summation variables (integer)
p	pressure, usually the perturbation pressure, i.e., the deviation from the ambient (atmospheric) pressure. All perturbation quantities are proportional to $e^{-i\omega t}$
p_1	fluctuating pressure above the shear layer at $y > o$
p_2	fluctuating pressure below the shear layer at $y < o$
Δp, Δp_{12}	pressure difference between both sides of the semi-infinite plate
$\dot{p}$	abbreviation of a quantity related to a pressure gradient in y-direction, i.e., $\dot{p} = -\frac{2i}{\rho_2 \omega} \cdot \frac{\partial p_{2f}}{\partial y}$
p_{1f}, p_{2f}	contribution of the exteriour forcing field to the total fluctuating pressure. $p_{1f} = p_{2f}$
p_{1s}, p_{2s}	contribution of the shear layer field to the total fluctuating pressure. p_{1s} is valid for $y > o$ and p_{2s} is valid for $y<o$. In addition we have $p_1 = p_{1f} + p_{1s}$; $p_2 = p_{2f} + p_{2s}$.
q, $q(\xi)$	source distribution on the x-axis; dimension like a velocity.
r	radius or distance from the origin (in most cases the splitter plate edge) to the considered field point $r = \sqrt{x^2 + y^2}$
r_o	distance between the location of a point source and the splitter plate edge $r_o = \sqrt{x_o^2 + y_o^2}$

s	integration variable (eq. (38))
t	time
τ	integration variable, e.g., in eqs. (171) and (173)
u	fluctuating velocity component in the x-direction; all fluctuating quantities are proportional to $e^{-i\omega t}$
u_1	fluctuating u velocity component above the shear layer at $y > o$
$u_{1\lambda 1}$	u-velocity induced by a v velocity distribution of an amplified Helmholtz instability wave (exponent λ_1) in the half-plane above the shear layer ($y > o$). The v distribution of the instability wave exists only for $x > o$.
$u_{1\lambda 2}$	similar to $u_{1\lambda 1}$, but referring to the attenuated Helmholtz instability wave (exponent λ_2)
u_∞	fluctuating u-velocity in a channel with a splitter plate, asymptotic value far upstream of the trailing edge of the splitter plate
u_2	fluctuating u velocity component below the shear layer at $y < o$
$u_{2\lambda 1}$	similar to $u_{1\lambda 1}$, but valid below the shear layer ($y < o$)
$u_{2\lambda 2}$	similar to $u_{1\lambda 2}$, but valid below the shear layer ($y < o$)
u_{2D}	u-velocity, induced by v_{2D} at $y < o$. v_{2D} is the difference between the forced instability wave v_2 and the asymptote which behaves like the Helmholtz

instability wave v_{2H}; $v_{2D} = v_2 - v_{2H}$. v_{2D} becomes zero both at $x = -\infty$ and $x = +\infty$.

Δu_{2D} — u-velocity, induced by just one trapezoidal source element representing the local v_{2D} distribution between two neighboring points ξ_a and ξ_b.

u_{2DI} — imaginary part of u_{2D}

u_{2DR} — real part of u_{2D}

u_{2I} — imaginary part of u_2

u_{2R} — real part of u_2

u_2^δ — u-velocity component induced by a point source located at $y = o$ and $x = o$.

$u_{C.L.}$ — center line velocity (at the splitter plate) in the two-dimensional channel

$\tilde{u}$ — dimensionless form of the u velocities (with various indices, as given above) in the following form

$$\tilde{u} = \frac{u \cdot \rho\sqrt{\bar{U}_o \omega l}}{\Delta p_{12}}$$

in the two stream case ρ has to be replaced by ρ_2 and $\bar{U}_o$ by $\bar{U}_2$

u_{ind} — velocity induced by the mirror image of the shear flow representing the wall in a channel flow

v — fluctuating velocity component in the y-direction, all fluctuating quantities are proportional to $e^{-i\omega t}$

v_1 — v-velocity component above the shear layer at $y > o$

v_{1f}	v-velocity component at y > o, generated by the exteriour forcing field
v_{1s}	v-velocity component at y > o, generated by the shear layer; $v_1 = v_{1f} + v_{1s}$
v_{1D}	difference between the forced instability wave v_1 and its asymptote v_{1H}, which behaves like an amplified Helmholtz instability wave. $v_{1D}=v_1-v_{1H}$ (valid for y > o)
v_{1I}	imaginary part of v_1 (valid for y > o)
v_{1R}	real part of v_1 (valid for y > o)
v_{1DI}	imaginary part of v_{1D} (valid for y > o)
v_{1DR}	real part of v_{1D} (valid for y > o)
v_{1H}	asymptotic behaviour of the v_1 component of the forced instability wave, assumes the form of a Helmholtz instability wave, amplified in the downstream direction (valid for y > o)
v_2	v-velocity component below the shear layer at y < o
v_{2D}	difference between the forced instability wave v_2 and its asymptote v_{2H}, which behaves like an amplified Helmholtz instability wave. $v_{2D}=v_2-v_{2H}$ (valid for y < o)
v_{2DI}	imaginary part of v_{2D} (valid for y < o)
v_{2DR}	real part of v_{2D} (valid for y < o)
v_{2H}	asymptotic behaviour of the forced instability wave, assumes the form of a Helmholtz instability wave, amplified in the downstream direction (valid

for $y < o$)

$\tilde{v}$ — dimensionless form of the different v-velocities as given above, i.e.,

$\tilde{v} = \dfrac{v \cdot \rho\sqrt{\bar{U}_o \omega l}}{\Delta p_{12}}$; in the two stream case ρ has to be replaced by ρ_2 and $\bar{U}_o$ by $\bar{U}_2$

$v_{a,b}$ — v-velocities at the lower and upper end of a trapezoidal source distribution. The local strength of a plane source distribution is two times the local v-velocity just above the distribution

x — horizontal coordinate

$\tilde{x}$ — nondimensional horizontal coordinate $\tilde{x}=x\omega/\bar{U}_o$ or $\tilde{x}=x\omega/\bar{U}_2$ for the two stream case

y — vertical coordinate

$\tilde{y}$ — nondimensional vertical coordinate $\tilde{y}=y\omega/\bar{U}_o$

z — complex variable, usually defined as $z=x+iy=re^{i\vartheta}$

$\bar{z}$ — complex conjugate of z; $\bar{z} = x-iy = re^{-i\vartheta}$

A — constant, used on different occasions:
in eq. (31) it defines the strength of a pressure field
in eqs. (67) and (140) it defines the strength of a potential
in eq. (155) it is a constant with the dimension of a velocity, $A = u_\infty$

A — in the appendix D, eq. (D3), A is the real part of a complex variable in conjunction with a computer program which uses the same symbol

ABS(z) — modulus of a complex quantity , e.g., ABS(z) = $\sqrt{x^2 + y^2}$

B — constant, used on different occasions: in eq. (67) it defines the strength of a potential; in eq. (160) it defines the strength of a pressure field

B — in the appendix D, eq. (D3), B is the imaginary part of a complex variable in conjunction with a computer program which uses the same symbol

$B_{(x,y)}$ — Beta function, Euler's integral of the first kind (see also [31, 39]), defined as

$$B_{(x,y)} = \int_0^1 t^{x-1}(1-t)^{y-1}dt$$

C_1, C_2 — constants (can be complex) with the dimension of a velocity, defining the magnitude of the amplified (C_1) and decaying (C_2) Helmholtz instability wave

D — Dipole strength

$E_{1(z)}$ — Exponential integral, defined as (see also [31])

$$E_1 = \int_z^\infty \frac{e^{-t}}{t} dt$$

G_1, G_2 — lower boundaries of the integrals in eq. (23); their existence is equivalent to the existence of additional Helmholtz instability waves

G_3, G_4 — lower boundaries of the integrals in eq. (66)

$H_{(x)}$, $H_{(\xi)}$	Heaviside unit step function $H_{(x)} = 0$ for $x < 0$ and $H_{(x)} = 1$ for $x > 0$
I	imaginary part of a complex quantity as used in the appendix D, $z = R + iI$, in conjunction with a computer program using the same symbols
I_1	integral, defined by eq. (169)
Im{}	imaginary part of a complex quantity in brackets
L	distance between splitter plate edge and the location of the pressure pickup devices (e.g., microphones) at both sides of the splitter plate in a channel (see Figs. 19, 22)
M	Mach numer, e.g., $M = \bar{U}_o/a_o$
O	e.g., in $O(z^{-2})$: of the order of z^{-2}
P	Fourier transform of the pressure
P_1, P_2	points above and below the shear layer at which induced velocities are considered
Q, Q_o	source strength $Q = Q_o e^{-i\omega t}$; Q, Q_o have the dimension of a velocity times a length
R	radius of a nozzle (used only in the introduction)
R	cylinder radius (eq. (31))
R	real part of a complex quantity as used in the appendix D, $z = R + iI$, in conjunction with a computer program using the same symbols
Re{}	real part of a complex quantity in brackets
RS	right hand side of eq. (119)

S	source strength of a pressure source
S_θ	Strouhal number calculated with the momentum thickness of the shear layer and defined as $S_\theta = f \cdot \theta/\bar{U}_0$
T, $\bar{T}$	abbreviations for complex quantities $T = 1 + \frac{i(r_0+x_0)}{y_0}$; $\bar{T} = 1 - \frac{i(r_0+x_0)}{y_0}$
$\bar{U}$, $\bar{U}_{(y)}$	mean flow velocity, it has only a component in the x-direction
$\bar{U}_0$	mean flow velocity for $y < 0$
$\bar{U}_1$	mean flow velocity (in the two stream case) for $y > 0$
$\bar{U}_2$	mean flow velocity (in the two stream case) for $y < 0$
α	angle of the radius vector in the z_a-plane; $z_a = x_a + iy_a = r_a e^{i\alpha}$
α	complex wave number as defined usually in the stability theory. The relation to our nomenclature is the following: $i\alpha = \lambda$
β	angle of the radius vector in the z_b-plane; $z_b = x_b + iy_b = r_b e^{i\beta}$
κ	ratio of the densities at both sides of the shear layer; $\kappa = \rho_1/\rho_2$
γ	strength of a vorticity distribution, located on the x-axis. It has the dimension of a velocity
$\delta(x-x_0)$	delta function at the location $x = x_0$

ζ quantity defining the slope of a shear layer $\zeta = 1/2\vartheta$

η Fourier transform variable, corresponding to y

ϑ angle of the radius vector in the z-plane; $z = x + iy = re^{i\vartheta}$

λ complex wave number of the instability waves in a shear layer. The relation to the conventional wave number α in the stability theory is $\lambda = i\alpha$

$\lambda_{1,2}$ complex wave number, defined

(i) for a flow below the shear layer with $\bar{U}=\bar{U}_o$ and zero flow above the shear layer as $\lambda_{1,2} = \frac{\omega}{\bar{U}_o}(i+1)$; the positive sign corresponds to λ_1 and the negative sign to λ_2

(ii) for a flow with different velocities ($\bar{U}_1$, $\bar{U}_2$) at both sides of the shear layer and with different densities (ρ_1, ρ_2) as

$$\lambda_{1,2} = \frac{\omega}{\bar{U}_2} \cdot \frac{1}{1+\sigma^2\beta}\left[i(1+\sigma\beta) \pm (1-\sigma)\sqrt{\beta}\right]$$

(iii) for a flow below the shear layer with uniform gradient $d\bar{U}/dy$ and the value $\bar{U}=\bar{U}_o$ at the shear layer (y=-o) and with zero flow above the shear layer

$$\lambda_{1,2} = \frac{\omega}{\bar{U}_o}\left[i\left(1+\frac{d\bar{U}/dy}{2\omega}\right) \pm \sqrt{1-\left(\frac{d\bar{U}/dy}{2\omega}\right)^2}\right]$$

$\tilde{\lambda}_{1,2}$ is the corresponding dimensionless wave number with $\tilde{\lambda}_{1,2} = \lambda_{1,2} \cdot \frac{\bar{U}_o}{\omega}$ or $\lambda_{1,2} \cdot \frac{\bar{U}_2}{\omega}$ for the two stream case

ν	Fourier transform variable, corresponding to x
ξ	integration variable for source and vorticity distribution on the x axis; ξ has the same direction as x
$\xi_{a,b}$	lower and upper boundaries of a trapezoidal source distribution element
ξ_1	lower boundary for the integral over a continuous source distribution $q_{(\xi)}$ with $q_{(\xi)} \propto 1/\sqrt{\xi}$
ξ_2	upper boundary for the integral over a parabolic source distribution $q_{(\xi)}$ with $q_{(\xi)} \propto \sqrt{\xi}$
$\Delta\xi$	stepwidth (length) of a trapezoidal source element
ρ	density of the fluid
ρ_1	density of the fluid above the shear layer ($y > o$)
ρ_2	density of the fluid below the shear layer ($y < o$)
σ	velocity ratio of the two stream case with $\sigma = \bar{U}_1/\bar{U}_2$, $\bar{U}_1$ being the mean flow velocity above the shear layer ($y > o$) and $\bar{U}_2$ being the mean flow velocity below the shear layer ($y < o$)
τ	complex constant in eq. (93)
φ_1, φ_2	amplified and decaying Helmholtz instability waves
ω	radian frequency of the exteriour excitation $\omega = 2\pi f$
$\Gamma_{(z)}$	Gamma function; Euler's integral of the second kind, defined as $\Gamma_{(z)} = \int_o^\infty e^{-t} \cdot t^{z-1} dt$

θ momentum thickness of the shear layer, defined as

$$\theta = \int_{-\infty}^{+\infty} \frac{\bar{U}_{(y)}}{\bar{U}_o} \left(1 - \frac{\bar{U}_{(y)}}{\bar{U}_o}\right) dy$$

ϕ potential function for the fluctuating velocities

ψ stream function for the fluctuating velocities

Φ complex potential function, defined as $\Phi = \phi + i\psi$

∇^2 Laplace operator in two dimensions, defined as

$\nabla^2 p = \frac{\partial^2 p}{\partial x^2} + \frac{\partial^2 p}{\partial y^2}$ for p, as an example

10.2. Appendix B

Discussion of the pressure sources

The source term in eq. (11), on the right hand side

$$(11) \qquad \nabla^2 p = -2\rho \frac{\partial \bar{U}}{\partial y} \cdot \frac{\partial v}{\partial x} = S$$

has apparently led to some confusion, in particular among those people, who have heard about aeroacoustic theory and know for sure, that there should be "some quadrupoles" [40]. We will not query Lighthill's theory, but the present approach is something different. We will have to deal with pressure sources; these are not sources of matter, which would be at variance with the continuity equation in our model (3).

To provide a better feeling for our pressure sources we will determine the pressure source structure of an instability wave in a free shear layer. This refers to the right hand side of eq. (11). Using a Fourier transform technique, we integrate eq. (11) to obtain the pressure distribution in the whole field, which could be obtained clearly also by other methods. Finally, we check our solution with the Euler equations.

We restrict ourselves to the "one stream" case where we have a fluid at rest above the shear layer and a flow of velocity $\bar{U}_o$ below the shear layer. We consider a normal spatially amplified instability wave where all fluctuations like p, v, u and the elevation h are proportional to $e^{\lambda x - i\omega t}$. In addition, we restrict ourselves to low Strouhal numbers (calculated with the shear layer thickness) where we have $\lambda = (i+1)\cdot\omega/\bar{U}_o$. It turns out to be most convenient to replace the v-velocity in eq. (11) by the displacement h. The displacement (as the pressure) has the same value at both sides of the shear layer and can be assumed to be constant throughout the shear layer at low Strouhal numbers. The relation between h and v is

$$(7) \qquad v = \frac{\partial h}{\partial t} + \bar{U}_{(y)} \frac{\partial h}{\partial x} .$$

Inserting this into eq. (11), we have

$$(B1) \qquad S = - \frac{2\rho\omega^2}{\bar{U}_o} \cdot \frac{d\bar{U}_{(y)}}{dy} h_{(x,y,t)} \left(1-i\left(1-2\,\frac{\bar{U}_{(y)}}{\bar{U}_o}\right)\right)$$

by writing h or $h_{(x,y,t)}$ we mean $h_{(y)} e^{\lambda x - i\omega t}$ throughout the calculations. It is assumed, that h is constant in the shear layer; it will vary, however, for greater distances $|y|$ from the shear layer, as we will see later.

A reasonable model for the shear layer velocity distribution is a hyperbolic tangent profile [6, 7]:

$$(B2) \qquad \bar{U}_{(y)} = \frac{\bar{U}_o}{2} (1-\tanh \varsigma y) ,$$

The quantity ς in this equation is related to the momentum thickness θ

$$(B3) \qquad \theta = \int_{-\infty}^{+\infty} \frac{\bar{U}_{(y)}}{\bar{U}_o} \left(1-\frac{\bar{U}_{(y)}}{\bar{U}_o}\right) dy$$

in the following way

(B4) $\zeta = 1/20$

Fig. 23 shows the distribution of $\bar{U}_{(y)}$.

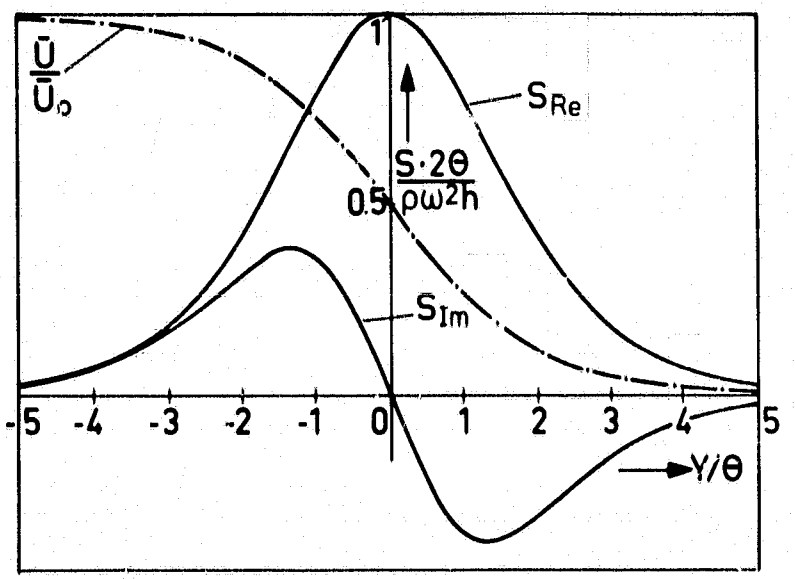

Fig. 23 Velocity distribution in the shear layer

Using eq. (B2) for the velocity distribution, we obtain the real and imaginary part of the pressure source distribution S

$$(B5) \qquad \left\{ \begin{array}{l} S_{Re} = \frac{\rho\omega^2 h}{20} \cdot \frac{1}{\cosh^2(y/20)} \\ S_{Im} = -\frac{\rho\omega^2 h}{20} \cdot \frac{\tanh(y/20)}{\cosh^2(y/20)} \end{array} \right\} .$$

The distributions in y-direction of these functions in the shear layer are displayed in Fig. 23.

As we see from Fig. 23, the real part of S has the near field structure of a δ-function; it exists only in a limited region which can shrink to zero if $\theta \to 0$. The actual value of the

δ function is determined by the surface under the $1/\cosh^2$-curve in Fig. 23.

$$(B6) \qquad \int_{-\infty}^{+\infty} \frac{dy}{\cosh^2 (y/20)} = 40.$$

Therefore, we can replace S_{Re} by a δ function representation for $\theta \to o$

$$(B7) \qquad S_{Re} = 2\rho\omega^2 h \ \delta_{(y)}.$$

The imaginary part has no contribution of a δ function type, and an integral like (B6) would give zero. Contributions of a δ'-type (dipole) are present, but this influence becomes negligible with $\theta \to o$. Therefore, the contribution of the imaginary part of S becomes zero. We are left with the nonhomogeneous partial differential equation

$$(B8) \qquad \nabla^2 p = 2\rho\omega^2 h \ \delta_{(y)}.$$

This equation will be solved by Fourier transformation. In fact, using h and p proportional to $e^{\lambda x - i\omega t}$, we have already taken a Fourier transformation in time (harmonic motion) and in the downstream direction x. To obtain a notation compatible with the usual form of Fourier transformations we replace λ by $i\nu$, where ν is the Fourier transform variable corresponding to the physical variable x. We have, therefore, instead of eq. (B8):

$$(B9) \qquad -\nu^2 p + \frac{\partial^2 p}{\partial y^2} = 2\rho\omega^2 h \ \delta_{(y)}.$$

We take the Fourier transform in y-direction; with

$$(B10) \qquad P_{(\eta)} = \int_{-\infty}^{+\infty} e^{i\eta y} \cdot p_{(y)} dy; \qquad p_{(y)} = \frac{1}{2\pi} \int_{-\infty}^{+\infty} e^{-i\eta y} \ P_{(\eta)} d\eta.$$

$$(B11) \qquad -\nu^2 P - \eta^2 P = 2\rho\omega^2 h$$

or

$$(B12) \qquad p = - \frac{2\rho\omega^2 h}{\nu^2+\eta^2}$$

where h is the displacement of the shear layer at y = o. The transformation back into the physical plane can be found in tables of Fourier transforms, like [39]

$$(B13) \qquad p = - \frac{\rho\omega^2 h}{\nu} e^{-\nu|y|},$$

For h we have

$$(B14) \qquad h_{(y=o)} = h_o \cdot e^{\lambda x} \quad \text{with } i\nu = \lambda = \frac{\omega}{\bar{U}_o}(i+1).$$

This can be inserted into (B13) and we find

$$(B15) \qquad \boxed{p_{(x,y)} = - \frac{(1+i)}{2} \cdot \rho\omega\bar{U}_o h_o \cdot e^{(\omega/\bar{U}_o)\cdot(i+1)\cdot(x+i|y|)}}$$

The last two terms can be interpreted as the spatial distribution $h_{(x,y)}$ of the displacement

$$(B16) \qquad h_{(x,y)} = h_o \cdot e^{(\omega/\bar{U}_o)\cdot(i+1)\cdot(x+i|y|)}$$

and we find the relation

$$(B17) \qquad \boxed{p_{(x,y)} = - \frac{(1+i)}{2} \rho\omega\bar{U}_o \cdot h_{(x,y)}}$$

We can check whether or not this relation is correct by using the Euler equations and the relation between v and h, i.e., eq. (7). For y > o, in the fluid at rest (index "1"), we have

$$(B18) \qquad v_1 = -i\omega h_{(x,y)}.$$

With the first Euler equation, we obtain

$$\frac{\partial p_1}{\partial y} = \rho\omega^2 h_{(x,y)} \cdot \tag{B19}$$

If we take the y-derivative of eq. (B15) we find, that this relation is fulfilled.

With that result, it is shown, that it is possible to analyze the pressure source distribution within a shear layer and integrate it (via Fourier transform techniques) to obtain the pressure distribution in the whole flow field. Thus, there is nothing mysterious left in our pressure source approach.

We have to mention what the difference between a pressure source (S) and a volume source (Q) is. A pressure source is a singularity in a field which is described outside the singularity by the Laplacean equation $\nabla^2 p = o$. A volume source is a singularity in an analogeous field with $\nabla^2 \phi = o$. In a fluid at rest, the relation between both fields is simple. From the first Eulerian equation we have $i\omega\rho\frac{\partial \phi}{\partial x} = \frac{\partial p}{\partial x}$, i.e., both fields are proportional. This is the reason why we have used potential theory and velocities like the excitation velocity v_{1f} in several sections of this paper instead of using pressures and pressure gradients. It would be more appropriate, however (and less obvious), to use pressure sources throughout the whole paper. The basic differences occur in the shear layer. Clearly it makes no sense to define a velocity potential inside the shear layer, whereas the pressure is still well defined there. In addition, the existence of pressure sources in the shear layer does not violate the continuity equation.

Some readers may be dissatisfied with the above methodic approach. Indeed, we have used a right hand side of eq. (11) which is known to fulfill all our equations. Instead of dealing with a formally nonhomogeneous equation we can also completely eliminate v and write eq. (11) only in terms of the pressure. This can be done

by using the second Euler equation. We end up with

$$(B20) \qquad (-i\omega + \bar{U}\frac{\partial}{\partial x})\nabla^2 p = 2\frac{\partial U}{\partial y}\cdot\frac{\partial^2 p}{\partial x \partial y}$$

outside the shear layer we have again $\nabla^2 p = o$. If we insert an instability wave ansatz $p \propto e^{i(\alpha x - \omega t)}$ we find

$$(B21) \qquad \frac{\partial^2 p}{\partial y^2} - \frac{2\frac{\partial \bar{U}}{\partial y}}{\bar{U} - \frac{\omega}{\alpha}}\cdot\frac{\partial p}{\partial y} - \alpha^2 p = o\,,$$

This is an equivalent to the Rayleigh equation for the instability of inviscid parallel flows, written in terms of the pressure. Outside the shear layer we have $p \propto e^{-\alpha|y|}$, as usual in the potential field of a wavy motion. The complete distribution of p can be found using a numerical procedure similar to the one used in stability theory [6]. This procedure would provide results valid for shear layers of finite thickness and would produce the whole pressure field for an instability wave, extended from $x = -\infty$ to $x = +\infty$. In fact, this latter approach provides a genuine and complete solution of the pressure field without knowing anything in advance, whereas the approach with a non-homogeneous pressure equation requires previous knowledge of the fluctuations in the shear layer.

10.3. Appendix C

The absence of "free" instability waves

In the main part of this paper, forced instability waves are calculated, which is equivalent to the assumption that the lower boundaries of the general solution of the instability waves

$$(23) \qquad v_1 = -\frac{\omega}{\bar{U}_o} e^{\lambda_1 x}\int_{G_1}^{x} e^{-\lambda_1 x} v_{1f}\,dx + \frac{\omega}{\bar{U}_o} e^{\lambda_2 x}\int_{G_2}^{x} e^{-\lambda_2 x} v_{1f}\,dx$$

should be $G_1 = G_2 = o$. This would also correspond to the non-

existence of additional "free" instability waves of the Helmholtz type. In a previous publication of the author [12], it had been mentioned, that additional instability waves of the Helmholtz type do not fulfill the boundary conditions, but no detailed proof had been given there. It is quite obvious, that a solution valid for a shear layer extended from $x = -\infty$ to $x = +\infty$ cannot be valid for a semi-infinite shear layer with a rigid boundary, such as a semi-infinite plate. The reader who is convinced by this simple and conclusive argument does not need to read the remainder of this section C of the appendix.

However, with all the present confusion about the Kutta condition issue the author feels that he cannot avoid providing a mathematical proof for the fact, that the Helmholtz solutions do not fulfill, in any conceivable combination, the boundary conditions. The absence of independent Helmholtz solutions leads to the conclusion, that only forced instability waves exist and that only the Kutta condition is possible. Of course, this latter statement on the Kutta condition is only valid for an infinitesimally thin shear layer, as assumed in our model. In reality, this would correspond to the case of low Strouhal number S_0. Any "rectification" effect (i.e., a steady deflection of the jet caused by the unsteady motion) as suggested by Orszag & Crow [9] could not be found in the experiments [41,42]. Such an effect would be also at variance with the equations of motion for a linearized problem. The linearization is well confirmed by the experiments [41, 42].

In the following calculations, we will restrict ourselves to the one-stream model of section 2. To prove that free instability waves (Helmholtz solutions) are not solutions of the present problem, we have to keep in mind that these solutions are truncated for $x < o$, because v has to be zero at the semi-infinite plate. The v distribution, therefore, assumes the following form:

$$(C1) \qquad v_1 = H_{(x)} \; (C_1 e^{\lambda 1 x} + C_2 e^{\lambda 2 x})$$

with $\lambda_{1,2} = \frac{\omega}{\bar{U}_o}(i \pm 1)$.

In this equation v_1 is the v-component of the fluctuating velocity just above the shear layer at $y = +o$; C_1 and C_2 are constants which may be complex and $H_{(x)}$ is the Haeviside unit step function which is zero for $x < o$ and unity for $x > o$. From equation (C1) we can calculate v_2, the v-velocity just below the shear layer, using equation (10), which represents the condition of equal displacement at both sides of the shear layer:

$$(10) \qquad v_2 = v_1 + i \frac{\bar{U}_o}{\omega} \frac{\partial v_1}{\partial x}$$

we obtain

$$(C2) \qquad v_2 = iH_{(x)} \left[C_1 e^{\lambda_1 x} - C_2 e^{\lambda_2 x}\right] + i\frac{\bar{U}_o}{\omega} \cdot \delta_{(x)} \cdot \left[C_1 + C_2\right].$$

The delta function $\delta_{(x)}$ is created by taking the derivative of the step function $H_{(x)}$. The physical significance of the $\delta_{(x)}$ function is that we need a source to create a finite displacement of the shear layer at $x = +o$ in the flow (at $y < o$ and with mean flow $\bar{U}_o$).

After having fulfilled the condition of equal displacement at both sides of the shear layer, we have to check whether or not the pressure is the same at both sides. Instead of taking the pressure, we can take as well $\partial p/\partial x$, the pressure gradient in the downstream direction. $\partial p/\partial x$ is related to the u-velocity component via the first Euler equation. We end up with eq. (6)

$$(6) \qquad u_2 + i\frac{\bar{U}_o}{\omega} \frac{\partial u_2}{\partial x} - u_1 = \frac{i}{\rho\omega} \frac{\partial(p_1 - p_2)}{\partial x}.$$

The right hand side should be zero for $x > o$. We have to calculate first the induced u-velocity for the decaying Helmholtz wave (exponent $\lambda_2 x$). In addition, we can omit the Haeviside step functions, if we change the boundaries of the integrals

$$(C3) \qquad u_{1\lambda_2} = \frac{C_2}{2\pi} \int_o^\infty \frac{e^{\lambda_2 \xi}}{z - \xi} d\xi + \frac{C_2}{2\pi} \int_o^\infty \frac{e^{\lambda_2 \xi}}{\bar{z} - \xi} d\xi .$$

It is understood, that the whole induced velocity u_1 will then consist of

$$(C4) \quad u_1 = u_{1\lambda_1} + u_{1\lambda_2} .$$

The integrals in eq. (C3) are of the structure of exponential integrals, defined as (see [31]):

$$(C5) \quad E_{1(z)} = \int_z^\infty \frac{e^{-t}}{t}\, dt .$$

After appropriate substitution of variables we obtain

$$(C6) \quad u_{1\lambda_2} = -\frac{C_2}{2\pi}\left[e^{\lambda_2 z} \cdot E_1(\lambda_2 z) + e^{\lambda_2 \bar{z}} \cdot E_1(\lambda_2 \bar{z})\right] .$$

This is the induced u-velocity for $y > o$ and for an instability wave decaying in the downstream direction. The situation is slightly more complex for an amplified instability wave (terms containing λ_1). By a straight forward integration we would enface divergence problems with the upper boundary of the integrals. This problem can be circumvented if we subtract from the complete instability wave solution (extended from $x = -\infty$ to $x = +\infty$) a contribution from $x = -\infty$ to $x = o$ to obtain $v_1 = o$ for $x < o$. The relation between u and v of the complete wave is (see eq. (68)) $u_1 = -iv_1$. Otherwise, the integration is very similar as that leading to eq. (C6). We obtain after some intermediate calculations

$$(C7) \quad u_{1\lambda_1} = -iC_1 e^{\lambda_1 x} - \frac{C_1}{2\pi}\left[e^{\lambda_1 z} \cdot E_1(\lambda_1 z) + e^{\lambda_1 \bar{z}} \cdot E_1(\lambda_1 \bar{z})\right] .$$

The complete solution for u_1 is then ($y > o$):

$$(C8) \quad u_1 = -iC_1 e^{\lambda_1 x} - \frac{C_1}{2\pi}\left[e^{\lambda_1 z} \cdot E_1(\lambda_1 z) + e^{\lambda_1 \bar{z}} \cdot E_1(\lambda_1 \bar{z})\right] -$$

$$- \frac{C_2}{2\pi}\left[e^{\lambda_2 z} \cdot E_1(\lambda_2 z) + e^{\lambda_2 \bar{z}} \cdot E_1(\lambda_2 \bar{z})\right]$$

for $y \to +o$.

It is understood, that y becomes +o to obtain the value of u_1 just above the shear layer. This transition to y = +o can be postponed, though, to a later stage of the calculations.

The procedure to obtain u_2 is very similar. However, for y < o the sign of u_2 changes. In addition, we have a contribution from a point source, represented by a δ function appearing in u_2. For negative y we have as the contribution from the source term

$$(C9) \qquad u_{2\delta} = -\frac{i\bar{U}_o}{\omega} \cdot \frac{(C_1+C_2)}{\pi} \int_{-\omega}^{+\omega} \frac{\delta(\xi)\cdot(x-\xi)}{(x-\xi)^2+y^2}\, d\xi \,.$$

For $y \to -o$ we obtain

$$(C10) \qquad u_{2\delta} = -\frac{i\bar{U}_o}{\pi\omega x} \quad (C_1+C_2) \,.$$

Obviously, the induced u-field of a source located on the x-axis should be proportional to 1/x. The complete solution for u_2 is then from eq. (C2)

$$(C11) \qquad u_2 = -C_1 e^{\lambda_1 x} + i\frac{C_1}{2\pi}\left[e^{\lambda_1 z}\cdot E_1(\lambda_1 z) + e^{\lambda_1 \bar{z}} \cdot E_1(\lambda_1 \bar{z})\right] -$$

$$- \frac{iC_2}{2\pi}\left[e^{\lambda_2 z} \cdot E_1(\lambda_2 z) + e^{\lambda_2 \bar{z}} \cdot E_1(\lambda_2 \bar{z})\right] - \frac{i\bar{U}_o}{\pi\omega x}(C_1+C_2)$$

for $y \to -o$.

u_1 and u_2 have to be inserted into equation (6) to find out whether or not the pressure equilibrium at both sides of the shear layer is fulfilled for x > o. To do this, we have to take the derivative of the exponential integral

$$(C12) \qquad \frac{dE_1(z)}{dz} = -\frac{e^{-z}}{z} \,.$$

Using this relation and, after taking the derivatives, letting $y \to o$, we obtain from equation (6) after some algebra

$$(C13) \qquad \frac{\bar{U}_o}{\pi\omega x}\left((C_1-C_2)-i(C_1+C_2)\right) - \frac{\bar{U}_o^2}{\pi\omega^2 x^2}(C_1+C_2) = \frac{i}{\rho\omega}\frac{d(p_1-p_2)}{dx} \,.$$

The right hand side should be zero for $x > o$. We see, that the right hand side can be zero for all positive x only if $C_1 = C_2 = o$.

This is the proof for the absence of "free" (unforced) instability waves, and it is, since the forced instability waves fulfill the Kutta condition at the plate edge, the proof for the existence of the Kutta condition there. Here, the Kutta condition is understood in that way, that the flow does not suffer a local jump in its slope when it passes the trailing edge of the plate.

10.4. Appendix D

v-computations at $y = \pm o$, tables

The purpose of this section is to provide numerical data for v_1 and v_2. This means, that the error function of a complex argument has to be computed. The present calculations are based on expansions given in [31]. One of the building blocks of our calculation is to provide an expansion for the function $e^{z^2}\,\mathrm{erf}\,z$ (where z is an arbitrary complex variable) and to split it subsequently into real and imaginary constituents. In the preceding calculations we used this expansion:

$$(D1)\qquad e^{z^2}\,\mathrm{erf}z = \frac{2}{\sqrt{\pi}} \sum_{n=o}^{\infty} \frac{2^n}{1\cdot 3\ldots(2n+1)} \cdot z^{2n+1} .$$

It provides, e.g., the near field behaviour near the plate end in a very elegant way. It was also used to produce the numerical values for v_1 between $\tilde{x} = o$ and $\tilde{x} = 2$ computed in [12]. Unfortunately, numerical convergence problems occur beyond $\tilde{x} \approx 3$ so that this series cannot be used up to those values of $\tilde{x}$ where the asymptotic expansion for large $\tilde{x}$ (say, $\tilde{x} > 6$)

$$(D2)\qquad \underset{(z \to \infty)}{e^{z^2}\,\mathrm{erf}z} = e^{z^2} - \frac{1}{z\sqrt{\pi}} \left(1 + \sum_{m=1}^{\infty} (-1)^m \frac{1\cdot 3\ldots(2m-1)}{(2z^2)^m}\right)$$

is valid. The series expansion in eq. (D2) is semi-konvergent. Therefore, it does not make sense to include, say, more than 6 terms of the series in our case.

For our numerical computations we had to use a more complicated expansion providing numerical convergence for low and middle values of the argument so that also the lower validity range of eq. (D2) (for large z) can be covered. This is based on eq. (7.1.29) in [31]. We introduce $z = R + iI$ and

$$(D3) \qquad A + iB = e^{z^2}\,\mathrm{erf}\,z = e^{(R+iI)^2}\,\mathrm{erf}(R+iI).$$

After splitting eq. (7.1.29) in [31] into real (A) and imaginary parts (B) we obtain after some algebra:

$$(D4) \qquad A = e^{R^2-I^2}\cdot\cos 2RI\cdot\mathrm{erf}\,R + \frac{e^{-I^2}}{2\pi R}(\cos 2RI - 1) + \frac{2e^{-I^2}}{\pi}\cdot\sum_{n=1}^{\infty}\frac{e^{-\frac{n^2}{4}}}{n^2+4R^2}(2R\cos 2RI - 2R\cosh nI)$$

$$(D5) \qquad B = e^{R^2-I^2}\cdot\sin 2RI\cdot\mathrm{erf}\,R + \frac{e^{-I^2}}{2\pi R}\cdot\sin 2RI + \frac{2e^{-I^2}}{\pi}\sum_{n=1}^{\infty}\frac{e^{-\frac{n^2}{4}}}{n^2+4R^2}(2R\sin 2RI + n\sinh nI).$$

For the numerical representation of the error function of a real argument we use an approximation suggested by Hastings [31, eq. (7.1.28)]:

$$(D6) \qquad \mathrm{erf}\,R = 1 - \frac{1}{[1+a_1R+a_2R^2+\ldots+a_6R^6]^{16}}$$

with the constants a_n:

$$a_1 = 0.0705230784 \qquad a_2 = 0.0422820123$$
$$a_3 = 0.0092705272 \qquad a_4 = 0.0001520143$$
$$a_5 = 0.0002765672 \qquad a_6 = 0.0000430638\ .$$

The error of this approximation should be smaller than $3\cdot10^{-7}$ over the whole range.

With equations (D2) and (D4), (D5) we can now write the computer subroutines for the building block "e^{z^2} erf z" which is the essential part for the v_1 and v_2 computations. When we will show some computer programs here, it is done without showing all details of the considerations leading to these programs. The programs shown here are written in BASIC for the sharp PC 1211 Microcomputer*) (see Fig. 24). These programs are only provided in order to keep the mathematics verifyable. In addition, it is shown, that the present numerical solutions are not dependent on the access to big, fast and expensive computers.

In the subroutines, which are given below, R and I are, as in eq. (D3), the real and imaginary part of the variable z, and A & B have also the same meaning as in eq. (D3). For equation (D4), (D5) we have the subroutine "SUBR 1" and for equation (D2) we have "SUBR 2". With these subroutines we have to calculate v_1 and v_2 from eq. (44) and (45)

$$(44) \qquad \tilde{v}_1 = \frac{i\sqrt{\pi}}{4}\left[\frac{e^{\tilde{\lambda}_1\tilde{x}}}{\sqrt{\tilde{\lambda}_1}}\,\mathrm{erf}\sqrt{\tilde{\lambda}_1\tilde{x}} - \frac{e^{\tilde{\lambda}_2\tilde{x}}}{\sqrt{\tilde{\lambda}_2}}\,\mathrm{erf}\,\sqrt{\tilde{\lambda}_2\tilde{x}}\right]$$

$$(45) \qquad \tilde{v}_1 = -\frac{\sqrt{\pi}}{4}\left[\frac{e^{\tilde{\lambda}_1\tilde{x}}}{\sqrt{\tilde{\lambda}_1}}\,\mathrm{erf}\,\sqrt{\tilde{\lambda}_1\tilde{x}} + \frac{e^{\tilde{\lambda}_2\tilde{x}}}{\sqrt{\tilde{\lambda}_2}}\,\mathrm{erf}\,\sqrt{\tilde{\lambda}_2\tilde{x}}\right]$$

with $\tilde{\lambda}_1 = i+1$ and $\tilde{\lambda}_2 = i-1$.

One point is worth mentioning concerning the algebra of complex numbers. If we take the root of a quantity like

$$(D7) \qquad i+1 = \sqrt{2}\,e^{i\frac{\pi}{4}} \;;\; i-1 = \sqrt{2}\,e^{i\frac{3\pi}{4}}.$$

*) sold as "TRS80 Microcomputer" by Radio Shack in the U.S.. This is not a commercial for microcomputers. Indeed, the memory and speed of this computer are not very satisfactory. In the meantime, however, more powerful microcomputers are available.

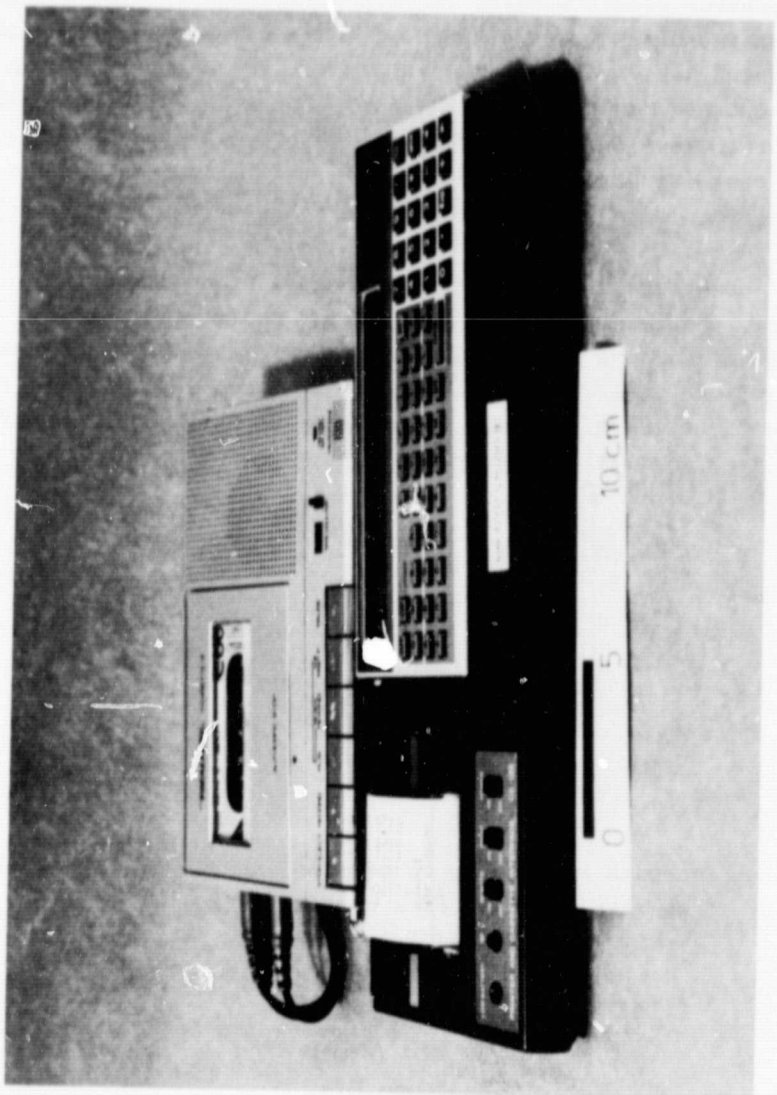

Fig. 24 Sharp PC 1211 microcomputer with printer/cassette interface and cassette recorder.

Program listing of the subroutines

"SUBR 1"

```
101:"SUBR1"
102:A(27)=.07052
    30784
103:A(28)=.04228
    20123
104:A(29)=.00927
    05572
105:A(30)=.00015
    20143
106:A(31)=.00027
    65672
107:A(32)=.00004
    30638
108:E=(1+A(27)*R
    +A(28)*R*R+A
    (29)*(R^3)+A
    (30)*(R^4)+A
    (31)*(R^5)+A
    (32)*(R^6))^
    -16
109:E=1-E
110:N=1:H=0:K=0
111:S=SIN 2IR:C=
    COS 2IR
112:T=4RR:L=2RC:
    M=2R^2
113:N=EXP (NI):D
    =NN
114:Z=(D+T)*EXP
    (D*4)
115:P=L-P*(N+1
    N)*2
116:Q=(M*.5*N+N
    -1 N)*2
117:H=H+P:K=K+Q:
    N=N+1
118:IF ABS P*1E-
    4<0TO 113
119:IF ABS Q*1E-
    4<0TO 113
120:T=EXP (-II):
    L=EXP (RR):M
    =2RE
121:A=T*(LCE+(C-
    1*M+2H N)
122:I=T*(LSE+S*M
    +2I N)
123:RETURN
```

"SUBR 2"

```
201:"SUBR2"
202:D=KK+1I:D=
    ATN (I R)
203:IF R<0GOTO 2
    06
204:IF I OLET D=
    D+E
205:IF I<0LET D=
    D-E
206:M=1:P=1:I=0:
    L=0
207:P=P*(.5-M)/(
    I*(2M+1))*D
208:F=F+COS N
209:G=P*SIN N
210:L=L+F:L=L+G:
    M=M+1
211:IF M<7GOTO 2
    07
212:M=EXP (RR-II
    ):T=0*ZI:H=Z
    (ZI)
213:A=M*COS 2RI-
    R T-I H
214:B=M*SIN 2RI+
    I T+L H
215:RETURN
```

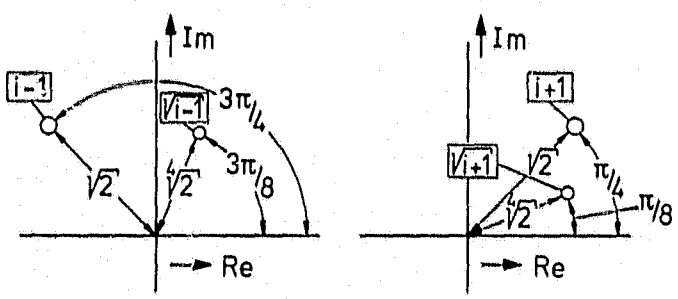

Fig. 25 roots of complex numbers.

we take only the first of two possible roots (see Fig. 25)

$$\sqrt{1+i} = \sqrt[4]{2}\, e^{i\frac{\pi}{8}} = \sqrt[4]{2}\quad (\cos \pi/8 + i \sin \pi/8)$$

(D8) $$\sqrt{1-i} = \sqrt[4]{2}\, e^{i\frac{3\pi}{8}} = \sqrt[4]{2}\quad (\cos 3\pi/8 + i \sin 3\pi/8) =$$

$$= \sqrt[4]{2}\ (\sin\pi/8 + i \cos \pi/8)$$

we proceed in the same way with the quantity $\tilde{x}\tilde{\lambda}_{1,2}$.

With these relations and the subroutines, the evaluation of eqs. (44) and (45) is a straightforward procedure. We end up with the real and imaginary parts of v_1, i.e., V_{1R} and v_{1I} and with similar quantities for v_2, i.e., v_{2R} and v_{2I}.

In addition to that, the computer calculates also the difference between v and its asymptotic form, the amplified Helmholtz instability wave

(D9) $$\tilde{v}_{1D} = \tilde{v}_1 - \tilde{v}_{1H};\ \tilde{v}_{2D} = \tilde{v}_2 - \tilde{v}_{2H}$$

with

$$\tilde{v}_{1H} = \frac{i\sqrt{\pi}}{4} \cdot \frac{e^{\tilde{\lambda}_1\tilde{x}}}{\sqrt{\tilde{\lambda}_1}};\ \tilde{v}_{2H} = -\frac{\sqrt{\pi}}{4} \cdot \frac{e^{\tilde{\lambda}_1\tilde{x}}}{\sqrt{\tilde{\lambda}_1}}\ .$$

As before, we will calculate the real and imaginary parts also of the quantities in eq. (D9), i.e., v_{1DR} & v_{1DI} as well as v_{2DR} & v_{2DI}.

Finally, the program calculates the modulus of v_{1H}, which is equal to $|v_{2H}|$ and the modulus of v_1 and v_2, respectively. Since the memory of the microcomputer is quite limited, the mean program to calculate all those quantities cannot contain both subroutines. We have two programs, "v-PRO 1" with the subroutine "SUBR 1" for small and middle values of $\tilde{x}$ and a second, almost identical program "v-PRO 2" with the subroutine "SUBR 2" for large values of $\tilde{x}$. It is suggested to switch from "v-PRO 1" to "v-PRO 2" at values of $\tilde{x}$ between 5 and 8. It has been checked, that also the series expansion (D1) produces overlapping values for the velocities up to $\tilde{x} = 2 \div 3$. The operation of the programs starts with the computer asking for

(i) the initial values of x ("x-START?")

(ii) the stepwidth Δx for the consecutive calculation of a series of x values ("SCHRITT?")

(iii) the final value of x of the data set ("x-ENDE?")

The programs "v-PRO 1" and "v-PRO 2" are listed on the next pages.

There is another version of these programs which provides data on casette tape for further use of the following programs calculating u_2 (Appendix E). Since only v_{2DR} and v_{2DI} are the necessary quantities to be supplied for these further u-programs, the v-program is much shorter, so that both subroutines for small and middle x and for large x can be comprised in the program. Each data set stored on the data tape consists of 4 words, i.e.

1) the label "v_{2D}"
2) the value of $\tilde{x}$
3) the value of v_{2DR}
4) the value of v_{2DI}

Program listing
"v-PRO 1"

```
 1:"V-PRO1"
 2:INPUT "X-STA
   RT?";A(45),"
   SCHRITT?";A(
   46),"X-ENDE?
   ";A(47)
 3:X=A(45)
 9:IF X>0GOTO 1
   1
10:A(37)=0:A(38
   )=0:A(39)=0:
   A(40)=0:GOTO
   27
11:0=√(X*√2):U=
   COS (π/8):V=
   SIN (π/8)
12:R=0U:I=0V
13:GOSUB 101
15:A(33)=AU+BV
16:A(34)=-AV+BU
17:R=0V:I=0U
18:GOSUB 101
20:A(35)=AV+BU
21:A(36)=-AU+BV
22:Y=-(√π)/(4*√
   (√2))
23:A(37)=Y*(A(3
   3)+A(35))
24:A(38)=Y*(A(3
   4)+A(36))
25:A(39)=Y*(A(3
   4)-A(36))
26:A(40)=Y*(-A(
   33)+A(35))
27:Y=-(√π)*(EXP
   X)/(4*√(√2))
28:A(41)=A(37)-
   Y*COS (X-(π/
   8))
29:A(42)=A(38)-
   Y*SIN (X-(π/
   8))
30:A(43)=A(39)+
   Y*COS (X+(3π
   /8))
31:A(44)=A(40)+
   Y*SIN (X+(3π
   /8))
32:PRINT "X=":
   PRINT X
33:PRINT "V2R="
   :PRINT A(37)
34:PRINT "V2I="
   :PRINT A(38)
35:PRINT "V1R="
   :PRINT A(39)
36:PRINT "V1I="
   :PRINT A(40)
37:PRINT "V2DR=
   ":PRINT A(41
   )
38:PRINT "V2DI=
   ":PRINT A(42
   )
39:PRINT "V1DR=
   ":PRINT A(43
   )
40:PRINT "V1DI=
   ":PRINT A(44
   )
41:PRINT "ABS(V
   2H=V1H)=":
   PRINT -Y
42:PRINT "ABS(V
   2)=":PRINT √
   (A(37)*A(37)
   +A(38)*A(38)
   )
43:PRINT "ABS(V
   1)=":PRINT √
   (A(39)*A(39)
   +A(40)*A(40)
   )
44:X=X+A(46):IF
   X<=A(47)GOTO
   9
45:END
101:"SUBR1"
102:A(27)=.07052
   30784
103:A(28)=.04228
   20123
104:A(29)=.00927
   05272
105:A(30)=.00015
   20143
106:A(31)=.00027
   65672
107:A(32)=.00004
   30638
108:E=(1+A(27)*R
   +A(28)*R*R+A
   (29)*(R^3)+A
   (30)*(R^4)+A
   (31)*(R^5)+A
   (32)*(R^6))^
   -16
109:E=1-E
110:N=1:H=0:K=0
111:S=SIN 2IR:C=
   COS 2IR
112:T=4RR:L=2RC:
   M=2RS
113:W=EXP (NI):D
   =NN
114:Z=(D+T)*EXP
   (D/4)
115:P=(L-R*(W+1/
   W))/Z
116:Q=(M+.5*N*(W
   -1/W))/Z
117:H=H+P:K=K+Q:
   N=N+1
118:IF ABS P>1E-
   4GOTO 113
119:IF ABS Q>1E-
   4GOTO 113
120:T=EXP (-II):
   L=EXP (RR):M
   =2πR
121:A=T*(LCE+(C-
   1)/N+2H/π)
122:B=T*(LSE+S/N
   +2K-π)
123:RETURN
```

Program listing
"v-PRO 2"

```
 1:"V-PRO2"
 2:INPUT "X-START?",A(45),"SCHRITT?",A(46),"X-ENDE?",A(47)
 3:X=A(45)
 9:IF X>0GOTO 11
10:A(37)=0:A(38)=0:A(39)=0:A(40)=0:GOTO 27
11:0=√(X*√2):U=COS (π/8):V=SIN (π/8)
12:R=0U:I=0V
14:GOSUB 201
15:A(33)=AU+BV
16:A(34)=-AV+BU
17:R=0V:I=0U
19:GOSUB 201
20:A(35)=AV+BU
21:A(36)=-AU+BV
22:Y=-(√π)/(4*√(√2))
23:A(37)=Y*(A(33)+A(35))
24:A(38)=Y*(A(34)+A(36))
25:A(39)=Y*(A(34)-A(36))
26:A(40)=Y*(-A(33)+A(35))
27:Y=-(√π)*(EXP X)/(4*√(√2))
28:A(41)=A(37)-Y*COS (X-(π/8))
29:A(42)=A(38)-Y*SIN (X-(π/8))
30:A(43)=A(39)+Y*COS (X+(3π/8))
31:A(44)=A(40)+Y*SIN (X+(3π/8))
32:PRINT "X=":PRINT X
33:PRINT "V2R=":PRINT A(37)
34:PRINT "V2I=":PRINT A(38)
35:PRINT "V1R=":PRINT A(39)
36:PRINT "V1I=":PRINT A(40)
37:PRINT "V2DR=":PRINT A(41)
38:PRINT "V2DI=":PRINT A(42)
39:PRINT "V1DR=":PRINT A(43)
40:PRINT "V1DI=":PRINT A(44)
41:PRINT "ABS(V2H=V1H)=":PRINT -Y
42:PRINT "ABS(V2)=":PRINT √(A(37)*A(37)+A(38)*A(38))
43:PRINT "ABS(V1)=":PRINT √(A(39)*A(39)+A(40)*A(40))
44:X=X+A(46):IF X<=A(47)GOTO 9
45:END
201:"SUBR2"
202:Q=RR+II:D=ATN (I/R)
203:IF R>0GOTO 206
204:IF I>0LET D=D+π
205:IF I<0LET D=D-π
206:M=1:P=1:K=0:L=0
207:P=P*(.5-M)/Q:N=(2M+1)*D
208:F=P*COS N
209:G=P*SIN N
210:K=K+F:L=L+G:M=M+1
211:IF MK7GOTO 207
212:M=EXP (RR-II):T=Q*√π:H=√(πQ)
213:A=M*COS 2RI-R/T-K/H
214:B=M*SIN 2RI+I/T+L/H
215:RETURN
```

Besides that output feature, the "tape output version "v_{2D}-PRO" is identical to v-PRO 1 + v-PRO 2; the switching from the expansion for small and middle $\tilde{x}$ (SUBR 1) to large $\tilde{x}$ (SUBR 2) takes place at $\tilde{x} = 6$. Finally, we provide in Table 2 a data survey for the different v-velocity constituents.

ORIGINAL PAGE IS
OF POOR QUALITY

Program listing
"V_{2D}-PRO"

```
1:"V2D-PRO"
2:INPUT "X-START?",A(27),"SCHRITT?",A(28),"X-ENDE?",A(29)
3:X=A(27)
9:IF X>0GOTO 11
10:A(30)=0:A(31)=0:A(32)=0:A(33)=0:GOTO 27
11:Q=√(X+√2):U=COS (π/8):V=SIN (π/8)
12:R=QU:I=QV
13:IF X<6GOSUB 101
14:IF X>=6GOSUB 201
15:A(34)=AU+BV
16:A(35)=-AV+BU
17:R=QV:I=QU
18:IF X<6GOSUB 101
19:IF X>=6GOSUB 201
20:A(36)=AV+BU
21:A(37)=-AU+BV
22:Y=-(√π)/(4+√(√2))
23:A(30)=Y*(A(34)+A(36))
24:A(31)=Y*(A(35)+A(37))
25:A(32)=Y*(A(35)-A(37))
26:A(33)=Y*(-A(34)+A(36))
27:Y=-(√π)*(EXP X)/(4+√(√2))
30:A(56)=A(30)-Y*COS (X-(π/8))
31:A(57)=A(31)-Y*SIN (X-(π/8))
32:A(55)=X
33:PRINT #"V2D",A(55)
44:X=X+A(28):IF X<=A(29)GOTO 9
45:END
101:"SUBR1"
102:K=.070523078 4
103:L=.042282012 3
104:M=.009270527 2
105:N=.000152014 3
106:P=.000276567 2
107:Q=.000043063 8
108:E=(1+KR+LRR+M*(R^3)+N*(R^4)+P*(R^5)+Q*(R^6))^-16
109:E=1-E
110:N=1:H=0:K=0
111:S=SIN 2R:C=COS 2R
112:T=4RR:L=2RC:M=2RS
113:W=EXP (NI):D=NN
114:Z=(D+T)*EXP (D/4)
115:P=(L-R*(N+1/N))/2
116:Q=(M+.5+N*(W+1/W))/2
117:H=H+P:K=K+Q:N=N+1
118:IF ABS P>1E-4GOTO 113
119:IF ABS Q>1E-4GOTO 113
120:T=EXP (-II):L=EXP (RR):M=2ΠR
121:A=T*(LCE+(C-1)*N+2H/π)
122:B=T*(LSE+S/M+2K/π)
123:RETURN
201:"SUBR2"
202:Q=RR+II:D=ATN (I/R)
203:IF R>0GOTO 206
204:IF I>0LET D=D+π
205:IF I<0LET D=D-π
206:N=1:P=1:K=0:L=0
207:P=P+(.5-M)/Q:N=(2M+1)*D
208:F=P+COS N
209:G=P+SIN N
210:K=K+F:L=L+G:M=M+1
211:IF M<7GOTO 207
212:M=EXP (RR-II):T=Q+√π:H=√(πQ)
213:A=M*COS 2RI-R/T-K/H
214:B=M*SIN 2RI+I/T+L/H
215:RETURN
```

$\tilde{x}$	-4	-3.8	-3.6	-3.4	-3.2	-3.0	-2.8	-2.6	-2.4	-2.2	-2.0	-1.8	-1.6
$\tilde{v}_{1R}$	o	o	o	o	o	o	o	o	o	o	o	o	o
$\tilde{v}_{1I}$	o	o	o	o	o	o	o	o	o	o	o	o	o
$\tilde{v}_{2R}$	o	o	o	o	o	o	o	o	o	o	o	o	o
$\tilde{v}_{2I}$	o	o	o	o	o	o	o	o	o	o	o	o	o
$\tilde{v}_{1DR}$	0.0065	0.0072	0.0077	0.0075	0.0066	0.0046	0.0012	-0.0041	-0.0116	-0.0215	-0.0343	-0.0501	-0.0686
$\tilde{v}_{1DI}$	0.0021	0.0041	0.0067	0.0099	0.0137	0.0180	0.0226	0.0274	0.0318	0.0352	0.0369	0.0359	0.0308
$\tilde{v}_{2DR}$	-0.0021	-0.0041	-0.0067	-0.0099	-0.0137	-0.0180	-0.0226	-0.0274	-0.0318	-0.0352	-0.0369	-0.0359	-0.0308
$\tilde{v}_{2DI}$	0.0065	0.0072	0.0077	0.0075	0.0066	0.0046	0.0012	-0.0041	-0.0116	-0.0215	-0.0343	-0.0501	-0.0686
$\lvert\tilde{v}_{1H}\rvert = \lvert\tilde{v}_{2H}\rvert$	0.0068	0.0083	0.0102	0.0124	0.0152	0.0186	0.0227	0.0277	0.0338	0.0413	0.0504	0.0616	0.0752
$\lvert\tilde{v}_1\rvert$	o	o	o	o	o	o	o	o	o	o	o	o	o
$\lvert\tilde{v}_2\rvert$	o	o	o	o	o	o	o	o	o	o	o	o	o

Table 2 v-velocity constituents.

$\bar{x}$	-1.4	-1.2	-1.0	-0.8	-0.6	-0.4	-0.2	o	0.2	0.4	0.6	0.8	1.0
$\tilde{v}_{1R}$	o	o	o	o	o	o	o	o	-0.0095	-0.0540	-0.1486	-0.3044	-0.5295
$\tilde{v}_{1I}$	o	o	o	o	o	o	o	o	0.0591	0.1624	0.2836	0.4037	0.5025
$\tilde{v}_{2R}$	o	o	o	o	o	o	o	o	-0.4472	-0.6314	-0.7678	-0.8696	-0.9324
$\tilde{v}_{2I}$	o	o	o	o	o	o	o	o	-0.0602	-0.1747	-0.3346	-0.5431	-0.8062
$\tilde{v}_{1DR}$	-0.0896	-0.1122	-0.1349	-0.1556	-0.1713	-0.1779	-0.1704	-0.1426	-0.0967	-0.0499	-0.0088	0.0241	0.0484
$\tilde{v}_{1DI}$	0.0202	0.0025	-0.0243	-0.0618	-0.1117	-0.1753	-0.2530	-0.3442	-0.3876	-0.3934	-0.3808	-0.3577	-0.3293
$\tilde{v}_{2DR}$	-0.202	-0.0025	0.0243	0.0618	0.1117	0.1753	0.2530	0.3442	-0.0005	-0.0755	-0.1034	-0.1082	-0.1006
$\tilde{v}_{2DI}$	-0.0896	-0.1122	-0.1349	-0.1556	-0.1713	-0.1779	-0.1704	-0.1426	-0.1473	-0.1707	-0.1948	-0.2146	-0.2282
$\lvert\tilde{v}_{1H}\rvert = \lvert\tilde{v}_{2H}\rvert$	0.0919	0.1122	0.1371	0.1674	0.2045	0.2498	0.3051	0.3726	0.4551	0.5559	0.6789	0.8293	1.0129
$\lvert\tilde{v}_1\rvert$	o	o	o	o	o	o	o	o	0.0598	0.1711	0.3202	0.5056	0.7300
$\lvert\tilde{v}_2\rvert$	o	o	o	o	o	o	o	o	0.4512	0.6551	0.8375	1.0253	1.2326

Table 2 v-velocity constituents (contd.).

$\tilde{x}$	1.2	1.4	1.6	1.8	2.0	2.2	2.4	2.6	2.8	3.0	3.2	3.4	3.6
$\tilde{v}_{1R}$	-0.8289	-1.2032	-1.6470	-2.1466	-2.6775	-3.2009	-3.6607	-3.9801	-4.0587	-3.7708	-2.9650	-1.4661	0.9196
$\tilde{v}_{1I}$	0.5564	0.5378	0.4146	0.1501	-0.2957	-0.9651	-1.8987	-3.1321	-4.6891	-6.5743	-8.7627	-11.1877	-13.7275
$\tilde{v}_{2R}$	-0.9422	-0.8774	-0.7099	-0.4053	0.0754	0.7738	1.7309	2.9827	4.5536	6.4490	8.6445	11.0744	13.6172
$\tilde{v}_{2I}$	-1.1293	-1.5147	-1.9594	-2.4521	-2.9705	-3.4780	-3.9199	-4.2209	-4.2816	-3.9769	-3.1557	-1.6431	0.7544
$\tilde{v}_{1DR}$	0.0648	0.07422	0.0780	0.07751	0.07391	0.0683	0.0615	0.0543	0.0471	0.0403	0.0342	0.0288	0.0242
$\tilde{v}_{1DI}$	-0.2990	-0.2693	-0.2416	-0.2168	-0.1953	-0.1771	-0.1622	-0.1502	-0.1407	-0.1333	-0.1276	-0.1233	-0.1200
$\tilde{v}_{2DR}$	-0.0868	-0.0703	-0.0538	-0.0384	-0.0251	-0.0141	-0.0056	0.0008	0.0052	0.0080	0.0094	0.0099	0.0097
$\tilde{v}_{2DI}$	-0.2356	-0.2373	-0.2344	-0.2280	-0.2191	-0.2088	-0.1977	-0.1866	-0.1758	-0.1657	-0.1565	-0.1483	-0.1410
$\lvert\tilde{v}_{1H}\rvert = \lvert\tilde{v}_{2H}\rvert$	1.2371	1.5110	1.8455	2.2541	2.7532	3.3628	4.1074	5.0168	6.1275	7.4841	9.1411	11.1650	13.6370
$\lvert\tilde{v}_1\rvert$	0.9983	1.3179	1.6983	2.1518	2.6938	3.3432	4.1238	5.0647	6.2017	7.5790	9.2507	11.2834	13.7583
$\lvert\tilde{v}_2\rvert$	1.4707	1.7505	2.0840	2.4854	2.9715	3.5630	4.2851	5.1684	6.2504	7.5766	9.2025	11.1956	13.6381

Table 2 v-velocity constituents (contd.).

$\tilde{x}$	3.8	4.0	4.2	4.4	4.6	4.8	5.0	5.2	5.4	5.6	5.8	6.0	6.2
$\tilde{v}_{1R}$	4.394	9.153	15.361	23.126	32.452	43.196	55.005	67.249	78.945	88.682	94.542	94.05	84.12
$\tilde{v}_{1I}$	-16.189	-18.293	-19.656	-19.782	-18.048	-13.709	-5.909	6.294	23.873	47.755	78.704	117.17	163.10
$\tilde{v}_{2R}$	16.081	18.185	19.549	19.675	17.942	13.604	5.803	-6.399	-23.977	-47.857	-78.806	-117.27	-163.20
$\tilde{v}_{2I}$	4.239	9.006	15.222	22.992	32.323	43.071	54.884	67.131	78.830	88.568	94.430	94.94	84.01
$\tilde{v}_{1DR}$	0.0204	0.0173	0.0148	0.0128	0.0114	0.0102	0.0094	0.0088	0.0083	0.0080	0.0077	0.0075	0.0073
$\tilde{v}_{1DI}$	-0.1174	-0.1153	-0.1136	-0.1121	-0.1107	-0.1094	-0.1080	-0.1067	-0.1053	-0.1039	-0.1025	-0.1010	-0.0996
$\tilde{v}_{2DR}$	0.0090	0.0080	0.0068	0.0057	0.0046	0.0036	0.0027	0.0020	0.0014	0.0009	0.0006	0.0003	0.0002
$\tilde{v}_{2DI}$	-0.1347	-0.1292	-0.1246	-0.1206	-0.1171	-0.1142	-0.1116	-0.1093	-0.1073	-0.1054	-0.1037	-0.1021	-0.1005
$\lvert\tilde{v}_{1H}\rvert = \lvert\tilde{v}_{2H}\rvert$	16.656	20.344	24.848	30.350	37.069	45.276	55.301	67.544	82.499	100.76	123.07	150.32	183.60
$\lvert\tilde{v}_1\rvert$	16.775	20.455	24.947	30.432	37.133	45.319	55.321	67.543	82.476	100.72	123.01	150.25	183.52
$\lvert\tilde{v}_2\rvert$	16.630	20.293	24.777	30.262	36.969	45.168	55.190	67.435	82.396	100.67	122.99	150.26	183.56

Table 2 v-velocity constituents (contd.).

$\tilde{x}$	6.4	6.6	6.8	7.0	7.2	7.4	7.6	7.8	8.0	8.2	8.4	8.6	8.8
$\tilde{v}_{1R}$	61.09	20.77	-41.41	-130.13	-249.76	-403.83	-594.21	-820.17	-1077.1	-1355.2	-1637.6	-1898.9	-2103.1
$\tilde{v}_{1I}$	215.68	273.02	331.88	387.25	432.00	456.34	448.53	392.75	271.14	63.22	-252.15	-700.4	-1299.2
$\tilde{v}_{2R}$	-215.77	-273.12	-331.98	-387.34	-432.09	-456.63	-448.62	-392.84	-271.23	-63.31	253.06	700.3	1299.1
$\tilde{v}_{2I}$	60.99	20.67	-41.51	-130.23	-249.86	-403.93	-594.31	-820.26	-1077.2	-1355.3	-1637.7	-1899.0	-2103.2
$\tilde{v}_{1DR}$	0.0071	0.0069	0.0067	0.0066	0.0064	0.0062	0.0060	0.0058	0.0056	0.0054	0.0052	0.0050	0.0048
$\tilde{v}_{1DI}$	-0.0982	-0.0967	-0.0954	-0.0940	-0.0927	-0.0915	-0.0902	-0.0891	-0.0880	-0.0869	-0.0858	-0.0848	-0.0839
$\tilde{v}_{2DR}$	0.00005	-0.00001	-0.00004	-0.00005	-0.00003	-0.00001	0.00001	0.00003	0.00006	0.00007	0.00009	0.0001	0.0001
$\tilde{v}_{2DI}$	-0.0991	-0.0977	-0.0963	-0.0950	-0.0937	-0.0925	-0.0912	-0.0901	-0.0889	-0.0878	-0.0868	-0.0857	-0.0847
$\tilde{v}_{1R} = \tilde{v}_{2I}$	224.25	273.91	334.55	408.62	499.09	609.59	744.55	909.40	1110.7	1356.6	1657.0	2023.9	2472.0
$\tilde{v}_1$	224.16	273.81	334.45	408.53	499.01	609.52	744.49	909.36	1110.7	1356.7	1657.0	2023.9	2472.0
$\tilde{v}_2$	224.23	273.90	334.56	408.65	499.14	609.65	744.63	909.48	1110.8	1356.8	1657.1	2024.0	2472.1

Table 2 v-velocity constituents (contd.).

$\tilde{x}$	9.0	9.2	9.4	9.6	9.8	10.0
$\tilde{v}_{1R}$	-2202.3	-2135.2	-1826.3	-1187.0	-117.4	1489.7
$\tilde{v}_{1I}$	-2065.5	-3006.9	-4117.5	-5372.0	-6718.7	-8071.1
$\tilde{v}_{2R}$	2065.4	3006.8	4117.4	5372.0	6718.6	8071.0
$\tilde{v}_{2I}$	-2202.4	-2135.2	-1826.4	-1187.1	-117.5	1489.6
$\tilde{v}_{1DR}$	0.0047	0.0045	0.0044	0.0042	0.0041	0.0040
$\tilde{v}_{1DI}$	-0.0829	-0.0820	-0.0812	-0.0803	-0.0795	-0.0787
$\tilde{v}_{2DR}$	0.0001	0.0001	0.0001	0.0001	0.00009	0.00004
$\tilde{v}_{2DI}$	-0.0837	-0.0828	-0.0819	-0.0810	-0.0802	-0.0793
$\lvert\tilde{v}_{1H}\rvert = \lvert\tilde{v}_{2H}\rvert$	3019.3	3687.8	4504.3	5501.5	6719.6	8207.3
$\lvert\tilde{v}_1\rvert$	3019.4	3687.9	4504.4	5501.6	6719.7	8207.4
$\lvert\tilde{v}_2\rvert$	3019.4	3687.8	4504.3	5501.6	6719.6	8207.3

Table 2 v-velocity constituents (contd.).

10.5. Appendix E

u-computations at y < o, tables

The basic ideas of the u_2 field computations have already been outlined in section 3. The calculation proceeds as follows (see Fig. 26)

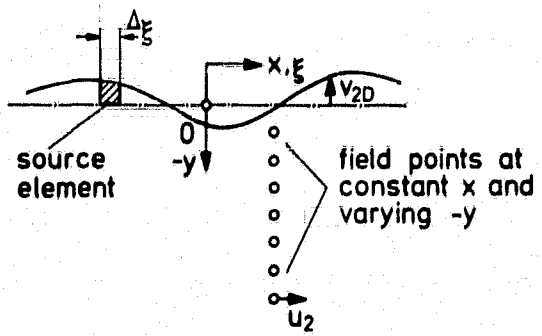

Fig. 26 Field computation scheme.

We calculate the velocity u_{2D}, induced by the v_{2D} velocity distribution. u_{2D} is computed for a set of, say, 15 field points with varying -y and at a constant x location. We are summarizing the induced velocities from each (source distribution) interval $\Delta\xi$. We start the computation at sufficiently large negative values of ξ to have a sufficiently low value of v_{2D}. We use an integration procedure utilizing trapezoidal (source) elements between, say, $\xi = -6$ and $\xi = o$. For the real part of v_{2D}, which has an infinite slope at $\xi = c$ (see Fig. 6 in section 2), we use for the v_{2R} contribution to v_{2DR} a parabolic piece of curve between $\xi = o$ and $\xi = o.1$. For this region we use the analytic solution eq. (82). For the region between $\xi = o.1$ (or $\xi = o$ for the imaginary part) and $\xi = 6$, we use again the trapezoidal element model. The stepwidth for our calculation is $\Delta\xi = o.1$. Above $\xi = 6$, the real part is set equal to zero (no contribution above $\xi = 6$) and the imaginary part, which has a $-1/4\sqrt{\xi}$ behaviour, is evaluated with the analytical far field solution, eq. (79). The

computation of u_{2DR} and u_{2DI} is done simultaneously. The values of v_{2D} for $\xi \cdot 0$ are computed by the u_2-program, because it consists just of the (negative) Helmholtz solution. For values between $\xi = 0$ and $\xi = 6$ the values are taken from a data tape produced by the program discussed in Appendix D. For values above $\xi = 6$ we use again asymptotic solutions, as mentioned above.

Since many expressions in equation (79) for the far field and in equation (82) for the field at the plate edge are the same, we use the same subroutine, i.e., instructions 201+209 of the program. The trapezoidal integration segment is the subroutine between instructions 101 and 105. The field calculation between $\xi = 0$ and $\xi = 0.1$ is done between instructions 60 and 65, and the far field calculation is done between instructions 50 and 52. The rest of the program consists more or less of program management like loop controls etc. as well as the calculation of the Helmholtz wave field which has to be added to the values of u_{2D} to obtain u_2. In addition, the reading of the v_{2D} values from the data tape is checked with the ξ of each data set read from the tape against a ξ generated internally by the program. For a given x of the field points, the program calculates 15 values of -y with a step width of 0.05. This takes about 6 hours (!). So the data set for u_2 consisting of 16 x-subsets took about 96 hours. This is outrageous, but the computing time is free for a microcomputer and much time is saved during the program establishment phase, since the microcomputer can be used continuously. The BASIC computer program for u_2 is given on the next page and it is followed by a set of u_2 field data (see Table 3). Plots of these data are given in Fig. 10.

ORIGINAL PAGE IS OF POOR QUALITY

Program listing "u_2-PRON"

```
1:"U2-PRON"
2:INPUT "X=?";X
3:A=-6.1:N=27:M=46:V=1.E-8:E=0:F=0:Z=(√Π)/(4*√(√2))
4:A=A+.1
5:IF A>=0GOTO 10
6:W=Z*EXP A:G=W*COS (A-(Π/8)):H=W*SIN (A-(Π/8))
7:GOTO 14
10:INPUT #"V2D";A(65)
11:G=A(66):H=A(67)
12:IF A<>A(65) PRINT "LESEFEHLER"
13:IF A=.1GOTO 60
14:K=(G-E)*10:L=E
15:GOSUB 101
16:A(N)=A(N)+U
17:K=(H-F)*10:L=F
18:GOSUB 101
19:A(M)=A(M)+U
20:IF A=6.0GOTO 50
21:Y=Y+.05:N=N+1:M=M+1
22:IF Y<0.8GOTO 13
23:E=G:F=H:Y=0
24:N=27:M=46
25:IF A<6GOTO 4
26:PRINT "X=";X
27:PRINT "Y=";-Y
28:W=2*EXP (X-Y)
29:R=-A(N)+W*SIN (X+Y-(Π/8))
30:I=-A(M)-W*COS (X+Y-(Π/8))
31:PRINT "U2R=";R
32:PRINT "U2I=";I
33:PRINT "ABS(U2)=";√(R*R+I*I)
34:IF R=0LET R=V
35:D=ATN (I/R)
36:IF R<0GOTO 39
37:IF I<0LET D=D+Π
38:IF I<0LET D=D-Π
39:PRINT "PHASE(U2)DEG=";(D/Π)*180
40:Y=Y+.05:N=N+1:M=M+1
41:IF Y<.8GOTO 26
42:END
50:GOSUB 201
51:A(M)=A(M)-(1/(4*Π*(√W)))*(-D+(SIN (D/2))*(T-Π))
52:GOTO 21
60:G=2*(EXP A)*COS (A-(Π/8)):H=(G-E)*10:L=E
61:GOSUB 101
62:A(N)=A(N)+U
63:GOSUB 201
64:A(N)=A(N)-((√W)/Π)*(D+T*SIN (D*2))+((2*√.1)/Π):G=G-√.1
65:GOTO 17
101:B=H-.1:Y=Y+V
102:P=(N-B)*(X-B)+YY
103:D=(X-A)*(X-A)+YY
104:U=(K/Π)*(Y*(ATN ((A-X)/Y))-ATN ((B-X)/Y))-((L/(K+V))*(X-B)*.5*LN (D*P)-.1):Y=Y-V
105:RETURN
201:D=ATN (Y/(X+V))
202:IF X<0LET D=D+Π
203:W=√(Y*Y+V)
204:C=2+(√(8W))*(COS (D/2))
205:S=2+(√(8W))*SIN (D/2)
206:T=ATN (S/(N-M))
207:IF (N-M)<0 LET T=T+Π
208:D=.5*COS (D/2)*LN ((N+M)*C+(N-M)*S+W+M-C+S)
209:RETURN
```

$\chi = -2.0$

$\bar{y}$	0	0.05	0.1	0.15	0.2	0.25	0.3	0.35	0.4	1.45	0.5	0.55	0.6	0.65	0.7	0.75
$\tilde{u}_{2R}$	0.0083	0.0083	0.0089	0.0088	0.0087	0.0085	0.0082	0.0081	0.0079	0.0076	0.0073	0.0070	0.0066	0.0063	0.0059	0.0055
$\tilde{u}_{2I}$	0.1821	0.1821	0.1819	0.1817	0.1815	0.1811	0.1807	0.1802	0.1736	0.1790	0.1782	0.1774	0.1765	0.1757	0.1748	0.1737
$\tilde{u}_2$	0.1823	0.1823	0.1822	0.1820	0.1817	0.1813	0.1809	0.1804	0.1738	0.1791	0.1784	0.1776	0.1768	0.1758	0.1749	0.1738
phase^o	92.8	92.8	92.8	92.8	92.7	92.7	92.6	92.6	92.5	92.4	92.3	92.3	92.2	92.0	91.9	91.8

$\chi = -1.0$

$\bar{y}$	0	0.05	0.1	0.15	0.2	0.25	0.3	0.35	0.4	0.45	0.5	0.55	0.6	0.65	0.7	0.75
$\tilde{u}_{2R}$	0.0339	0.0338	0.0334	0.0328	0.0319	0.0308	0.0295	0.0281	0.0264	0.0247	0.0228	0.0208	0.0188	0.0167	0.0147	0.0126
$\tilde{u}_{2I}$	0.2523	0.2522	0.2518	0.2511	0.2502	0.2490	0.2475	0.2458	0.2439	0.2417	0.2394	0.2368	0.2342	0.2313	0.2283	0.2252
$\tilde{u}_2$	0.2546	0.2544	0.2540	0.2532	0.2522	0.2509	0.2492	0.2474	0.2453	0.2430	0.2405	0.2378	0.2349	0.2319	0.2288	0.2256
phase^o	97.7	97.6	97.6	97.4	97.3	97.1	96.8	96.5	96.2	95.8	95.4	95.0	94.6	94.1	93.7	93.2

Table 3 u_2-field data.

$\tilde{x} = -0.75$

$-\tilde{y}$	o	0.05	0.1	0.15	0.2	0.25	0.3	0.35	0.4	0.45	0.5	0.55	0.6	0.65	0.7	0.75
$\tilde{u}_{2R}$	0.0513	0.0511	0.0503	0.0491	0.0474	0.0453	0.0429	0.0401	0.0371	0.0340	0.0307	0.0273	0.0239	0.0205	0.0172	0.0139
$\tilde{u}_{2I}$	0.2831	0.2829	0.2823	0.2812	0.2798	0.2780	0.2758	0.2732	0.2704	0.2672	0.2638	0.2602	0.2563	0.2523	0.2481	0.2437
$\lvert\tilde{u}_2\rvert$	0.2877	0.2874	0.2867	0.2855	0.2838	0.2816	0.2791	0.2762	0.2729	0.2694	0.2656	0.2616	0.2574	0.2531	0.2486	0.2441
phase^o	100.3	100.2	100.1	99.9	99.6	99.3	98.8	98.4	97.8	97.2	96.6	96.0	95.3	94.7	94.0	93.3

$\tilde{x} = -0.5$

$-\tilde{y}$	o	0.05	0.1	0.15	0.2	0.25	0.3	0.35	0.4	0.45	0.5	0.55	0.6	0.65	0.7	0.75
$\tilde{u}_{2R}$	0.0823	0.0817	0.0800	0.0772	0.0734	0.0688	0.0637	0.0581	0.0522	0.0462	0.0402	0.0342	0.0284	0.0228	0.0174	0.0123
$\tilde{u}_{2I}$	0.3247	0.3244	0.3234	0.3216	0.3193	0.3163	0.3128	0.3088	0.3043	0.2994	0.2942	0.2887	0.2830	0.2771	0.2710	0.2648
$\lvert\tilde{u}_2\rvert$	0.3350	0.3345	0.3331	0.3308	0.3276	0.3237	0.3192	0.3142	0.3088	0.3030	0.297o	0.2908	0.2844	0.2780	0.2716	0.2651
phase^o	104.2	104.1	103.9	103.5	102.9	102.3	101.5	100.7	99.7	98.8	97,8	96.8	95.7	94.7	93.7	92.7

Table 3 u_2-field data (contd.).

$\tilde{x} = -0.25$

$-\tilde{y}$	o	0.05	0.1	0.15	0.2	0.25	0.3	0.35	0.4	0.45	0.5	0.55	0.6	0.65	0.7	0.75
$\tilde{u}_{2R}$	-0.1472	-0.1451	-0.1391	-0.1302	-0.1192	-0.1070	-0.0945	-0.0819	-0.0697	-0.0580	-0.0469	-0.0365	-0.0269	-0.0181	-0.0099	-0.002[illegible]
$\tilde{u}_{2I}$	-0.3849	-0.3842	-0.3821	-0.3788	-0.3743	-0.3688	-0.3625	-0.3556	-0.3480	-0.3401	-0.3317	-0.3231	-0.3144	-0.3055	-0.2965	-0.2876
$\lvert\tilde{u}_2\rvert$	0.4121	0.4107	0.4067	0.4005	0.3928	0.3841	0.3747	0.3649	0.3549	0.3450	0.3350	0.3252	0.3155	0.3060	0.2967	0.2876
phase^o	-110.9	-110.7	-110.0	-109.0	-107.7	-106.2	-104.6	-103.0	-101.3	-99.7	-98.0	-96.5	-94.9	-93.4	-91.9	-90.5

$\tilde{x} = -0.125$

$-\tilde{y}$	o	0.05	0.1	0.15	0.2	0.25	0.3	0.35	0.4	0.45	0.5	0.55	0.6	0.65	0.7	0.75
$\tilde{u}_{2R}$	-0.2159	-0.2095	-0.1935	-0.1731	-0.1515	-0.1304	-0.1104	-0.0918	-0.0749	-0.0590	-0.0447	-0.0317	-0.0200	-0.0095	-0.0001	-0.0083
$\tilde{u}_{2I}$	-0.4276	-0.4261	-0.4226	-0.4172	-0.4103	-0.4024	-0.3935	-0.3840	-0.3740	-0.3636	-0.3530	-0.3422	-0.3313	-0.3204	-0.3095	-0.2988
$\lvert\tilde{u}_2\rvert$	0.4790	0.4748	0.4648	0.4517	0.4374	0.4229	0.4087	0.3948	0.3814	0.3684	0.3558	0.3436	0.3319	0.3205	0.3095	0.2989
phase^o	-116.8	-116.2	-114.6	-112.5	-110.3	-108.0	-105.7	-103.4	-101.3	-99.2	-97.2	-95.3	-93.5	-91.7	-90.0	-88.4

Table 3 u_2-field data (contd.).

$\tilde{x}$ = 0.0

$\tilde{y}$	0	0.05	0.1	0.15	0.2	0.25	0.3	0.35	0.4	0.45	0.5	0.55	0.6	0.65	0.7	0.75
$\tilde{u}_{2R}$	−0.4858	−0.3282	−0.2645	−0.2169	−0.1781	−0.1453	−0.1170	−0.0922	−0.0704	−0.0512	−0.0341	−0.0191	−0.0058	+0.0059	+0.0161	+0.0251
$\tilde{u}_{2I}$	−0.4892	−0.4825	−0.4743	−0.4643	−0.4531	−0.4411	−0.4285	−0.4155	−0.4022	−0.3887	−0.3752	−0.3616	−0.3482	−0.3349	−0.3219	−0.3091
$\lvert\tilde{u}_2\rvert$	0.6894	0.5838	0.5431	0.5125	0.4869	0.4644	0.4442	0.4256	0.4083	0.3920	0.3767	0.3621	0.3483	0.3350	0.3223	0.3101
phase^o	−134.8	−124.2	−119.1	−115.0	−111.5	−108.2	−105.3	−102.5	−99.9	−97.5	−95.2	−93.0	−91.0	−89.0	−87.1	−85.4

$\tilde{x}$ = 0.125

$\tilde{y}$	0	0.05	0.1	0.15	0.2	0.25	0.3	0.35	0.4	0.45	0.5	0.55	0.6	0.65	0.7	0.75
$\tilde{u}_{2R}$	−0.3937	−0.3275	−0.2668	−0.2151	−0.1713	−0.1341	−0.1022	−0.0746	−0.0506	−0.0297	−0.0114	+0.0044	+0.0182	+0.0302	+0.0405	+0.0493
$\tilde{u}_{2I}$	−0.5698	−0.5522	−0.5352	−0.5181	−0.5008	−0.4834	−0.4660	−0.4486	−0.4313	−0.4141	−0.3972	−0.3805	−0.3642	−0.3482	−0.3326	−0.3175
$\lvert\tilde{u}_2\rvert$	0.6925	0.6420	0.5980	0.5609	0.5293	0.5017	0.4771	0.4548	0.4342	0.4152	0.3973	0.3805	0.3646	0.3495	0.3351	0.3213
phase^o	−124.6	−120.7	−116.5	−112.5	−108.9	−105.5	−102.4	−99.4	−96.7	−94.1	−91.7	−89.3	−87.1	−85.0	−83.1	−81.2

Table 3 u_2-field data (contd.).

$\tilde{x} = 0.25$

$-\tilde{y}$	o	0.05	0.1	0.15	0.2	0.25	0.3	0.35	0.4	0.45	0.5	0.55	0.6	0.65	0.7	0.75
$\tilde{u}_{2R}$	−0.3013	−0.2521	−0.2058	−0.1634	−0.1252	−0.0912	−0.0612	−0.0349	−0.0119	+0.0082	+0.0257	+0.0408	+0.0537	+0.0648	+0.0741	+0.0818
$\tilde{u}_{2I}$	−0.6471	−0.6217	−0.5971	−0.5730	−0.5493	−0.5262	−0.5034	−0.4812	−0.4594	−0.4381	−0.4174	−0.3973	−0.3778	−0.3589	−0.3406	−0.3230
$\lvert\tilde{u}_2\rvert$	0.7138	0.6709	0.6315	0.5958	0.5634	0.5340	0.5072	0.4824	0.4596	0.4382	0.4182	0.3994	0.3816	0.3647	0.3486	0.3332
phase^o	−115.0	−112.1	−109.0	−105.9	−102.8	−99.8	−96.9	−94.1	−91.5	−88.9	−86.5	−84.1	−81.9	−79.8	−77.7	−75.8

$\tilde{x} = 0.5$

$-\tilde{y}$	o	0.05	0.1	0.15	0.2	0.25	0.3	0.35	0.4	0.45	0.5	0.55	0.6	0.65	0.7	0.75
$\tilde{u}_{2R}$	−0.0770	−0.0439	−0.0132	+0.0150	+0.0407	+0.0639	+0.0845	+0.1026	+0.1184	+0.1318	+0.1432	+0.1525	+0.1600	+0.1658	+0.1700	+0.1728
$\tilde{u}_{2I}$	−0.7865	−0.7471	−0.7089	−0.6717	−0.6357	−0.6009	−0.5673	−0.5349	−0.5038	−0.4738	−0.4451	−0.4176	−0.3913	−0.3662	−0.3424	−0.3197
$\lvert\tilde{u}_2\rvert$	0.7903	0.7484	0.7090	0.6719	0.6371	0.6043	0.5736	0.5447	0.5175	0.4918	0.4675	0.4445	0.4227	0.4020	0.3823	0.3634
phase^o	−95.6	−93.4	−91.1	−88.7	−86.3	−83.9	−81.5	−79.1	−76.8	−74.4	−72.2	−69.9	−67.8	−65.6	−63.6	−61.6

Table 3 u_2-field data (contd.).

$\tilde{x}$ = 0.75

$-\tilde{y}$	o	0.05	0.1	0.15	0.2	0.25	0.3	0.35	0.4	0.45	0.5	0.55	0.6	0.65	0.7	0.75
$\tilde{u}_{2R}$	+ 0.2021	0.2240	0.2431	0.2596	0.2736	0.2851	0.2943	0.3013	0.3063	0.3093	0.3106	0.3103	0.3085	0.3053	0.3009	0.2954
$\tilde{u}_{2I}$	− 0.8989	0.8445	0.7919	0.7412	0.6924	0.6456	0.6009	0.5581	0.5174	0.4786	0.4419	0.4071	0.3742	0.3432	0.3141	0.2867
$\lvert\tilde{u}_2\rvert$	0.9214	0.8737	0.8284	0.7853	0.7445	0.7058	0.6691	0.6343	0.6012	0.5699	0.5401	0.5119	0.4850	0.4593	0.4349	0.4117
phase^o	− 77.3	75.1	72.9	70.7	68.4	66.2	63.9	61.6	59.4	57.1	54.9	52.7	50.5	48.3	46.2	44.1

$\tilde{x}$ = 1.0

$-\tilde{y}$	o	0.05	0.1	0.15	0.2	0.25	0.3	0.35	0.4	0.45	0.5	0.55	0.6	0.65	0.7	0.75
$\tilde{u}_{2R}$	+ 0.5531	0.5613	0.5662	0.5682	0.5674	0.5643	0.5588	0.5514	0.5421	0.5312	0.5189	0.5053	0.4906	0.4750	0.4587	0.4417
$\tilde{u}_{2I}$	− 0.9665	0.8950	0.8264	0.7610	0.6987	0.6396	0.5835	0.5305	0.4805	0.4335	0.3894	0.3482	0.3097	0.2738	0.2406	0.2098
$\lvert\tilde{u}_2\rvert$	1.1136	1.0564	1.0018	0.9497	0.9001	0.8529	0.8079	0.7651	0.7244	0.6857	0.6488	0.6136	0.5802	0.5483	0.5179	0.4890
phase^o	− 60.2	57.9	55.6	53.3	50.9	48.6	46.2	43.9	41.6	39.2	36.9	34.6	32.3	30.0	27.7	25.4

Table 3 u_2-field data (contd.).

$\tilde{x} = 1.5$

$-\tilde{y}$	o	0.05	0.1	0.15	0.2	0.25	0.3	0.35	0.4	0.45	0.5	0.55	0.6	0.65	0.7	0.75
$\tilde{u}_{2R}$	+ 1.5197	1.4766	1.4307	1.3824	1.3323	1.2806	1.2279	1.1744	1.1206	1.0665	1.0126	0.9591	0.9061	0.8539	0.8027	0.7525
$\tilde{u}_{2I}$	− 0.5254	0.7178	0.6173	0.5238	0.4370	0.3567	0.2828	0.2148	1.5273	0.0962	0.0449	+ 0.0014	+ 0.0429	+ 0.0798	+ 0.1125	+ 0.1412
$\lvert\tilde{u}_2\rvert$	1.7294	1.6418	1.5581	1.4783	1.4021	1.3294	1.2601	1.1939	1.1309	1.0708	1.0136	0.9591	0.9071	0.8576	0.8105	0.7656
phase^o	− 28.5	25.9	23.3	20.8	18.2	15.6	13.0	10.4	7.8	5.2	2.5	+ 0.1	+ 2.7	+ 5.3	+ 8.0	+ 10.6

$\tilde{x} = 2.0$

$-\tilde{y}$	o	0.05	0.1	0.15	0.2	0.25	0.3	0.35	0.4	0.45	0.5	0.55	0.6	0.65	0.7	0.75
$\tilde{u}_{2R}$	+ 2.7881	2.6429	2.4990	2.3570	2.2173	2.0804	1.9467	1.8165	1.6900	1.5677	1.4495	1.3357	1.2265	1.1218	1.0218	0.9264
$\tilde{u}_{2I}$	+ 0.0662	0.1896	0.3002	0.3986	0.4855	0.5615	0.6274	0.6838	0.7314	0.7706	0.8022	0.8267	0.8446	0.8566	0.8630	0.8645
$\lvert\tilde{u}_2\rvert$	2.7889	2.6497	2.5170	2.3904	2.2698	2.1548	2.0453	1.9409	1.8415	1.7468	1.6567	1.5708	1.4892	1.4114	1.3375	1.2671
phase^o	+ 1.4	4.1	6.9	9.6	12.3	15.1	17.9	20.6	23.4	26.2	29.0	31.7	34.6	37.4	40.2	43.0

Table 3 u_2-field data (contd.).

$\tilde{x} = 2.5$

$-\tilde{y}$	o	0.05	0.1	0.15	0.2	0.25	0.3	0.35	0.4	0.45	0.5	0.55	0.6	0.65	0.7	0.75
$\tilde{u}_{2R}$	+3.9310	3.6242	3.3294	3.0469	2.7767	2.5191	2.2740	2.0415	1.8214	1.6136	1.4180	1.2342	1.0621	0.9013	0.7516	0.6125
$\tilde{u}_{2I}$	+2.3128	2.3796	2.4286	2.4612	2.4789	2.4829	2.4745	2.4549	2.4254	2.3869	2.3405	2.2872	2.2279	2.1634	2.0945	2.0220
$\lvert\tilde{u}_2\rvert$	4.5609	4.3356	4.1211	3.9168	3.7222	3.5370	3.3607	3.1929	3.0331	2.8811	2.7365	2.5989	2.4681	2.3436	2.2253	2.1127
phase^o	+30.5	33.3	36.1	38.9	41.8	44.6	47.4	50.3	53.1	55.9	58.8	61.4	64.5	67.4	70.3	73.1

$\tilde{x} = 3.0$

$-\tilde{y}$	o	0.05	0.1	0.15	0.2	0.25	0.3	0.35	0.4	0.45	0.5	0.55	0.6	0.65	0.7	0.75
$\tilde{u}_{2R}$	+3.8290	3.3318	2.8662	2.4312	2.0261	1.6499	1.3016	0.9804	0.6850	0.4145	+0.1678	−0.0562	−0.2586	−0.4405	−0.6030	−0.7471
$\tilde{u}_{2I}$	+6.4458	6.3028	6.1433	5.9697	5.7840	5.5884	5.3874	5.1745	4.9597	4.7415	4.5214	4.3005	4.0800	3.8610	3.6442	3.4306
$\lvert\tilde{u}_2\rvert$	7.4973	7.1293	6.7790	6.4458	6.1286	5.8269	5.5397	5.2666	5.0067	4.7596	4.5245	4.3009	4.0882	3.8860	3.6938	3.5110
phase^o	59.3	62.1	65.0	67.8	70.7	73.6	76.4	79.3	82.1	85.0	87.9	90.7	93.6	96.5	99.4	102.3

Table.3 u_2-field data (contd.).

$\tilde{x}$ = 4.0

$-\tilde{y}$	o	0.05	0.1	0.15	0.2	0.25	0.3	0.35	0.4	0.45	0.5	0.55	0.6	0.65	0.7	0.75
$\tilde{u}_{2R}$	− 9.1335	− 9.5411	− 9.8644	− 10.110	− 10.284	− 10.393	− 10.442	− 10.436	− 10.382	− 10.283	− 10.145	− 9.972	− 9.767	− 9.536	− 9.281	− 9.007
$\tilde{u}_{2I}$	+ 18.184	16.840	15.544	14.298	13.101	11.957	10.864	9.823	8.835	7.899	7.014	6.180	5.395	4.659	3.972	3.331
$\lvert\tilde{u}_2\rvert$	20.349	19.355	18.410	17.511	16.656	15.842	15.068	14.333	13.632	12.967	12.333	11.731	11.158	10.613	10.096	9.603
phase^o	+ 116.7	119.5	122.4	125.3	128.1	131.0	133.9	136.7	139.6	142.5	145.3	148.2	151.1	154.0	156.8	159.7

$\tilde{x}$ = 5.0

$-\tilde{y}$	o	0.05	0.1	0.15	0.2	0.25	0.3	0.35	0.4	0.45	0.5	0.55	0.6	0.65	0.7	0.75
$\tilde{u}_{2R}$	− 54.997	− 52.525	− 50.039	− 47.551	− 45.073	− 42.618	− 40.193	− 37.807	− 35.469	− 33.185	− 30.960	− 28.800	− 26.708	− 24.688	− 22.743	− 20.875
$\tilde{u}_{2I}$	+ 5.803	+ 2.898	+ 0.256	− 2.137	− 4.291	− 6.220	− 7.936	− 9.451	− 10.777	− 11.926	− 12.908	− 13.736	− 14.420	− 14.970	− 15.397	− 15.710
$\lvert\tilde{u}_2\rvert$	55.303	52.605	50.039	47.599	45.277	43.069	40.969	38.971	37.070	35.263	33.543	31.908	30.352	28.872	27.465	26.126
phase^o	+ 174.0	+ 176.8	+ 179.7	− 177.4	− 174.6	− 171.7	− 168.8	− 166.0	− 163.1	− 160.2	− 157.4	− 154.5	− 151.6	− 148.8	− 145.9	− 143.0

Table 3 u_2-field data (contd.).

$\tilde{x} = 10.0$

$-\tilde{y}$	o	0.05	0.1	0.15	0.2	0.25	0.3	0.35	0.4	0.45	0.5	0.55	0.6	0.65	0.7	0.75
$\tilde{u}_{2R}$	− 1489.7	− 1799.0	− 2070.3	− 2305.9	− 2508.2	− 2679.2	− 2821.3	− 2936.4	− 3026.6	− 3093.8	− 3139.9	− 3166.7	− 3175.8	− 3169.0	− 3147.8	− 3113.6
$\tilde{u}_{2I}$	+ 8071.0	7597.0	7131.9	6677.2	6233.9	5803.3	5386.0	4982.7	4594.2	4220.8	3862.8	3520.6	3194.2	2883.6	2588.9	2309.9
$\lvert\tilde{u}_2\rvert$	8207.3	7807.1	7426.3	7064.1	6719.6	6391.9	6080.1	5783.6	5501.5	5233.2	4978.0	4735.2	4504.3	4284.6	4075.6	3876.9
phase^o	+ 100.5	103.3	106.2	109.0	111.9	114.8	117.6	120.5	123.4	126.2	129.1	132.0	134.8	137.7	140.6	143.4

Table 3 u_2-field data (contd.).